



POLITECNICO DI TORINO

Master's Degree in Aerospace Engineering

**Modeling, Dynamics and Control
of Space Tethered System as
Distributed Radar Array**



Jet Propulsion Laboratory
California Institute of Technology

Mentor

Dr. Marco B. QUADRELLI

Jet Propulsion Laboratory

Candidate

Stefano ALIBERTI

Supervisor

Prof. Lorenzo CASALINO

Politecnico di Torino

October 2022

This research was carried out at Jet Propulsion Laboratory, California Institute of Technology, during an internship sponsored by JVS RP (JPL Visiting Student Research Program) and NASA (National Aeronautic and Space Administration).

Acknowledgements

Un ringraziamento speciale va al mio Tutor Dott. Marco B. Quadrelli, che mi ha aiutato a condurre le ricerche, oggetto dell'elaborato, presso il NASA Jet Propulsion Laboratory, e al mio Relatore Prof. Lorenzo Casalino, che mi ha guidato nel perfezionamento della mia tesi.

Ringrazio particolarmente la mia famiglia, che mi ha supportato costantemente durante questi anni, motivandomi e appoggiandomi in ogni mia scelta e rassicurandomi nei momenti difficili.

Infine, ringrazio gli amici, i colleghi e tutte le persone che hanno avuto un ruolo importante durante questo mio percorso, con le quali ho affrontato le difficoltà e condiviso le gioie di questa esperienza.

Abstract

Distributed Space Systems are an anticipated critical technology, thanks to which it would be possible to achieve performance unattainable with classical monolithic satellites. These systems are composed of several small satellites working together to achieve a common goal. Due to the distributed nature of this type of system, it is possible to achieve great reliability and adaptability to different types of missions, providing great robustness and flexibility while maintaining low costs.

The purpose of this thesis is to study the dynamics and control of a Tethered Space System: a system composed of several CubeSats connected to each other via a tether. Several other analyses have already been carried out at the Jet Propulsion Laboratory over the past few years, in order to assess the possible applications of this type of architecture in Low Earth Orbit. Among them, the use of a radially positioned tethered system for radar remote sensing is of particular interest: due to the presence of the gravitational gradient, this configuration is particularly stable and performing, preserving the relative position between its elements with a less frequent and expensive control.

Therefore, the aim of this work is to continue the research on this type of system, evaluating the reliability of a radial tethered system and considering the feasibility of other possible configurations. To do this, an optimization and improvement of the tool used for the simulation of this type of system was initially carried out, analyzing the significant influence of the integration method on the calculation time required for simulation.

As a result of the optimization work carried out, it was possible to perform an Uncertainty Propagation analysis based on Monte Carlo methods, which further revealed the better performance of a Tethered Space System compared to Formation Flight.

Finally, the feasibility of an across-track configuration was analyzed, introducing an optimal control and a state estimator to keep the system in place. This analysis revealed that the stabilization of this configuration is relatively simple, requiring only a constant force in modulus and direction. Therefore, the possibility of introducing a control through aerodynamic surfaces to limit the use of the actuators was evaluated.

Table of Contents

List of Tables	v
List of Figures	vi
1 Introduction	1
1.1 Overview of Distributed Space Systems	1
1.2 Benefits of Distributed Space Systems for Remote Sensing	4
1.3 Advantages of Tethered Space Systems	6
1.4 Work Subdivision	7
2 Mathematical Notation and Reference Frames	9
2.1 Vectors and Vectrices	9
2.2 Rotation Matrices	10
2.3 Rotating Reference Frame	11
2.4 Quaternions	12
2.5 Refence Frames	13
2.5.1 Earth Centered Inertial (ECI)	14
2.5.2 Local Vertical - Local Horizontal (LVLH)	15
2.5.3 Tether Frame (TF)	16
2.5.4 Body Frame (BF)	17
3 Kinematics and Kinetics	18
3.1 Modeling of External Forces	18
3.1.1 Earth's Gravitational Potential Perturbation	19
3.1.2 Atmospheric Drag Perturbation	20
3.1.3 Solar Pressure Perturbation	21
3.1.4 Third-body Perturbation	22
3.2 Modeling of Internal Forces	23
3.2.1 Discretized Mass Tether Model	23
3.2.2 Tension Forces	24
3.2.3 Control Forces	26

3.3	Equations of motion	27
3.3.1	Translational Dynamics	27
3.3.2	Attitude Dynamics	29
4	Numerical Simulation and Optimization	32
4.1	Architecture of the code	32
4.1.1	Initialization	34
4.1.2	Simulation	36
4.1.3	Post Processing	37
4.2	Numerical optimization	40
4.2.1	Simulation parameters	40
4.2.2	Analysis of Results and Computational time	42
4.2.3	Frequency Analysis of TSS Dynamics	44
4.2.4	Choice of Integration Method	46
4.2.5	Results of the optimization	47
5	Monte-Carlo Analysis on Uncertainty Propagation	49
5.1	Methodology applied in the study	49
5.2	Position Uncertainties	51
5.2.1	Uncertainty on the In-plane Angle (α)	51
5.2.2	Uncertainty on the Out-of-Plane Angle (β)	53
5.2.3	Analysis of Results for Position Uncertainties	55
5.3	Satellites' Characteristics Uncertainties	56
5.3.1	Uncertainty on Masses (m_i)	56
5.3.2	Uncertainty on Surfaces (A_i)	59
5.3.3	Uncertainty on Drag Coefficients (CD_i)	61
5.3.4	Uncertainty on Reflectivity Coefficients (CR_i)	64
5.3.5	Analysis of Results for Satellites' Characteristics Uncertainties	66
6	Feasibility Study of an Across-Track Configuration	68
6.1	Free propagation of an EndFire Array oriented across-track	69
6.2	Stabilization using Optimal Control	72
6.2.1	Model linearization	73
6.2.2	State Estimation	75
6.2.3	Definition of an LQR controller	77
6.2.4	Results of controlled simulation	78
7	Aerodynamic Stabilization of the Across-Track Configuration	84
7.1	Decomposition of Control Forces	84
7.2	Validation of the Decomposition	86
7.3	Aerodynamic Stabilization	88
7.3.1	Modeling Aerodynamic Surfaces	89

7.3.2	Effectiveness Analysis of the Aerodynamic Control System	92
8	Conclusions and Future Work	96
8.1	Conclusions	96
8.2	Future work	98
	Bibliography	100
A	Additional Plots Uncertainty Propagation	103
A.1	Uncertainty on the In-plane Angle (α)	103
A.2	Uncertainty on the Out-of-plane Angle (β)	106
A.3	Uncertainty on Masses (m_i)	109
A.4	Uncertainty on Surfaces (A_i)	112
A.5	Uncertainty on Drag Coefficients (CD_i)	115
A.6	Uncertainty on Reflectivity Coefficients (CD_i)	118
B	Additional Plots Aerodynamic Stabilization	122
B.1	Average Altitude 200 <i>km</i>	122
B.2	Average Altitude 250 <i>km</i>	124
B.3	Average Altitude 300 <i>km</i>	125

List of Tables

4.1	<i>Satellite characteristics</i>	40
4.2	<i>Tether lumps characteristics</i>	41
4.3	<i>Tether characteristics</i>	41
4.4	<i>Orbit characteristics</i>	41
4.5	<i>Natural frequencies of the modes of the system under examination.</i>	45
4.6	<i>Comparison of the performance of different <code>matlab</code> built-in integration methods for systems of stiff equations.</i>	46
6.1	<i>Satellite characteristics for simplified simulation</i>	70
6.2	<i>Propellant consumption for the maintenance of the across-track configuration for 1, 10 and 50 orbits</i>	81
7.1	<i>Aerodynamic contribution on the control force for the different orbits simulated.</i>	94

List of Figures

1.1	<i>Representation of the GPS satellite constellation. Credits: NASA</i>	2
1.2	<i>Artistic representation of the LISA mission. Credits: NASA</i>	2
1.3	<i>Artistic representation of the TSS-1 mission. Credits: NASA</i>	3
1.4	<i>Representation of the Footprint of an antenna. Credits: ESA</i>	4
1.5	<i>Schematic representation of an EndFire Array arranged radially</i>	6
2.1	<i>Graphical representation of the ECI reference frame</i>	14
2.2	<i>Graphical representation of the LVLH reference frame</i>	15
2.3	<i>Graphical representation of the Tether Reference Frame compared with the LVLH frame and ECI frame</i>	16
2.4	<i>Graphical representation of the Body Reference Frame compared with the LVLH frame and ECI frame</i>	17
3.1	<i>Model of the conical shadow</i>	21
3.2	<i>Schematization of the undeformed tether and material coordinate s</i>	23
3.3	<i>Schematization representing the discretization used for the tether mass</i>	24
3.4	<i>Difference between stress modeling of a spring and a string</i>	25
3.5	<i>Representation of the most significant sources of torque in LEO orbit as a function of altitude referenced to the center of the earth. Credit: Spacecraft Attitude Dynamics, Hughes P.C., pag 271 [8]</i>	30
4.1	<i>Schematization of code structure.</i>	33
4.2	<i>Schematization of the error ($\Delta\alpha$) between the real horizontal and vertical axes and those of the ORF that incurs when the system moves too far away from it.</i>	38
4.3	<i>Non-scale representation of the 11-mass EndFire array.</i>	40
4.4	<i>Evolution of the radial position of the 11 masses representing the EndFire Array. The graph is referred to the center of mass of the system.</i>	42

4.5	<i>Evolution of the along-track position of the 11 masses representing the EndFire Array. The graph is referred to the center of mass of the system.</i>	42
4.6	<i>Evolution of the across-track position of the 11 masses representing the EndFire Array. The graph is referred to the center of mass of the system.</i>	43
4.7	<i>Comparison of the integration time required by different integration methods against the number of orbits simulated.</i>	47
5.1	<i>Distribution of in-plane angle for the initial condition of the different samples employed.</i>	51
5.2	<i>Representation of the final condition (after 10 orbits) of the 500 samples differing in the initial condition of the in-plane angle (X-Y plane)</i>	52
5.3	<i>Representation of the final condition (after 10 orbits) of the 500 samples differing in the initial condition of the in-plane angle (X-Z plane)</i>	52
5.4	<i>Evolution of the standard deviation of the α and β angles due to an uncertainty in the in-plane angle.</i>	53
5.5	<i>Distribution of out-of-plane angle for the initial condition of the different samples employed.</i>	53
5.6	<i>Representation of the final condition (after 10 orbits) of the 500 samples differing in the initial condition of the out-of-plane angle (X-Y plane)</i>	54
5.7	<i>Representation of the final condition (after 10 orbits) of the 500 samples differing in the initial condition of the out-of-plane angle (X-Z plane)</i>	54
5.8	<i>Evolution of the standard deviation of the α and β angles due to an uncertainty in the out-of-plane angle.</i>	55
5.9	<i>Distribution of the masses used for the different samples of satellite 1.</i>	56
5.10	<i>Representation of the final condition (after 10 orbits) of the 500 samples differing in the mass of each body (X-Y plane)</i>	57
5.11	<i>Representation of the final condition (after 10 orbits) of the 500 samples differing in the mass of each body (X-Z plane)</i>	57
5.12	<i>Evolution of position standard deviation due to 10% uncertainty in mass for satellites 1, 6 and 11.</i>	58
5.13	<i>Evolution of velocity standard deviation due to 10% uncertainty in mass for satellites 1, 6 and 11.</i>	58
5.14	<i>Distribution of the surfaces used for the different samples of satellite 1.</i>	59
5.15	<i>Representation of the final condition (after 10 orbits) of the 500 samples differing in the surfaces of each body (X-Y plane)</i>	59

5.16	<i>Representation of the final (after 10 orbits) condition of the 500 samples differing in the surfaces of each body (X-Z plane)</i>	60
5.17	<i>Evolution of position standard deviation due to 10% uncertainty in surfaces for satellites 1, 6 and 11.</i>	60
5.18	<i>Evolution of velocity standard deviation due to 10% uncertainty in surfaces for satellites 1, 6 and 11.</i>	61
5.19	<i>Distribution of the drag coefficients used for the different samples of satellite 1.</i>	61
5.20	<i>Representation of the final condition (after 10 orbits) of the 500 samples differing in the drag coefficients of each body (X-Y plane)</i>	62
5.21	<i>Representation of the final (after 10 orbits) condition of the 500 samples differing in the drag coefficients of each body (X-Z plane)</i>	62
5.22	<i>Evolution of position standard deviation due to 10% uncertainty in drag coefficients for satellites 1, 6 and 11.</i>	63
5.23	<i>Evolution of velocity standard deviation due to 10% uncertainty in drag coefficients for satellites 1, 6 and 11.</i>	63
5.24	<i>Distribution of the reflectivity coefficients used for the different samples of satellite 1.</i>	64
5.25	<i>Representation of the final condition (after 10 orbits) of the 500 samples differing in the reflectivity coefficients of each body (X-Y plane)</i>	64
5.26	<i>Representation of the final (after 10 orbits) condition of the 500 samples differing in the reflectivity coefficients of each body (X-Z plane)</i>	65
5.27	<i>Evolution of position standard deviation due to 10% uncertainty in reflectivity coefficients for satellites 1, 6 and 11.</i>	65
5.28	<i>Evolution of velocity standard deviation due to 10% uncertainty in reflectivity coefficients for satellites 1, 6 and 11.</i>	66
6.1	<i>Comparison between the radial configuration (on the right) and across-track configuration (on the left).</i>	68
6.2	<i>Schematization of the simplified system in the across-track configuration.</i>	69
6.3	<i>Evolution of the radial position of the 2 masses representing the EndFire Array, initialized in the across-track configuration. The graph is referred to the center of mass of the system.</i>	70
6.4	<i>Evolution of the along-track position of the 2 masses representing the EndFire Array, initialized in the across-track configuration. The graph is referred to the center of mass of the system.</i>	71

6.5	<i>Evolution of the across-track position of the 2 masses representing the EndFire Array, initialized in the across-track configuration. The graph is referred to the center of mass of the system.</i>	71
6.6	<i>Schematization of a De-Centralized Measurement Architecture for a system of N bodies</i>	76
6.7	<i>Evolution of the radial position of the 2 masses representing the EndFire Array, controlled in order to maintain the across-track configuration.</i>	79
6.8	<i>Evolution of the along-track position of the 2 masses representing the EndFire Array, controlled in order to maintain the across-track configuration.</i>	80
6.9	<i>Evolution of the across-track position of the 2 masses representing the EndFire Array, controlled in order to maintain the across-track configuration.</i>	80
6.10	<i>Control forces in the radial direction acting on the two satellites generated by the command law in order to maintain the system in the across-track configuration.</i>	82
6.11	<i>Control forces in the along-track direction acting on the two satellites generated by the command law in order to maintain the system in the across-track configuration.</i>	82
6.12	<i>Control forces in the across-track direction acting on the two satellites generated by the command law in order to maintain the system in the across-track configuration.</i>	83
7.1	<i>Evolution of average command forces during 50 orbits.</i>	85
7.2	<i>Evolution of differential command forces during 50 orbits.</i>	86
7.3	<i>Evolution of the radial position of the 2 masses representing the EndFire Array, controlled using only the across-track force.</i>	87
7.4	<i>Evolution of the along-track position of the 2 masses representing the EndFire Array, controlled using only the across-track force.</i>	87
7.5	<i>Evolution of the across-track position of the 2 masses representing the EndFire Array, controlled using only the across-track force.</i>	88
7.6	<i>Non-scale schematization of the system with aerodynamic surfaces.</i>	89
7.7	<i>Comparison between the approximate value of the lift coefficient and that obtained by the complete formula for the maximum and minimum values of the parameter s.</i>	91
7.8	<i>Comparison between the approximate value of the drag coefficient and that obtained by the complete formula for the maximum and minimum values of the parameter s.</i>	91
7.9	<i>Contribution of aerodynamic forces (F_a) and thruster (F_t) forces on total control force (F) for an orbit with an average altitude of 200 km).</i>	93

7.10	<i>Contribution of aerodynamic forces (F_a) and thruster (F_t) forces on total control force (F) for an orbit with an average altitude of 250 km.</i>	93
7.11	<i>Contribution of aerodynamic forces (F_a) and thruster (F_t) forces on total control force (F) for an orbit with an average altitude of 300 km.</i>	94
A.1	<i>Position distribution for satellite 1 after 10 orbits, uncertainty on In-plane angle</i>	103
A.2	<i>Position distribution for satellite 6 after 10 orbits, uncertainty on In-plane angle</i>	104
A.3	<i>Position distribution for satellite 11 after 10 orbits, uncertainty on In-plane angle</i>	104
A.4	<i>Velocity distribution for satellite 1 after 10 orbits, uncertainty on In-plane angle</i>	105
A.5	<i>Velocity distribution for satellite 6 after 10 orbits, uncertainty on In-plane angle</i>	105
A.6	<i>Velocity distribution for satellite 11 after 10 orbits, uncertainty on In-plane angle</i>	106
A.7	<i>Position distribution for satellite 1 after 10 orbits, uncertainty on Out-of-plane angle</i>	106
A.8	<i>Position distribution for satellite 6 after 10 orbits, uncertainty on Out-of-plane angle</i>	107
A.9	<i>Position distribution for satellite 11 after 10 orbits, uncertainty on Out-of-plane angle</i>	107
A.10	<i>Velocity distribution for satellite 1 after 10 orbits, uncertainty on Out-of-plane angle</i>	108
A.11	<i>Velocity distribution for satellite 6 after 10 orbits, uncertainty on Out-of-plane angle</i>	108
A.12	<i>Velocity distribution for satellite 11 after 10 orbits, uncertainty on Out-of-plane angle</i>	109
A.13	<i>Position distribution for satellite 1 after 10 orbits, uncertainty on masses</i>	109
A.14	<i>Position distribution for satellite 6 after 10 orbits, uncertainty on masses</i>	110
A.15	<i>Position distribution for satellite 11 after 10 orbits, uncertainty on masses</i>	110
A.16	<i>Velocity distribution for satellite 1 after 10 orbits, uncertainty on masses</i>	111
A.17	<i>Velocity distribution for satellite 6 after 10 orbits, uncertainty on masses</i>	111
A.18	<i>Velocity distribution for satellite 11 after 10 orbits, uncertainty on masses</i>	112

A.19	<i>Position distribution for satellite 1 after 10 orbits, uncertainty on surfaces</i>	112
A.20	<i>Position distribution for satellite 6 after 10 orbits, uncertainty on surfaces</i>	113
A.21	<i>Position distribution for satellite 11 after 10 orbits, uncertainty on surfaces</i>	113
A.22	<i>Velocity distribution for satellite 1 after 10 orbits, uncertainty on surfaces</i>	114
A.23	<i>Velocity distribution for satellite 6 after 10 orbits, uncertainty on surfaces</i>	114
A.24	<i>Velocity distribution for satellite 11 after 10 orbits, uncertainty on surfaces</i>	115
A.25	<i>Position distribution for satellite 1 after 10 orbits, uncertainty on drag coefficients</i>	115
A.26	<i>Position distribution for satellite 6 after 10 orbits, uncertainty on drag coefficients</i>	116
A.27	<i>Position distribution for satellite 11 after 10 orbits, uncertainty on drag coefficients</i>	116
A.28	<i>Velocity distribution for satellite 1 after 10 orbits, uncertainty on drag coefficients</i>	117
A.29	<i>Velocity distribution for satellite 6 after 10 orbits, uncertainty on drag coefficients</i>	117
A.30	<i>Velocity distribution for satellite 11 after 10 orbits, uncertainty on drag coefficients</i>	118
A.31	<i>Position distribution for satellite 1 after 10 orbits, uncertainty on reflectivity coefficients</i>	118
A.32	<i>Position distribution for satellite 6 after 10 orbits, uncertainty on reflectivity coefficients</i>	119
A.33	<i>Position distribution for satellite 11 after 10 orbits, uncertainty on reflectivity coefficients</i>	119
A.34	<i>Velocity distribution for satellite 1 after 10 orbits, uncertainty on reflectivity coefficients</i>	120
A.35	<i>Velocity distribution for satellite 6 after 10 orbits, uncertainty on reflectivity coefficients</i>	120
A.36	<i>Velocity distribution for satellite 11 after 10 orbits, uncertainty on reflectivity coefficients</i>	121
B.1	<i>Average control forces for an orbit with an average altitude orbit of 200 km</i>	122
B.2	<i>Differential control forces for an orbit with an average altitude orbit of 200 km</i>	123

B.3	<i>Variation of angle of attack for an orbit with an average altitude of 200 km</i>	123
B.4	<i>Average control forces for an orbit with an average altitude orbit of 250 km</i>	124
B.5	<i>Differential control forces for an orbit with an average altitude orbit of 250 km</i>	124
B.6	<i>Variation of angle of attack for an orbit with an average altitude of 250 km</i>	125
B.7	<i>Average control forces for an orbit with an average altitude orbit of 300 km</i>	125
B.8	<i>Differential control forces for an orbit with an average altitude orbit of 300 km</i>	126
B.9	<i>Variation of angle of attack for an orbit with an average altitude of 300 km</i>	126

Chapter 1

Introduction

This thesis will discuss the results of a research work on Tethered Space Systems, during which a code for the simulation of these systems was refined and subsequently used to perform analyses on the behavior of a EndFire Array in Low Earth Orbit. To introduce the reader to the study carried out, in this section, the concept of a *Distributed Space System* will be introduced, the advantages and possible applications for remote sensing will be examined, and then tethered systems will be analyzed specifically.

At the end of this chapter you will find a section in which the various topics that will be addressed in each chapter are presented.

1.1 Overview of Distributed Space Systems

A *Distributed Space System* is a system composed of several spacecraft, which work together to accomplish a given mission.

These kinds of systems are being particularly studied in recent years because they would allow for great advantages in terms of cost and performance. [1]

Generally the satellites that make up this type of architecture are small in size (SmallSat), consequently they are much less expensive than the large monolithic satellites that are classically used. In addition, the distributed nature of this type of system provides great flexibility and robustness, since this type of system can be easily scaled, adapted and reconfigured for different missions while retaining great reliability and a great fault-tolerance, given the independence of the different spacecraft.

It is possible to divide the various types of distributed systems into 3 main categories, depending on their functionality and specific architecture:

- **Constellations**

Satellite constellations are currently the most common type of distributed space system. This type of system consists of several satellites flying in similar orbits without control of relative position, that are organized in time and space to coordinate round coverage. Famous examples of this type of system may be the *GPS* (Global Positioning System) constellation consisting of 24 satellites in MEO (Medium Earth Orbit) or *Starlink* (currently under construction), which envisions more than 12,000 satellites in LEO (Low Earth Orbit).

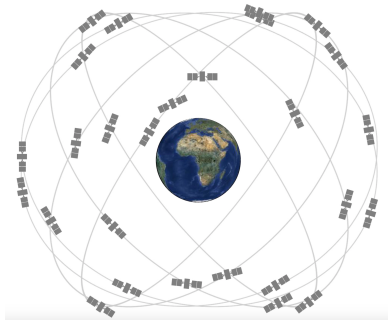


Figure 1.1: Representation of the GPS satellite constellation. Credits: NASA

- **Formation**

Formation flight is a type of distributed space system that consists of several satellites orbiting while maintaining a certain relative position, in order to be coordinate to perform the function of a single, large, virtual instrument. The applications of this type of system can be various: from earth observation and remote sensing of planets to gravitational field measurement. An example of this type of constellation may be the *LISA* (Laser Interferometer Space Antenna) mission carried out in collaboration between NASA and ESA planned for the early 2030s. This consists of three satellites placed as an equilateral triangle on the sides of a million miles, the purpose of which is the detection of gravitational waves.

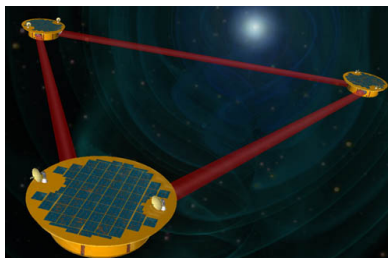


Figure 1.2: Artistic representation of the LISA mission. Credits: NASA

- **Swarm**

A wide-scale distributed system composed of a very large number of individual satellites cooperating to achieve a joint goal.

- **Tethered**

A tethered distributed system is a particular case of formation flight, in which the different satellites that make up the system are connected to each other through a cable. This type of architecture is particularly interesting, because it allows for greater control over the relative position of the satellites and ensures greater stability. Nevertheless, the dynamics of this type of system are particularly complex and require in-depth study. An example of an application of a tether system may be *TSS-1*, which was born between the collaboration between NASA and ASI (Italian Space Agency). The purpose of this mission was to test the gravitational gradient stabilization of a tethered system by relaunching a satellite connected to a shuttle with a 20-km cable.



Figure 1.3: *Artistic representation of the TSS-1 mission. Credits: NASA*

1.2 Benefits of Distributed Space Systems for Remote Sensing

The use of radar for remote sensing for scientific investigation is now widespread, both for the study of the Earth's surface and subsurface and for the study of other planets. In order to have good results, however, it is necessary to use instrumentation that guarantees good performance and accuracy in data acquisition. The main parameters that determine the accuracy of a given radar instrumentation for remote sensing are:

- **Resolution:** which determines size of a pixel recorded in an image;
- **Footprint size:** which represents the size of the area observed by the sensor during a single observation.

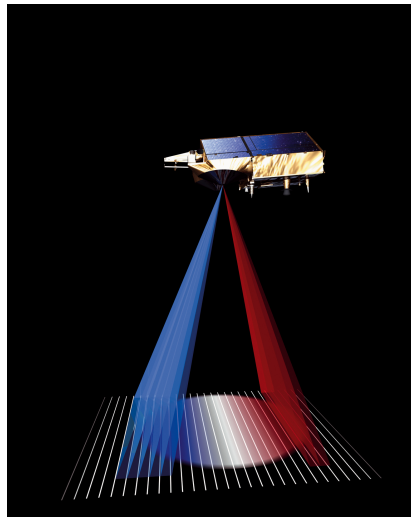


Figure 1.4: *Representation of the Footprint of an antenna. Credits: ESA*

These parameters depend strongly on several factors, including the size of the antenna, the wavelength used, and the distance between the antenna and the observed area.

In terms of wavelength, HF and VHF frequencies are generally used for ice and subsurface observation, and satellites used for this type of observation are located in Low Earth Orbit. Given these constraints on the distance and frequencies used, it is necessary to use antennas with a diameter of at least one kilometer to ensure a footprint on the order of one kilometer and, consequently, adequate performance. This kind of aperture would be impossible to achieve through the use of a monolithic satellite, so it becomes apparent that new solutions need to be explored.[2]

The technique of Synthetic Aperture Radar (SAR) has already been deeply explored for various applications. This involves collecting radar information from different viewpoints and then combining the data together to obtain a desired synthetic aperture. Nevertheless, in the case where only one satellite is used, which collects different information by moving along-track, the synthetic aperture obtained would be relative to only the direction of the motion.

Similar to SAR is the technique of Phased Array Beamforming, which involves the use of a single pulse and multiple radar elements, which sample information from different points.

It is possible to combine these two techniques by placing satellites in an across-track configuration and exploiting the SAR technique to sample in the along-track direction, while using the Phased Array Beamforming technique in the across-track direction as to create a two-dimensional mapping of the signal.

Using this technique, it is possible to obtain the desired footprint in multiple directions, providing significantly better performance.

Thus, it becomes evident the great opportunity that formation flight could represent in these kinds of applications.

The system thus defined will determine its definition and footprint as a function of the maximum distance of the satellites in the constellation, the shape and levels of the sidelobes (which define the shape of the radiation pattern of the antenna) in correlation with the relative positioning of the satellites, and the gain as a function of the number of satellites in the system.

In order to realize this kind of system and be able to take advantage of its benefits, it is necessary to know precisely the instantaneous position of each satellite in the formation, precisely controlling its orientation and relative position to the other elements in the formation.

Therefore, in order to achieve this performance, it is necessary for the systems used to possess autonomous active control, allowing periodic check of the system's status with corrections that can restore the desired conditions by limiting propellant consumption and, consequently, increasing mission duration. [3]

Depending on how system control is generated, two different architectures can be distinguished:

- **Centralized architecture:**

A single satellite, called chief, takes over most of the computation, limiting inter-satellite communications but definitely increasing the computational load.

- **Decentralized architecture:**

Computations are distributed among the various satellites, lowering the computational power required but requiring effective communication among the various elements of the formation.

1.3 Advantages of Tethered Space Systems

As mentioned, tethered systems are special distributed space systems in which formation flight is facilitated by the presence of a tether connecting two or more satellites.

The first to envision the idea of tethers for space use was Konstantin Tsiolkovsky in 1895 [4], who hypothesized how the presence of mechanical links could conserve the mechanical energy of the system.

The presence of the tether (a thin, strong cable that can extend up to several kilometers in length [5][6]) provides additional control over the system since the relative position can be managed by retracting the cable. This allows greater control of the formation, without the need for the use of propellant.

Thanks to the mechanical link of the various satellites, it is also possible to exploit some of the effects of external perturbations on the system. In fact, by placing a tethered system in a radial configuration, it is possible to exploit the gravitational gradient to achieve stabilization of the system.[7] [8]

This type of configuration, studied in various research works, is particularly advantageous because it makes it possible to build a large system which requires very little propellant for corrective maneuvers.

As demonstrated by Mazouz et al [9], a tethered system requires a mass of propellant to maintain pointing and orbit over a 5-year period of about one-tenth of that required by an Heilix formation (which represents the most stable formation [3]). Taking advantage of these features, the interest in developing an EndFire Array type system [10] based on a radially placed tethered system becomes apparent: placing several antenna elements in an aligned manner would result in a strongly directional radio antenna, the stability of which would be guaranteed by the stabilizing effect of the gravitational gradient, ensuring excellent performance with little corrective maneuvering.



Figure 1.5: *Schematic representation of an EndFire Array arranged radially*

1.4 Work Subdivision

This section will describe the topics approached in this study, analyzing the points covered in each chapter summarizing the research work carried out during a 6-month internship at NASA Jet Propulsion Laboratory.

- This **first chapter** discussed the advantages of developing distributed space systems, analyzing their possible applications for remote sensing by looking at some already tested examples, and looking at the possible advantages of a tethered system for an application in Earth observation.
- In the **second chapter**, the mathematical concepts necessary to fully understand the study performed will be approached, and the various reference frames that will be used to describe the kinematics of the system will be introduced.
- The **third chapter** will introduce all the physical models used to describe the EndFire system dynamics in low Earth orbit: first, the models used to describe perturbations in low Earth orbit will be defined, then the model to describe the dynamics of a tether will be discussed, and, finally, we will deduce the equations of relative dynamics, implemented in the algorithm.
- The **fourth chapter** will introduce the structure of the code used to simulate a tethered system. Its operation and the results of a simulation will be described, and then we will analyze the steps taken to carry out a numerical optimization of the latter, so as to improve its performance.
- In the **fifth chapter**, the results of an uncertainty propagation analysis performed by Monte Carlo methods will be discussed. In this analysis, it will be seen how freely the system evolves in response to some initial uncertainties both kinematically and on system characteristics.
- In the **sixth chapter**, a feasibility study on an EndFire system positioned across-track will be addressed. After checking its instability, the possibility of applying optimal control to hold it in place will be observed, and the forces required will be analyzed.

- In the **seventh chapter**, we will look at the possibility of using aerodynamic forces to stabilize the EndFire system positioned in a across-track configuration. We will analyze the aerodynamic surfaces needed to develop the required forces and determine the possibility of actively controlling the system using moving surfaces on the two leading satellites.
- In the **conclusion**, the most important results obtained in this research work will be summarized and possible future studies of this type of system will be discussed.

Chapter 2

Mathematical Notation and Reference Frames

In the study that will be analyzed in this research work, because of the different nature of the forces involved and the complex kinematics of the systems in analysis, different reference frames were used.

Each reference frame used is particularly suited to the study of certain phenomena, and makes it easier to represent the vector representation of forces and displacements acting on the system. Nevertheless, it is necessary to point out how the use of different reference frames leads to the need to use a notation that makes it intuitive to the reader in which reference system a given quantity is being analyzed.

The objective of this section is therefore to illustrate the notations used to represent the position and attitude of the systems under analysis and the different reference frames used in this study.

2.1 Vectors and Vectrices

As mentioned earlier, the use of different reference frames leads to the need to unambiguously represent in which frame a certain quantity is represented. For this reason we will introduce Hughes' notation of vectrix.

Each vector represents a certain quantity characterized by an amplitude and direction in a three-dimensional environment. This will be represented by three different components, expressed in a given reference system. By choosing a group of three versors (vectors of unit amplitude) that are orthogonal, it is possible to define a reference frame using vectrix notation.

In this paper, vectors will be represented with a bold letter \mathbf{v} , versors with the notation $\hat{\mathbf{v}}$, and the vectrix representation of the reference frame \mathcal{F} with the symbol $\hat{\mathcal{F}}$.

Using this notation, with three perpendicular versors $\hat{\mathbf{a}}_1, \hat{\mathbf{a}}_2, \hat{\mathbf{a}}_3$ we can obtain a vectrix representation for the frame \mathcal{F}_a as:

$$\hat{\mathcal{F}}_a \triangleq [\hat{\mathbf{a}}_1, \hat{\mathbf{a}}_2, \hat{\mathbf{a}}_3]^T \quad (2.1)$$

It is then possible to represent a vector \mathbf{v} with respect to this reference frame:

$$\mathbf{v} = v_1 \hat{\mathbf{a}}_1 + v_2 \hat{\mathbf{a}}_2 + v_3 \hat{\mathbf{a}}_3 \quad (2.2)$$

Where v_1, v_2 and v_3 represent the components of \mathbf{v} along the versors $\hat{\mathbf{a}}_1, \hat{\mathbf{a}}_2$ and $\hat{\mathbf{a}}_3$. We can then represent the vector \mathbf{v} in the \mathcal{F}_a reference frame as a column composed of these three components:

$$\mathbf{v}_a \triangleq [v_1, v_2, v_3]^T \quad (2.3)$$

Consequently we will have:

$$\mathbf{v} = \mathbf{v}_a \hat{\mathcal{F}}_a = \hat{\mathcal{F}}_a^T \mathbf{v}_a \quad (2.4)$$

2.2 Rotation Matrices

As we have just seen, it is possible to represent any vector with respect to a given reference system using the concept of vectrix. Working with different reference frames, however, it is readily apparent that there is very often a need to represent the same quantity in a different frames. To do this it is necessary to introduce the concept of rotation matrix.

Considering the \mathcal{F}_a reference system represented as vectrix $\hat{\mathcal{F}}_a$, we can observe that:

$$\hat{\mathcal{F}}_a \cdot \hat{\mathcal{F}}_a^T = \begin{bmatrix} \hat{\mathbf{a}}_1 \cdot \hat{\mathbf{a}}_1 & \hat{\mathbf{a}}_1 \cdot \hat{\mathbf{a}}_2 & \hat{\mathbf{a}}_1 \cdot \hat{\mathbf{a}}_3 \\ \hat{\mathbf{a}}_2 \cdot \hat{\mathbf{a}}_1 & \hat{\mathbf{a}}_2 \cdot \hat{\mathbf{a}}_2 & \hat{\mathbf{a}}_2 \cdot \hat{\mathbf{a}}_3 \\ \hat{\mathbf{a}}_3 \cdot \hat{\mathbf{a}}_1 & \hat{\mathbf{a}}_3 \cdot \hat{\mathbf{a}}_2 & \hat{\mathbf{a}}_3 \cdot \hat{\mathbf{a}}_3 \end{bmatrix} = \begin{bmatrix} 1 & 0 & 0 \\ 0 & 1 & 0 \\ 0 & 0 & 1 \end{bmatrix} = I_3 \quad (2.5)$$

$$\hat{\mathcal{F}}_a \times \hat{\mathcal{F}}_a^T = \begin{bmatrix} \hat{\mathbf{a}}_1 \times \hat{\mathbf{a}}_1 & \hat{\mathbf{a}}_1 \times \hat{\mathbf{a}}_2 & \hat{\mathbf{a}}_1 \times \hat{\mathbf{a}}_3 \\ \hat{\mathbf{a}}_2 \times \hat{\mathbf{a}}_1 & \hat{\mathbf{a}}_2 \times \hat{\mathbf{a}}_2 & \hat{\mathbf{a}}_2 \times \hat{\mathbf{a}}_3 \\ \hat{\mathbf{a}}_3 \times \hat{\mathbf{a}}_1 & \hat{\mathbf{a}}_3 \times \hat{\mathbf{a}}_2 & \hat{\mathbf{a}}_3 \times \hat{\mathbf{a}}_3 \end{bmatrix} = \begin{bmatrix} 0 & \hat{\mathbf{a}}_3 & -\hat{\mathbf{a}}_2 \\ -\hat{\mathbf{a}}_3 & 0 & \hat{\mathbf{a}}_1 \\ \hat{\mathbf{a}}_2 & -\hat{\mathbf{a}}_1 & 0 \end{bmatrix} \quad (2.6)$$

Representing the vector \mathbf{v} , initially represented in the frame \mathcal{F}_a , in the frame \mathcal{F}_b we obtain:

$$\mathbf{v}_b = \hat{\mathcal{F}}_b \cdot \mathbf{v} = \hat{\mathcal{F}}_b \cdot \hat{\mathcal{F}}_a^T \mathbf{v}_a \quad (2.7)$$

We can then deduce the rotation matrix:

$$R_{ba} = \hat{\mathcal{F}}_b \cdot \hat{\mathcal{F}}_a^T \quad (2.8)$$

From the equations 2.5,2.8 we can deduce the property:

$$R_{ba}R_{ab} = \hat{\mathcal{F}}_b \cdot \hat{\mathcal{F}}_a^T \cdot \hat{\mathcal{F}}_a \cdot \hat{\mathcal{F}}_b^T = I_3 \implies R_{ab} = R_{ba}^{-1} \quad (2.9)$$

Furthermore, because the vectors that make up vectrces are orthonormal, we can highlight the property:

$$R_{ba}^T = R_{ba}^{-1} \implies R_{ab} = R_{ba}^T$$

Furthermore, because the vectors that make up vectrces are orthonormal, we can highlight the property:

$$R_{da} = R_{dc}R_{cb}R_{ba} \quad (2.10)$$

2.3 Rotating Reference Frame

The problem of changing the reference frame becomes more complicated when the second reference frame is in rotation with respect to the first.

Consider a reference frame \mathcal{F}_b , which has an angular velocity ω_{ba} with respect to \mathcal{F}_a . It becomes apparent to understand how, on the contrary, the reference frame \mathcal{F}_a appears to be in rotation with respect to \mathcal{F}_b , with an angular velocity $\omega_{ab} = -\omega_{ba}$. Because of this rotation we will be able to assert the appearance of a new component in the time derivatives. In fact, denoting by $\dot{\mathbf{v}}|_a$ the time derivative of \mathbf{v} in reference frame a and by $\dot{\mathbf{v}}|_b$ the time derivative of \mathbf{v} in reference frame b, we will have that:

$$\dot{\hat{\mathcal{F}}}_a|_a = 0 \quad \dot{\hat{\mathcal{F}}}_b|_b = 0 \quad (2.11)$$

$$\dot{\hat{\mathcal{F}}}_b|_a = \omega_{ab} \times \hat{\mathcal{F}}_a \quad \dot{\hat{\mathcal{F}}}_a|_b = \omega_{ba} \times \hat{\mathcal{F}}_b \quad (2.12)$$

Using matrix notation we obtain:

$$\dot{\hat{\mathcal{F}}}_b|_a = \Omega_{ab}\hat{\mathcal{F}}_a \quad \dot{\hat{\mathcal{F}}}_a|_b = \Omega_{ba}\hat{\mathcal{F}}_b \quad (2.13)$$

Where:

$$\omega = [\omega_1, \omega_2, \omega_3]^T \implies \Omega = \begin{bmatrix} 0 & -\omega_3 & \omega_2 \\ \omega_3 & 0 & \omega_1 \\ -\omega_2 & -\omega_1 & 0 \end{bmatrix} \quad (2.14)$$

We then obtain the relations for the time first derivative and time second derivative in the \mathcal{F}_a frame of a quantity expressed in the \mathcal{F}_b reference frame:

$$\dot{\mathbf{v}}|_a = \hat{\mathcal{F}}_b^T|_a \mathbf{v}_b + \hat{\mathcal{F}}_b^T \dot{\mathbf{v}}_b|_a = \hat{\mathcal{F}}_b^T (\dot{\mathbf{v}}_b|_a + \Omega_{ba} \mathbf{v}_b) \quad (2.15)$$

$$\ddot{\mathbf{v}}|_a = \hat{\mathcal{F}}_b^T (\ddot{\mathbf{v}}_b|_a + 2\Omega_{ba} \dot{\mathbf{v}}_b|_a + \dot{\Omega}_{ba}|_a \mathbf{v}_b + \Omega_{ba} \Omega_{ba} \mathbf{v}_b) \quad (2.16)$$

2.4 Quaternions

To obtain a more effective representation of the attitude of the systems in analysis, in the work conducted, quaternions were used.

These are a much better performing tool than Euler angles, classically used for attitude definition in rigid body dynamics. A quaternion is a vector composed of four components, of which three components represent the vector part and the fourth the scalar part:

$$\mathbf{q} \triangleq \begin{bmatrix} q_1 \\ q_2 \\ q_3 \\ q_4 \end{bmatrix} = \begin{bmatrix} \mathbf{e} \sin(\frac{\theta}{2}) \\ \cos(\frac{\theta}{2}) \end{bmatrix} = q_1 \hat{\mathbf{i}} + q_2 \hat{\mathbf{j}} + q_3 \hat{\mathbf{k}} + q_4 \quad (2.17)$$

thanks to quaternions, it is then possible to easily represent a rotation of amplitude θ in the direction \mathbf{e} . In this work we will use right-hand quaternions ($\hat{\mathbf{i}}\hat{\mathbf{j}}\hat{\mathbf{k}} = -1$). it is possible to perform some peculiar operations with quaternions, which make gold particularly convenient to use:

- **Norm of a Quaternion**

We can define the norm of a quaternion as:

$$\|\mathbf{q}\| = \sqrt{q_1^2 + q_2^2 + q_3^2 + q_4^2} \quad (2.18)$$

Considering the definition of the quaternion stated earlier, we can easily deduce how it has a unitary norm:

$$\|\mathbf{q}\| = 1$$

- **Conjugate and Inverse of a Quaternion**

Given a quaternion $\mathbf{q} = [q_1, q_2, q_3, q_4]^T$, we can define its conjugate \mathbf{q}^* and its inverse \mathbf{q}^{-1} :

$$\mathbf{q}^* = \begin{bmatrix} -q_1 \\ -q_2 \\ -q_3 \\ q_4 \end{bmatrix} \quad \mathbf{q}^{-1} = \frac{\mathbf{q}^*}{\|\mathbf{q}\|^2} \quad (2.19)$$

- **Multiplication between quaternions**

Given two quaternions $\mathbf{q}_1 = [q_{1,1}, q_{2,1}, q_{3,1}, q_{4,1}]^T$ and $\mathbf{q}_2 = [q_{1,2}, q_{2,2}, q_{3,2}, q_{4,2}]^T$, distinguishing their scalar (s_1, s_2) part and their vector part ($\mathbf{v}_1, \mathbf{v}_2$) as:

$$\mathbf{v}_1 = \begin{bmatrix} q_{1,1} \\ q_{2,1} \\ q_{3,1} \end{bmatrix} \quad s_1 = q_{4,1} \quad \mathbf{v}_2 = \begin{bmatrix} q_{1,2} \\ q_{2,2} \\ q_{3,2} \end{bmatrix} \quad s_2 = q_{4,2}$$

We can define the operation of product of quaternions \otimes as:

$$\mathbf{q}_1 \otimes \mathbf{q}_2 = \begin{bmatrix} s_1 \mathbf{v}_2 + s_2 \mathbf{v}_1 + \mathbf{v}_1 \times \mathbf{v}_2 \\ s_1 s_2 - \mathbf{v}_1 \cdot \mathbf{v}_2 \end{bmatrix} \quad (2.20)$$

- **Quaternion Rate**

It is possible to tie the derivative of a quaternion to the angular velocity of the reference system, using the concept of product of quaternions but extending the angular velocity vector with a fourth null component $\hat{\omega} = [\omega_1, \omega_2, \omega_3, 0]$:

$$\dot{\mathbf{q}} = \frac{1}{2} \mathbf{q} \otimes \hat{\omega} \quad (2.21)$$

Using the operations just introduced, it is possible to reconstruct the concept of a rotation matrix using quaternions. Indeed, let us imagine that we have the quaternion \mathbf{q} indicating the orientation of the reference frame \mathcal{F}_a with respect to \mathcal{F}_b . We can then describe in the reference frame a the vector \mathbf{v} , initially described in the reference frame b. To do this we perform the operation:

$$\mathbf{v}_a = \mathbf{q} \otimes \mathbf{v}_b \otimes \mathbf{q}^* \quad (2.22)$$

This operation can be easily reversed:

$$\mathbf{v}_b = \mathbf{q}^* \otimes \mathbf{v}_a \otimes \mathbf{q} \quad (2.23)$$

Given the analogy with the rotation matrices introduced earlier, it can be shown that, given two reference systems \mathcal{F}_a and \mathcal{F}_b , and the quaternion \mathbf{q} describing their reciprocal orientation, it is possible to define the rotation matrix R_{ba} as:

$$R_{ba} = \hat{\mathcal{F}}_b \cdot \hat{\mathcal{F}}_a^T = \begin{bmatrix} 1 - 2(q_2^2 + q_3^2) & 2(q_1 q_2 - q_4 q_3) & 2(q_1 q_3 + q_4 q_2) \\ 2(q_1 q_2 + q_4 q_3) & 1 - 2(q_1^2 + q_3^2) & 2(q_2 q_3 - q_4 q_1) \\ 2(q_1 q_2 - q_4 q_2) & 2(q_2 q_3 + q_4 q_1) & 1 - 2(q_1^2 + q_2^2) \end{bmatrix} \quad (2.24)$$

2.5 Reference Frames

In this section we are going to analyze all the reference systems used in this study. All the vector quantities that will be discussed in this study will be expressed according to one of these reference systems, which will be referred to as the vector subscript. All the reference systems introduced are composed of a triplet of right-handed, unitary versors, consequently, it will be possible to apply the mathematical transformations described earlier to move from one reference system to another.

2.5.1 Earth Centered Inertial (ECI)

The Earth Centered Inertial reference frame (figure 2.1) is a quasi-inertial reference system, fixed with respect to the stars. The versors that compose this reference system are defined as:

- $\hat{\mathbf{e}}_1$ that is pointed towards the Vernial Equinox;
- $\hat{\mathbf{e}}_3$ that is pointed towards the celestial North Pole;
- $\hat{\mathbf{e}}_2$ that completes the tern $\hat{\mathbf{e}}_2 = \hat{\mathbf{e}}_3 \times \hat{\mathbf{e}}_1$

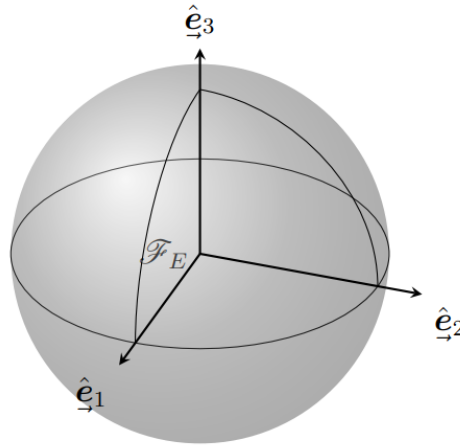


Figure 2.1: Graphical representation of the ECI reference frame

Due to the Earth's rotation, it is necessary to identify a specific instant in time to correctly define this reference frame, since in this way it is possible to uniquely define a mean equinox and the equator.

In our study we will use the J2000 frame, which refers to the earth's position at 12:00 on January 1st, 2000. Although ECI systems perform particularly well for describing the equations of orbital dynamics, this does not perform well for describing relative motion between satellites, which is particularly important for our study.

Using the versors defined earlier, we can then describe this reference system as a vectrix:

$$\hat{\mathcal{F}}_E = [\hat{\mathbf{e}}_1, \hat{\mathbf{e}}_2, \hat{\mathbf{e}}_3]^T$$

We can also mention that, in some cases, to best represent perturbations, it is preferable to use a reference system that rotates with the earth. In this case we will talk about Earth Centered - Earth Fixed (ECEF). This reference system will be similar to ECI but will use True of Date (TOD) to define the position of equator and mean equinox.

2.5.2 Local Vertical - Local Horizontal (LVLH)

As mentioned in the previous case, terrestrial reference systems do not suit well for the description of relative motion between satellites. This is due to the fact that these introduce large distances and velocities. Therefore, to describe near-field dynamics, it is necessary to introduce an Orbital Reference Frame (ORF), which follows the center of mass of the satellite under consideration.

The Local Vertical - Local Horizontal (LVLH) reference frame (figure 2.2) is an ORF oriented according to the instantaneous position of the satellite with respect to the earth. we can define the versors:

- $\hat{\mathbf{o}}_1 = \frac{\mathbf{R}}{\|\mathbf{R}\|}$ that is pointed toward the instantaneous radial direction;
- $\hat{\mathbf{o}}_3 = \frac{\mathbf{R} \times \mathbf{R}}{\|\mathbf{R} \times \mathbf{R}\|}$ that is pointed toward the direction of angular momentum;
- $\hat{\mathbf{o}}_2$ that completes the tern $\hat{\mathbf{o}}_2 = \hat{\mathbf{o}}_3 \times \hat{\mathbf{o}}_1$

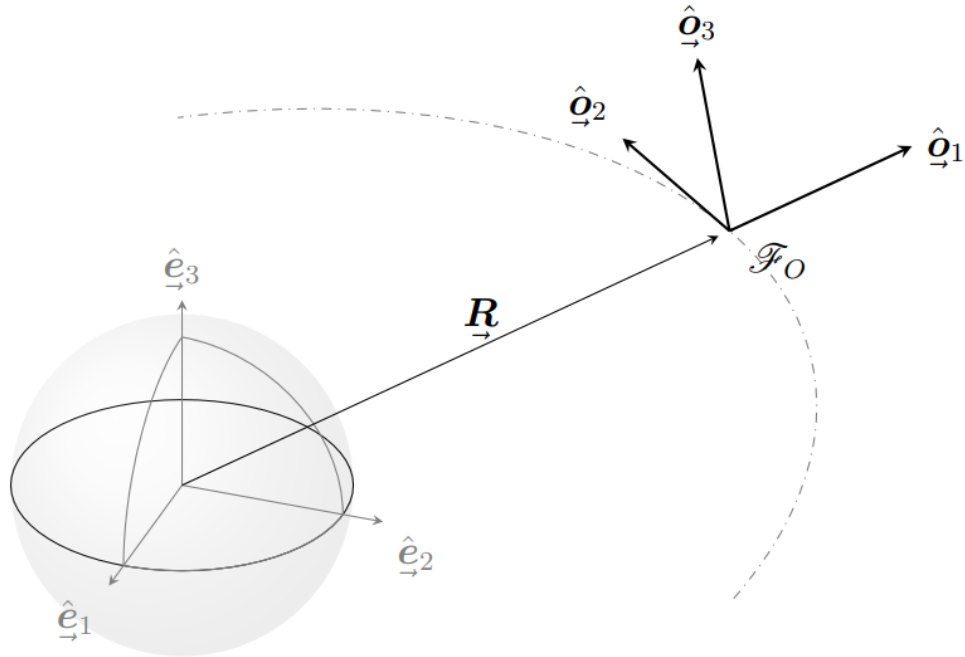


Figure 2.2: Graphical representation of the LVLH reference frame

As in the previous case, we can represent the system in the form of a vectrix:

$$\hat{\mathcal{F}}_O = [\hat{\mathbf{o}}_1, \hat{\mathbf{o}}_2, \hat{\mathbf{o}}_3]^T$$

2.5.3 Tether Frame (TF)

Since this research work is focused on the study of tethered satellites systems, it is essential to introduce a reference system that can best represent these systems.

In our case, the system is simply composed of several satellites connected by a single cable. To describe a cable connecting two satellites, it is necessary to know the position of its center of mass, its orientation and its length. By satellites m_1 and m_2 and their positions, respectively \mathbf{r}_1 and \mathbf{r}_2 , we can find the position of the center of mass \mathbf{r}_{CM} :

$$\mathbf{r}_{CM} = \frac{\mathbf{r}_1 m_1 + \mathbf{r}_2 m_2}{m_1 + m_2} \quad (2.25)$$

We can instead indicate the orientation and length of the wire by the vector $\boldsymbol{\tau} = \mathbf{r}_2 - \mathbf{r}_1$. From $\boldsymbol{\tau}$ it is then possible to define the versor $\hat{\boldsymbol{\tau}}_1 = \frac{\boldsymbol{\tau}}{\|\boldsymbol{\tau}\|}$.

It is then possible to obtain the Tether Frame (figure 2.3) from the two rotations of α (in-plane angle) around the axis $\hat{\mathbf{o}}_3$ and $-\beta$ (out-of-plane angle) around the axis $\hat{\mathbf{o}}_2$ necessary to make the radial vector of the LVLH frame $\hat{\mathbf{o}}_1$ coincide with the $\hat{\boldsymbol{\tau}}_1$ versor.

$$\hat{\mathcal{F}}_T = R_{TO} \hat{\mathcal{F}}_O = R_{\hat{\mathbf{o}}_3}(\alpha) R_{\hat{\mathbf{o}}_2}(-\beta) \hat{\mathcal{F}}_O \quad (2.26)$$

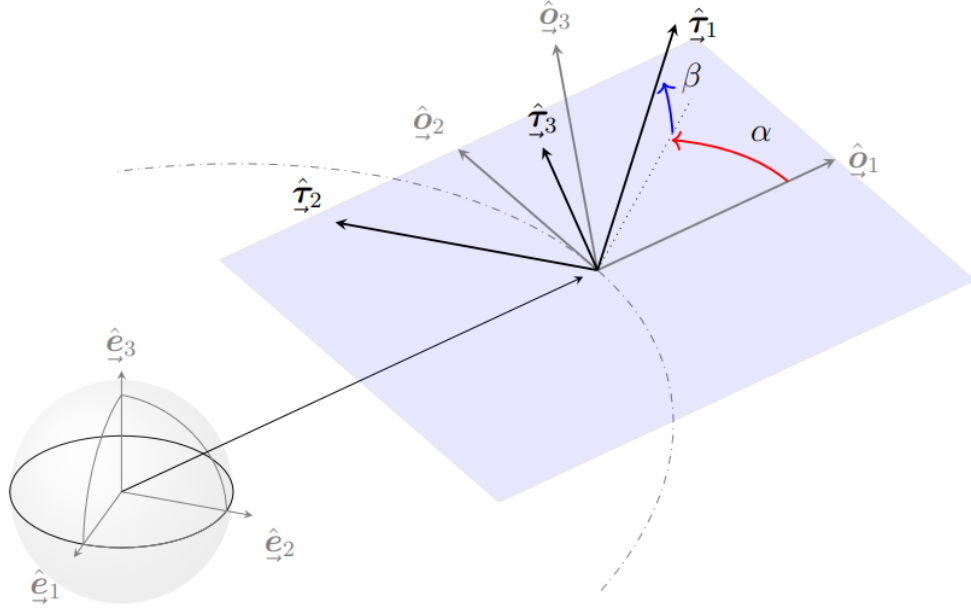


Figure 2.3: Graphical representation of the Tether Reference Frame compared with the LVLH frame and ECI frame

It is important to point out that these reference systems are time dependent, so it is necessary to calculate and every instant their relative position.

2.5.4 Body Frame (BF)

The last reference frame that will be used is the Body reference frame 2.4. This is particularly useful when it is necessary to estimate the position of the satellite, because most of the measurements made on the satellite are expressed in this reference frame.

This is centered at the satellite's center of mass, and its versors follow aerospace convention:

- $\hat{\mathbf{b}}_1$ that is pointed in the direction of the satellite's motion;
- $\hat{\mathbf{b}}_3$ that is pointed in the direction of the ground;
- $\hat{\mathbf{b}}_2$ that completes the tern $\hat{\mathbf{b}}_2 = \hat{\mathbf{b}}_3 \times \hat{\mathbf{b}}_1$

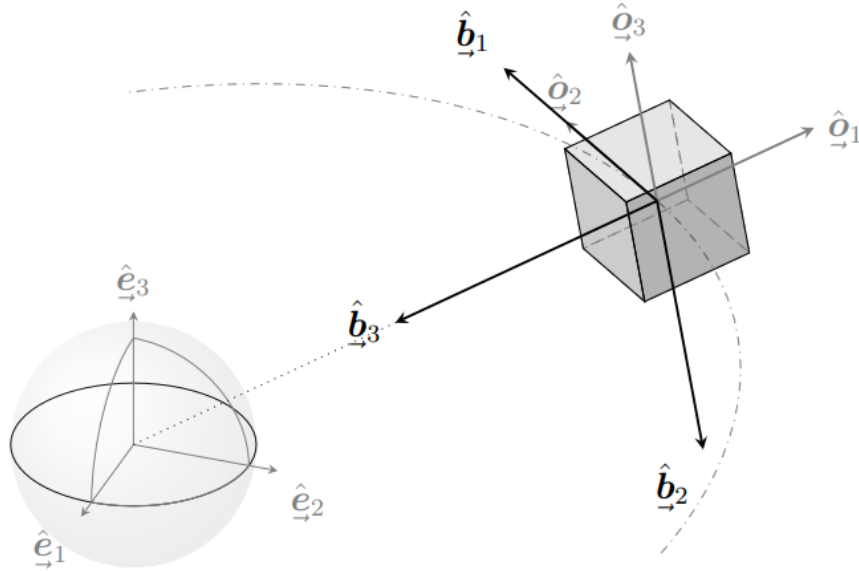


Figure 2.4: Graphical representation of the Body Reference Frame compared with the LVLH frame and ECI frame

It is finally necessary to point out that when it is required to extrapolate satellite attitude angles from quaternions, there is a need to consider the different convention used to measure Roll, Pitch and Yaw angles (RPY). To do this, it is necessary to multiply the quaternion to be converted by the quaternion \mathbf{q}_{Aero} :

$$\mathbf{q}_{RPY} = \mathbf{q}_{Aero} \otimes \mathbf{q} \quad (2.27)$$

Chapter 3

Kinematics and Kinetics

This chapter will introduce all mathematical modeling of the perturbations and forces that take part in TSS dynamics.

To do this, all the accelerations resulting from the external perturbations acting on the various satellites that compose the system will first be introduced. Then the modeling of the tether will be analyzed, deducing the equations necessary to determine the tensile forces acting on the system.

Once all the forces involved have been defined, the equations of motion will be introduced, dividing them between translation equations and rotation equations.

The following assumptions were made for this modeling:

- Satellites were considered as undeformable rigid bodies;
- The ORF reference frame follows an elliptical orbit, following the perturbations experienced by the system;
- The tensile tether tension was modeled as a linear spring; conversely, immediate buckling in compression was considered, thus considering the compressive force transmitted by the tether to be zero. A damper was added to this model to consider dissipation effects.

3.1 Modeling of External Forces

In this section, all the external forces involved in the dynamics of the problem under investigation will be analyzed. The mathematical models used for modeling and the formulas that will be implemented in the simulation code will then be described.

Precise calculation of the accelerations involved, using high-fidelity models, will result in simulations that will represent with good approximation the real behavior

of the system in orbit. All quantities presented here are expressed according to the ECI reference frame.

3.1.1 Earth's Gravitational Potential Perturbation

In the simplest models, the acceleration due to the earth's gravitational field is modeled by the gravitational force of a point mass positioned at the center of the earth. This acceleration can simply be calculated using the expression:

$$\mathbf{a}_G = -\frac{GM_\oplus}{r^3}\mathbf{r} \quad (3.1)$$

Where G denotes the gravitational constant, M_\oplus denotes the mass of the earth and \mathbf{r} the vector from the center of the earth to the center of mass of the body under consideration, the modulus of which is denoted by r .

Although this formula provides a good approximation for distances greater than $\tilde{22} \cdot 10^3 km$, it is necessary to use more accurate models when studying bodies closer to the earth. This is due to the fact that the earth is not perfectly spherical and is not composed of a homogeneous material; rather, it has a density that varies from point to point.

To obtain a correct assessment of the gravitational acceleration on the body, it would be necessary to integrate the gravitational force caused by each infinitesimal volume dv of the earth's volume::

$$\mathbf{a}_G = -G \int \frac{\rho(\mathbf{r})d\mathbf{v}}{r^3} \quad (3.2)$$

Where dv denotes the infinitesimal volume, $\rho(\mathbf{r})$ the density of that volume, and \mathbf{r} the vector indicating the distance between the volume and the body considered. Parameterizing the position of the satellite as a function of distance r , latitude ϕ and longitude λ , we can describe the gravitational potential by a Legendre polynomial of order n and degree m :

$$U = \frac{GM_\oplus}{r} \sum_{n=0}^{\infty} \sum_{m=0}^n \frac{R_\oplus^n}{r^n} P_{nm}(\sin \phi)(C_{nm} \cos(m\lambda) + S_{nm} \sin(m\lambda)) \quad (3.3)$$

Where R indicates the reference earth radius while the other parameters are defined as:

$$P_n(u) = \frac{1}{2^n n!} \frac{d^n}{du^n} (u^2 - 1)^n$$

$$C_{nm} = \frac{2 - \delta_{0m} (n - m)!}{M_\oplus (n + m)!} \int \frac{s^n}{R_\oplus^n} P_{nm} \sin(\phi') \cos(m\lambda') \rho(s) ds$$

$$C_{nm} = \frac{2 - \delta_{0m} (n - m)!}{M_{\oplus} (n + m)!} \int \frac{s^n}{R_{\oplus}^n} P_{nm} \sin(\phi') \sin(m\lambda') \rho(s) ds$$

Where δ denotes the Kronecker delta function.

Considering the coordinates in the ECI reference frame, it is possible to find the correlation with the parameters of longitude λ , latitude ϕ and distance r :

$$x = r \cos(\phi) \cos(\lambda)$$

$$y = r \cos(\phi) \sin(\lambda)$$

$$z = r \sin(\phi)$$

In the code used, harmonics up to the fourth order were used, considering that later harmonics represent a lower contribution of more than three orders of magnitude. It is necessary to give special importance to the C_{20} coefficient, generally called J_2 , which represents the most significant perturbation component.

To deduce the perturbative acceleration, it is then sufficient to calculate the gradient of the calculated potential via Legendre's polynomials:

$$\mathbf{a}_G = \nabla U \quad (3.4)$$

3.1.2 Atmospheric Drag Perturbation

Following the acceleration due to the gravity field, the most important force in low orbit is that caused by atmospheric friction. In fact, although at the heights considered the air is very rarefied, and, consequently, has a very small density, this is compensated for by the large velocities involved.

In order to accurately calculate this force, it would be necessary to know the exact density of the air lapping the body, the incidence of the satellite relative to the airflow, and the interactions between the satellite and the charged particles that characterize the upper atmosphere. For our simulations we will use a simple model that can represent these phenomena as easily as possible while not being numerically expensive.

To do this, to calculate the acceleration due to drag, the following formula will be used:

$$\mathbf{a}_D = -\frac{1}{2} \rho_{atm} \frac{C_d A}{m} \mathbf{v}_r^2 \frac{\mathbf{v}_r}{v_r} \quad (3.5)$$

Where ρ_{atm} denotes the atmospheric density, calculated according to the Harris-Priester model [11], C_d denotes the drag coefficient (considered constant $C_d = 2$), A is the reference surface of the satellite (also considered constant), m denotes the mass of the satellite, and V_r denotes the relative velocity between the satellite and the atmosphere.

The latter is calculated as the difference between the velocity of the satellite (\mathbf{v}) and that of the Earth's atmosphere (\mathbf{v}_{atm}) in ECI coordinates:

$$\mathbf{v}_r = \mathbf{v} - \mathbf{v}_{atm} \quad (3.6)$$

Where, denoting by ω_{\oplus} the earth's angular velocity and by \mathbf{r} the vector radius from the center of the earth to the satellite, the velocity of the atmosphere is obtained as:

$$\mathbf{v}_{atm} = \omega_{\oplus} \times \mathbf{r} \quad (3.7)$$

It is important to note that resistance is always opposed to the satellite's speed, causing it to continuously slow down. In terms of the orbit, this results in a decrease in the semi-major axis and a circularization of the orbit.

3.1.3 Solar Pressure Perturbation

Another perturbation considered in the simulations is that due to solar pressure. In fact, the absorption and reflection of photons emanating from the sun causes a pressure on each body exposed to its light.

To model this phenomenon, it is necessary to consider:

- The shadow factor ν , which takes into account the satellite's position relative to the earth's conical shadow pattern. This will be $\nu = 1$ if the satellite is in neither Umbra nor Penumbra, $0 < \nu < 1$ if it is in Penumbra, $\nu = 0$ if in Umbra (figure 3.1);

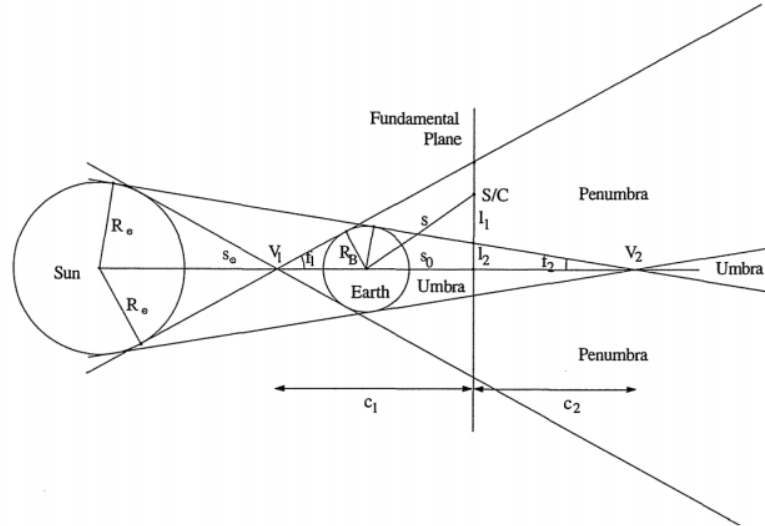


Figure 3.1: Model of the conical shadow

- The solar radiation pressure $P_{\odot} = 4.56 \cdot 10^{-6} \text{ N/m}^2$;
- The radiation pressure coefficient $C_r = 1 + \epsilon$, where ϵ is the reflectivity factor of the satellite surface. In the present case, $\epsilon = 0.1$ was considered;
- The mass of the satellite m ;
- The reference area of the satellite A ;
- The distance from the sun \mathbf{r}_{\odot} ;
- The astronomical unit AU .

We can then use the formula:

$$\mathbf{a}_{SP} = -\nu P_{\odot} C_r \frac{A \mathbf{r}_{\odot}}{m r_{\odot}^3} AU^2 \quad (3.8)$$

Using this formula, it is possible to achieve a good trade-off between accuracy and computation time, since there is not yet a final design for the constellation satellites and therefore it is not possible to identify the exact surface properties and size of the exposed area.

3.1.4 Third-body Perturbation

The last external perturbation considered in the model is third-body perturbations, which are perturbations due to the gravitational force of other celestial bodies. Specifically, for the problem examined, gravitational perturbations due to the sun and moon were considered.

In this case, since the system is at a very large distance from these celestial bodies, it is sufficient to consider the gravitational attraction of a point mass. We can then consider the equation:

$$\mathbf{a}_{TB} = GM \left(\frac{\mathbf{s} - \mathbf{r}}{|\mathbf{s} - \mathbf{r}|^3} - \frac{\mathbf{s}}{|\mathbf{s}|^3} \right) \quad (3.9)$$

Where G denotes the gravitational constant, M the mass of the celestial body for which we are calculating the third-body perturbation, \mathbf{r} the position of the satellite in geometric coordinates and \mathbf{s} the position of the celestial body in geocentric coordinates. The accuracy of the calculation strongly depends on the precision with which it is possible to calculate the position of the celestial body \mathbf{s} , considering the displacement of that body and the earth during the simulation.

3.2 Modeling of Internal Forces

This section will examine the model used to simulate the internal forces, which are the forces that are developed by the system itself. The main internal forces involved in the dynamics of the system under consideration are those related to the tether tension connecting the various satellites in the constellation and those related to the control forces, which are generated by actuators and inertia wheels to control the attitude and position of the system.

In contrast to the former, the latter are actuated on command to periodically correct the orbit and orientation of the satellite and thus ensure the successful continuation of the mission.

3.2.1 Discretized Mass Tether Model

The first internal force that will be analyzed is that due to the tether that connects the various satellites in the constellation. Before delving into this topic, however, it is necessary to explain the model used to represent the tether.

The tethers used for space applications are thin cables made of a highly corrosion-resistant material such as Kevlar or Wolfram.[5] To model the behavior of the tether there are several models, more or less complex, that succeed in describing the dynamics of the tether and the forces it develops on the various satellites in the constellation. In the current case, a discretized mass model will be used, which takes into account, therefore, the mass of the tether. Specifically, the discretization process used at Quadrelli will be used. [12][13][14]

Let s denote the material coordinate defining the length of the cable arc in the undeformed state and use subscript A to denote the end-mass closest to the earth and subscript B to denote the furthest (figure 3.2).

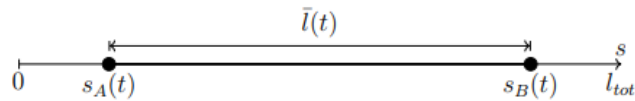


Figure 3.2: *Schematization of the undeformed tether and material coordinate s*

Through this modeling, it is possible to easily represent the tether contained within spacecraft A and the tether contained within spacecraft B, being denoted by coordinates, respectively:

$$0 < s(t) < s_A(t) \quad (3.10)$$

$$s_B(t) < s(t) < l_{tot} \quad (3.11)$$

Instead, the length of the exposed tether will be defined as $\bar{l}(t) = s_A(t) - s_B(t)$ and can be described by the coordinate $s_A(t) < s(t) < s_B(t)$.

It can be seen that, through this modeling, it is possible to vary the length of the tether simply by defining a time law for $s_A(t)$ and $s_B(t)$. With these material coordinates, it is then possible to describe a generic tether point as in the Orbital Reference Frame as $\boldsymbol{\rho}(s(t))$. To discretize the mass of the tether, a model that considers a constant number of nodes was used, whose mass is updated dynamically, so as to ensure a constant number of states in the system and ease the integration of the equations.

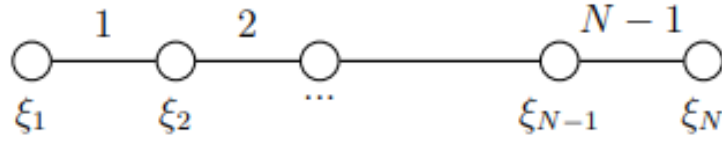


Figure 3.3: Schematization representing the discretization used for the tether mass

To do this, considering the discretization in N masses shown in the figure 3.3, the new variable ξ_i defined as:

$$\xi_i = \frac{i-1}{N-1} \quad \text{with } i = 1, 2, \dots, N \quad (3.12)$$

Using this new coordinate, it is possible to redefine the material coordinate and the position of the node in the ORF as:

$$s(t) = s_A(t) + \xi_i \bar{l}(t) \quad (3.13)$$

$$\boldsymbol{\rho}(s(t)) = \boldsymbol{\rho}(t, \xi) \quad (3.14)$$

In addition, it is possible to identify the i -th tether segment by the $\xi_i < \xi < \xi_{i+1}$ coordinate and the mass $m_i = \mu_t \Delta s = \mu_t (\xi_{i+1} - \xi_i) \bar{l}(t)$, where μ_t denotes the linear density of the tether.

The equations of dynamics, as will be explained in the next sections, will take into account the effects of this modeling by introducing terms dependent on ξ .

3.2.2 Tension Forces

Once the modeling used for the tether has been introduced, the model used to calculate the internal forces generated by the tether tension can be analyzed.

By indicating with increasing indices the satellites that make up the TSS, going from the one closest to the earth to the farthest away, we can define the strain in each tether segment as a function of orientation, strain, and strain rate. In fact, it is possible to indicate the direction of strain using the tether reference frame convention explained in the previous chapter. By denoting by $\boldsymbol{\rho}$ the position of the spacecraft at the ends of the tether segment we obtain:

$$\boldsymbol{\tau}_i = \frac{\boldsymbol{\rho}_{i+1} - \boldsymbol{\rho}_i}{\|\boldsymbol{\rho}_{i+1} - \boldsymbol{\rho}_i\|} \quad (3.15)$$

The tension of the i -th tether will be:

$$\mathbf{T}_i = EA(\epsilon_i + c_i \dot{\epsilon}_i) \boldsymbol{\tau}_i \quad (3.16)$$

Where E denotes the Young's modulus of the material composing the tether, A the cross section, ϵ_i the strain and $\dot{\epsilon}_i$ the strain rate. To define the latter quantities, it is necessary to use the undeformed length of the i -th \bar{l}_i segment, its mechanical stretch $l_{m,i}$ and its mechanical stretch rate $\dot{l}_{m,i}$ defined as:

$$l_{m,i} = \|\boldsymbol{\rho}_{i+1} - \boldsymbol{\rho}_i\| - \bar{l}_i \quad (3.17)$$

$$\dot{l}_{m,i} = (\dot{\boldsymbol{\rho}}_{i+1} - \dot{\boldsymbol{\rho}}_i) \cdot \boldsymbol{\tau}_i \quad (3.18)$$

It is then possible to define:

$$\epsilon_i = \frac{l_{m,i}}{\bar{l}_i} \quad (3.19)$$

$$\dot{\epsilon}_i = \frac{\bar{l}_i \dot{l}_{m,i} - \dot{\bar{l}}_i l_{m,i}}{\bar{l}_i^2} \quad (3.20)$$

It is necessary to emphasize that, in contrast to what happens in a spring, in the case of the tether the tension forces are present only in the case i which the cable is stretched. In the case of compression, in fact, it instantly goes into buckling, bringing the stress to 0 (figure 3.4).

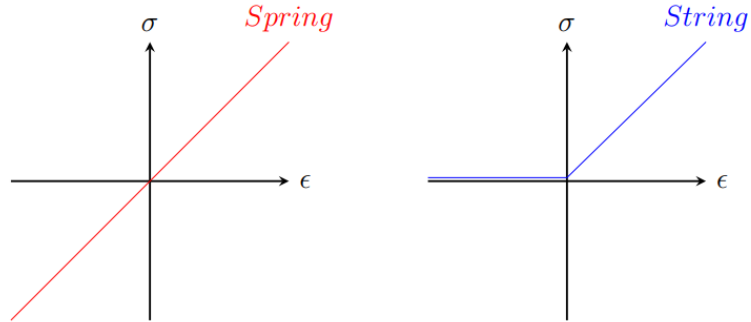


Figure 3.4: *Difference between stress modeling of a spring and a string*

3.2.3 Control Forces

Another category of internal forces involved in the dynamics of TSS is the control forces. These forces are used to control the position and attitude of the system, correcting all perturbations caused by external forces. For the presented problem, it was considered that the forces are generated by omnidirectional thrusters, which use cold gas technology. This type of actuators is widely used for satellite control because, despite having a rather low specific impulse, the system is very simple and easily integrated into small satellites.

To calculate the cost of keeping the constellation in orbit, thrusters characterized by a specific Pulse of $I_{sp} = 70$ s, whose maximum thrust is 1 N, were taken as reference. It was also assumed that the thrusters could be controlled with a 10 Hz frequency, keeping the thrust constant during each time step. The following equations were used to determine the mass cost of the maneuvers:

$$\dot{m} = \frac{T}{I_{sp}g_0} \quad (3.21)$$

Where \dot{m} denotes the fuel flow rate used, T the thrust provided by the thruster, I_{sp} the specific impulse, g_0 the gravitational acceleration at sea level.

By taking into account that $T = m \frac{\partial v}{\partial t}$ and integrating over the duration of the maneuver, we can obtain the *Tsiolkovsky* equation, which links the speed increment provided (ΔV) by the thruster to the amounts of propellant needed :

$$\Delta V = I_{sp}g_0 \ln \left(\frac{m_i}{m_f} \right) \quad (3.22)$$

Where m_i and m_f denote respectively the masses at the beginning and end of the maneuver.

For control torques, on the other hand, the use of reaction wheels was considered. These consist in electric motors that can modulate the reaction torque generated by putting a wheel into rotation to control the satellite's attitude. By using 3 perpendicular inertia wheels or 4 for redundancy, the attitude of each satellite can be perfectly controlled using only electric power. Nevertheless, it is necessary to consider that once these reach saturation speed, thrusters must be used to desaturate, thus implying consumption in terms of ΔV .

For a more accurate analysis of the dynamics of the system, it would be appropriate to also consider the gyroscopic torques generated by the rotating wheels, but this would generate a large increase in the computational cost. Considering the small magnitude of the torques generated, for the models under analysis it is possible to neglect these terms and not consider the dynamics of the wheels.

3.3 Equations of motion

Once all the internal and external forces acting on the system have been established, it is then possible to proceed and determine the equations describing the system's motions. To do this it will then be necessary to determine the equations for translation and rotation by selecting an appropriate reference frame. In the case under consideration, the Orbital Reference Frame was chosen to describe the position, velocity and attitude, and the Body Frame to indicate the angular velocity of each satellite.

This section will describe the steps performed to determine these equations.

3.3.1 Translational Dynamics

In order to describe the position r_i of a generic mass i , belonging to the system, in the ECI reference frame, it is possible to compose the vector R , which indicates the position of the center ORF reference frame with respect to the ECI reference frame, to the vector ρ_i , which indicates the position of the mass i in the ORF reference frame. Using the notation described in the previous chapter, we obtain the equation:

$$\hat{\mathcal{F}}_E^T \mathbf{r}_i = \hat{\mathcal{F}}_E^T \mathbf{R} + \hat{\mathcal{F}}_O^T \boldsymbol{\rho}_i \quad (3.23)$$

Since we want to determine the translation equations in the ECI reference frame, we derive in this frame, remembering that, as a result, $\dot{\hat{\mathcal{F}}}_E^T = 0$. We then obtain the equation:

$$\hat{\mathcal{F}}_E^T \dot{\mathbf{r}}_i = \hat{\mathcal{F}}_E^T \dot{\mathbf{R}} + \hat{\mathcal{F}}_O^T \dot{\boldsymbol{\rho}}_i + \hat{\mathcal{F}}_O^T \boldsymbol{\rho}_i \quad (3.24)$$

Considering that the ORF reference frame rotates with an angular velocity ($\boldsymbol{\Omega}$) with respect to the ECI system, we can deduce the derivative as demonstrated in the previous chapter, obtaining:

$$\hat{\mathcal{F}}_E^T \dot{\mathbf{r}}_i = \hat{\mathcal{F}}_E^T \dot{\mathbf{R}} + \hat{\mathcal{F}}_O^T (\boldsymbol{\Omega} \times \boldsymbol{\rho}_i + \dot{\boldsymbol{\rho}}_i) \quad (3.25)$$

A further derivation, again in the ECI reference frame, leads to the equation:

$$\hat{\mathcal{F}}_E^T \ddot{\mathbf{r}}_i = \hat{\mathcal{F}}_E^T \ddot{\mathbf{R}} + \hat{\mathcal{F}}_O^T (\dot{\boldsymbol{\Omega}} \times \boldsymbol{\rho}_i + \boldsymbol{\Omega} \times \boldsymbol{\Omega} \times \boldsymbol{\rho}_i + 2\boldsymbol{\Omega} \times \dot{\boldsymbol{\rho}}_i + \ddot{\boldsymbol{\rho}}_i) \quad (3.26)$$

At this point we can multiply everything by $\hat{\mathcal{F}}_O$, remembering that :

$$\hat{\mathcal{F}}_O \hat{\mathcal{F}}_O^T = I_{3 \times 3} \quad \hat{\mathcal{F}}_O \hat{\mathcal{F}}_E^T = R_{OE}$$

Isolating $\ddot{\boldsymbol{\rho}}_i$, we obtain:

$$\ddot{\boldsymbol{\rho}}_i = R_{OE} (\ddot{\mathbf{r}}_i - \ddot{\mathbf{R}}) - \dot{\boldsymbol{\Omega}} \times \boldsymbol{\rho}_i - \boldsymbol{\Omega} \times \boldsymbol{\Omega} \times \boldsymbol{\rho}_i - 2\boldsymbol{\Omega} \times \dot{\boldsymbol{\rho}}_i \quad (3.27)$$

With the obtained expression, it is then possible to represent the relative dynamics of a satellite of a generic constellation with respect to the ORF reference. In our specific case, the ORF reference is centered on the center of mass of the constellation. We can then make explicit the dynamics of the reference and the satellite under consideration in ECI coordinates, so as to substitute the expression of $\dot{\boldsymbol{\rho}}_i$ and $\ddot{\mathbf{R}}$ and thus specializing the equation for our case our tethered system model. To describe the dynamics in ECI coordinates, it is necessary to consider all the external accelerations listed in the previous paragraph and the tether stresses. In this case we neglect the control forces, considering the system in free evolution.

$$m_i \ddot{\mathbf{r}}_i = m_i (\mathbf{a}_G + \mathbf{a}_D + \mathbf{a}_{SP} + \mathbf{a}_{TB})_i + \mathbf{T}_i - \mathbf{T}_{i-1} \quad (3.28)$$

$$m_o \ddot{\mathbf{R}} = m_o (\mathbf{a}_G + \mathbf{a}_D + \mathbf{a}_{SP} + \mathbf{a}_{TB})_o \quad (3.29)$$

Subtracting the second equation from the first one results in:

$$\ddot{\mathbf{r}}_i - \ddot{\mathbf{R}} = \Delta \mathbf{a}_G + \Delta \mathbf{a}_D + \Delta \mathbf{a}_{SP} + \Delta \mathbf{a}_{TB} + \frac{\mathbf{T}_i - \mathbf{T}_{i-1}}{m_i} \quad (3.30)$$

By substituting in the equation (3.27) it is then possible to obtain the equation of specialized relative dynamics for our system:

$$\ddot{\boldsymbol{\rho}}_i = R_{OE} \left(\Delta \mathbf{a}_G + \Delta \mathbf{a}_D + \Delta \mathbf{a}_{SP} + \Delta \mathbf{a}_{TB} + \frac{\mathbf{T}_i - \mathbf{T}_{i-1}}{m_i} \right) - \boldsymbol{\Omega} \times \boldsymbol{\Omega} \times \boldsymbol{\rho}_i - 2\boldsymbol{\Omega} \times \dot{\boldsymbol{\rho}}_i \quad (3.31)$$

This equation then describes the dynamics of the i -th mass, for a system consisting of N masses and $N - 1$ tether segments. In the last expression, the Euler contribution was eliminated, since it is negligible ($\dot{\boldsymbol{\Omega}} \simeq 0$).

Terms due to the tether modeling explained in the previous chapter can then be added to this equation, resulting in the final version of the equations:

$$\begin{aligned} \ddot{\boldsymbol{\rho}}_i = & R_{OE} \left(\Delta \mathbf{a}_G + \Delta \mathbf{a}_D + \Delta \mathbf{a}_{SP} + \Delta \mathbf{a}_{TB} + \frac{\mathbf{T}_i - \mathbf{T}_{i-1}}{m_i} \right) \\ & - \boldsymbol{\Omega} \times \boldsymbol{\Omega} \times \boldsymbol{\rho}_i - 2\boldsymbol{\Omega} \times \dot{\boldsymbol{\rho}}_i \\ & - \frac{\dot{m}}{m} \dot{\boldsymbol{\rho}}_i + \frac{\mu_t}{m} \left[\frac{ds_{i+1}}{dt} \frac{\partial \boldsymbol{\rho}(s_{i+1}, t)}{\partial t} - \frac{ds_i}{dt} \frac{\partial \boldsymbol{\rho}(s_i, t)}{\partial t} \right] \end{aligned} \quad (3.32)$$

$$\dot{\boldsymbol{\rho}}_i = \mathbf{v}_i + \frac{\mu_t}{m} \left[\frac{ds_i}{dt} \boldsymbol{\rho}(\xi, t) + \frac{dl}{dt} \xi \boldsymbol{\rho}(\xi, t) \right]_{\xi_i}^{\xi_{i+1}} \quad (3.33)$$

3.3.2 Attitude Dynamics

For the description of the rotational dynamics of each satellite, quaternions (\mathbf{q}_i) and angular velocities ($\boldsymbol{\omega}_i$) were used. The former are defined with respect to the Orbital Reference Frame (ORF), while the latter are referred to the body frame of the satellite.

The expression described in the previous chapter (2.21) was used to bind these quantities. By indicating with $\hat{\boldsymbol{\omega}}_i$ the vector of angular velocities expanded with a zero at the end, it is possible to define the equation that binds the derivative of the attitude expressed as a quaternion to the angular velocity of the satellite.

$$\dot{\mathbf{q}}_i = \frac{1}{2} \mathbf{q}_i \otimes \hat{\boldsymbol{\omega}}_i \quad (3.34)$$

At this point, it is sufficient to define the rotational equation, taking into account external torques (\mathbf{t}_{ext}), the torques due to tether tension (\mathbf{t}_{tether}) and the rotation of the reference system. The equation obtained is thus:

$$\mathbf{J}_i \dot{\boldsymbol{\omega}}_i = -\boldsymbol{\omega}_i \times \mathbf{J}_i \boldsymbol{\omega}_i + \mathbf{t}_{ext} + \mathbf{t}_{tether} \quad (3.35)$$

Where \mathbf{J}_i denotes the inertia matrix of satellite i .

External torques (\mathbf{t}_{ext}) are caused mainly by solar pressure, atmospheric drag, and gravitational acceleration:

$$\mathbf{t}_{ext} = \mathbf{t}_G + \mathbf{t}_D + \mathbf{t}_{SP} \quad (3.36)$$

To calculate these perturbations, arbitrary application points were used so as to obtain orders of magnitude similar to the real ones. To do this, we relied on the data depicted in figure 3.5, considering a reference altitude of 500 kilometers.

In particular, the following approximations were made:

- Regarding the torques caused by perturbations due to atmospheric friction and solar pressure, constant arms were considered. The length of these was calculated such that, given the typical order of magnitude of these forces on LEO orbits, torques of the order of 10^{-5} [Nm] and 10^{-7} [Nm] are generated for solar pressure and drag, respectively. [8]
- Concerning the torques caused by Earth's gravitational perturbations, it was decided to deviate from the orders of magnitude suggested by the graph in the figure. This, in fact, indicates torques on the order of 10^{-3} , a value that is too high for small satellites characterized by an inertia of a few kgm^2 . This is because the graph is based on large satellites, and values for gravitational perturbations are not applicable to the nanosatellites that constitute the TSS

under consideration. Despite this, the balancing effect that gravitational torques have on pitch and roll was considered, assuming a nonhomogeneous mass distribution that guarantees the conditions $I_{z_b} < I_{y_b}$ and $I_{z_b} < I_{x_b}$, necessary to have this effect. Specifically, $I_{z_b} = 0.8I_{y_b}$ was considered. If we considered the whole system positioned radially, it would be observable how the inertia with respect to the I_{z_b} axis would be much less than that relative to the other two axes, resulting, therefore, in a large stabilizing torque due to gravitational acceleration. This characteristic makes the convenience of this type of configuration obvious.

- Regarding the torques applied on the masses representing the tether discretization, correction coefficients were introduced, which decrease the magnitude of these torques proportionally to their size.

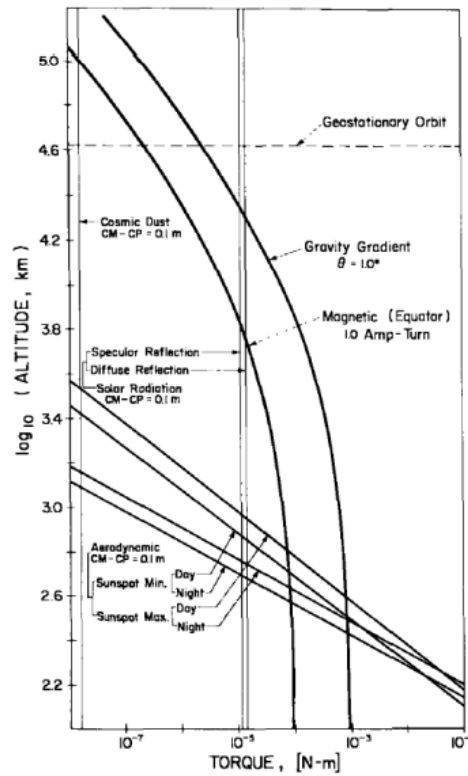


Figure 3.5: Representation of the most significant sources of torque in LEO orbit as a function of altitude referenced to the center of the earth. Credit: *Spacecraft Attitude Dynamics, Hughes P.C., pag 271 [8]*

The torque due to the tether (\mathbf{t}_{tether}) is simply calculated by considering the distance between the point where the tether is connected to the satellite and the center of mass. Denoting by \mathbf{d}_k the arm of the k -th tether and by \mathbf{T}_k the tension of the latter, considering a satellite connected with N_t tether we will obtain the equation:

$$\mathbf{t}_{tether} = \sum_{k=1}^{N_t} \mathbf{d}_k \times \mathbf{T}_k \quad (3.37)$$

Chapter 4

Numerical Simulation and Optimization

The development of software for the simulation of complex dynamical systems in order to obtain reliable results in a limited time is an issue of particular interest, because of the increasing complexity of these systems and the need to correctly predict their behavior in order to exploit their dynamics correctly and predict possible mission problems. To do this, it is necessary to carefully study the structure of the code used, both to optimize its operation and to avoid the incidence of bugs and numerical problems that could distort its results.

This chapter will review the architecture of the code used to obtain reliable simulations of the Tethered Space System and, subsequently, the optimization performed in order to limit the computation time required to compute the kinematics of complex dynamical systems.

The same architecture was used to develop both a `Matlab` and a `Python` code.

In the final part of this chapter the results of the optimization will be discussed, analyzing performance improvements.

4.1 Architecture of the code

In this first section of the chapter the structure of the code developed will be analyzed, highlighting its most important features and the methods used to manage and store the variables in an efficient and organized way.

The code can be decomposed into three main parts, which are composed in turn of different functions. To enable a consistent flow of information between these different sections of code, it was chosen to work using data structures, containing all the information about the simulation. Each section has access to the data structure processed by the previous section, extracts the information, processes it

in turn, and recreates a data structure for the next section.

To do this, *Structure Arrays* were used for the `Matlab` code, and *Dictionaries* for the `Python` version. Both of these data structures allow a simple and intuitive way of storing data of different form and extent. In fact, in both it is possible to locate a particular data item through a label that identifies it, saved as a string.

The three main sections of the code are:

- **Initialization** : this first section of the code acquires as input from the user all the options related to the simulation, processes them and organizes them in the structure called `EFData`. This information will then be passed to the section that performs the simulation.

- **Simulation** : from the data extracted from `EFData`, this section integrates the dynamics of the system, simulating its behavior over the required time interval. This section is the most time-consuming, and it is on this section that the optimization work was carried out. Once the simulation is completed, the contents of the `EFData` structure are correlated with the information obtained from the integration, resulting in the structure called `EFData_PP`.

- **Post Processing** : the processing of the data obtained from the integration takes place in this final section, so that the information can be drawn from it and represented clearly to the user. To do this, the data are extracted from `EFData_PP`, are analyzed, and are represented in a series of plots. In addition, the latter section allows the data to be saved at the user's request.

A schematization of the code structure can be seen in figure 4.1, summarizing the connections between its main elements.



Figure 4.1: *Schematization of code structure.*

Now that the general structure of the code has been explained, it is possible to explain specifically the individual roles of the various sections, analyzing the details of their operation.

4.1.1 Initialization

As introduced earlier, the functions used in this first section of code are intended to initialize the simulation by taking user input into account. The parameters chosen by the user govern different options of the simulations, in fact, it is possible to distinguish:

- **Time parameters** : these define the number of orbits to be simulated, the initial time (which option by default is January 1, 2030), and the time vector on which the simulation results are to be represented. The initial time, represented both as a *Datetime Array* and in *Modified Julian Date* format, has particular relevance in the calculation of perturbations, because from this it is possible to derive exactly the position of the sun and moon at each instant. The relative positions are needed to calculate precisely the density of the atmosphere used for atmospheric drag calculations (via the *Harris-Priester* model that takes into account the position of the sun), third-body perturbations, the shadow factor needed for solar pressure calculations, etc.

- **Orbital parameters** : these define the shape of the initial orbit, using *Keplerian parameters*. Indeed, mean altitude, eccentricity, inclination, argument of perigee and mean anomaly are defined. An orbit of an average altitude of 500 *km* quasi-circular ($e = 0.01$), inclination of 30 degrees is used as default options.

- **Type of formation** : is expressed by the user by a number indicating the type of configuration to be simulated. The various possible configurations differ in the type of system modeling, initial conditions, and system architecture. These various configurations define the number and type of bodies to be simulated, their location, and the size and orientation of the system. For the study conducted, an 11-mass model (2 to represent the satellites positioned at the ends and 9 to represent the discretization of the tether mass), positioned radially and with a total length of 1,000 meters, was predominantly used, but other models were later introduced for the study of particular configurations.

- **Accuracy of the model** : also expressed through a number from 1 to 5 by the user, indicates the precision to be used in the simulation. In the simplest model, only the effects due to the gravitational field are considered for the calculation of relative dynamics. In the other models more and more perturbations are gradually introduced, until reaching model 5, which includes

gravitational effects up to the fourth harmonic, atmospheric drag, solar pressure and third-body perturbations.

- **Control parameters** : the user can also specify whether to perform a simulation of a free propagation of the system or to simulate the operation of a control law. In the latter case, an attitude control or orbital control can be performed.

From these simulation options, the code calculates the total mass and initial conditions of the system. Using these data, an initial integration of the dynamics equations is performed by evolving in ECI coordinates a virtual satellite, which will represent the origin of the Orbital Reference Frame during the rest of the simulation. Through this integration, a reference orbit will then be generated, and, from this, reference data can be obtained that will then be used during the integration of the relative dynamics. Starting from the position of the center of the ORF, it is also possible to deduce its angular velocity and angular acceleration by means of the model of *Xu and Wang 2008*.^[15]

It is necessary to emphasize, however, that this model has validity only as long as the accelerations acting on the body are relative to the gravitational acceleration alone, considered up to the harmonic J2. For this reason, the dynamics of the center of the ORF takes into account only this perturbation.

Nevertheless, following the equations of dynamics described in the previous chapter, it is still possible to consider all desired perturbations in the relative dynamics, because this is affected only by the difference between the accelerations experienced by the ORF and those experienced by the satellite.

If requested by the user, the control law is also calculated in this section. To do this, a linear model of the system is derived and the variation in control forces over time on the various satellites is then calculated. Chapter 6 will look specifically at the methodology used to define the linear model and the synthesis of the control law, which is used to control a system aligned in the across-track direction.

Finally, this section also generates matrices that index the degrees of freedom of the system. These matrices are used to easily and conveniently define the position in the state vector of a given degree of freedom.

All of this data is then collected in the structure called `EFDData` (*End-Fire Data*), which is passed to the next code section in order to perform the integration. It is useful to highlight how within this structure all of the information useful for performing the integration is already present, and in the case where only minor changes from nominal case are to be made, it is sufficient to make minor changes to this structure. This particular feature proved particularly convenient when performing the different iterations of the Uncertainty Propagation study carried

out with Monte Carlo analysis. This is due to the fact that, since the random variations affected only some parameters of this structure, in the various iterations it was sufficient to change the desired parameter by generating a variation of the nominal `EFData`, without having to generate a new structure each time, which would require a new integration each time to determine the reference orbit.

4.1.2 Simulation

Once the simulation is initialized, the integration of the system of ordinary differential equations is carried out in this section of code.

From the data contained in `EFData`, a state vector is created, respecting the indices defined in the previous section and converting the initial conditions first imposed in the `State0` state vector.

This vector will consist of a number of elements proportional to the number of bodies modeled and the number of degrees of freedom considered for each body. In the more complex case, in which N masses are modeled considering translation and attitude, the first $7N$ components will represent the translation and rotation degrees of freedom of each satellite (3 components for translation and 4 for rotation for each body), while from the $7N + 1$ to the $13N$ component ($6N$ components in total) will represent the linear velocity and angular velocity of each satellite (3 components for translation and 3 for rotation for each body). These will be followed by $N - 1$ states representing the different tether segments and a last state representing the derivative of the total length of the tether. The state vector will then consist of $14 N$ components.

$$X = \begin{bmatrix} \boldsymbol{\rho}_1 \\ \mathbf{q}_1 \\ \dots \\ \boldsymbol{\rho}_N \\ \mathbf{q}_N \\ \dot{\boldsymbol{\rho}}_1 \\ \boldsymbol{\omega}_1 \\ \dots \\ \dot{\boldsymbol{\rho}}_N \\ \boldsymbol{\omega}_N \\ l_1 \\ \dots \\ l_{N-1} \\ \dot{L} \end{bmatrix} \quad \text{where:} \quad \boldsymbol{\rho}_i = \begin{bmatrix} x_i \\ y_i \\ z_i \end{bmatrix}_{ORF} \quad \mathbf{q}_i = \begin{bmatrix} q_{1,i} \\ q_{2,i} \\ q_{3,i} \\ q_{4,i} \end{bmatrix}_{ORF} \quad \boldsymbol{\omega}_i = \begin{bmatrix} \omega_{x,i} \\ \omega_{y,i} \\ \omega_{z,i} \end{bmatrix}_{BF} \quad (4.1)$$

The derivative of the state is calculated by the function `eom_EndiFire_HP`. This function, using the information contained in `EFData` and knowing the state in the

current condition, calculates the value of this derivative expressing it as a vector of the same size as the state vector, using the formulas explained in the previous chapter.

This derivative is then integrated using variable-step numerical integration algorithms, which are present by default as built-in functions in the respective programming languages. The choice of integration algorithm is particularly important for problems with complex dynamics, so this topic will be discussed in more detail in the section on numerical optimization.

This integration will provide as output a vector containing the times and a matrix containing the state evolution over time. These are then appended to the information already contained in the structure `EFDData`, thus creating the structure `EFDData_PP`, which will be analyzed in post-processing in order to derive useful information for analysis.

4.1.3 Post Processing

As previously mentioned, the purpose of this section of code is to extract all useful information from the simulation results and represent them in a clear and intuitive way through plots. Obviously, in order to do this, it is necessary to process this data to make it more readable.

According to the model used, the evolution of the state is represented in ORF coordinates, the center of which does not represent a real satellite, but is just a material point that undergoes gravitational attraction only (up to the J2 harmonic) so that analytical formulas can be used to predict the orientation of the axes without further complicating the calculations.

On the contrary, the bodies represented in this reference frame are subject to all the accelerations due to the perturbations presented above. This necessarily causes the system to move away from the center of the ORF during the simulation. In order to avoid problems with the readability of the graphs representing the evolution of the position of the masses over time, it was chosen to represent it with respect to the position of the center of mass of the system and not with respect to the center of the ORF, which is used only to correctly calculate the relative dynamics during integration.

By knowing the evolution of the position and velocity of all bodies in the Orbital Reference Frame, it is possible to calculate the position and velocity of the center of mass of the system in this Frame:

$$x_{cm} = \frac{\sum_{i=1}^N x_i m_i}{\sum_{i=1}^N m_i} \quad y_{cm} = \frac{\sum_{i=1}^N y_i m_i}{\sum_{i=1}^N m_i} \quad z_{cm} = \frac{\sum_{i=1}^N z_i m_i}{\sum_{i=1}^N m_i} \quad (4.2)$$

$$\dot{x}_{cm} = \frac{\sum_{i=1}^N \dot{x}_i m_i}{\sum_{i=1}^N m_i} \quad \dot{y}_{cm} = \frac{\sum_{i=1}^N \dot{y}_i m_i}{\sum_{i=1}^N m_i} \quad \dot{z}_{cm} = \frac{\sum_{i=1}^N \dot{z}_i m_i}{\sum_{i=1}^N m_i} \quad (4.3)$$

It is then possible to translate all quantities with respect to the position and velocity of this point:

$$x'_i = x_i - x_{cm} \quad y'_i = y_i - y_{cm} \quad z'_i = z_i - z_{cm} \quad (4.4)$$

$$\dot{x}'_i = \dot{x}_i - \dot{x}_{cm} \quad \dot{y}'_i = \dot{y}_i - \dot{y}_{cm} \quad \dot{z}'_i = \dot{z}_i - \dot{z}_{cm} \quad (4.5)$$

However, it is necessary to point out that this approximation is valid only as long as the system remains relatively close to the center of the ORF. The orientation of the instantaneous horizontal and vertical axis are calculated with respect to the center of the ORF, and, if the system is too far away from this the results could be misleading (figure 4.2). By all means, given the number of orbits simulated in this study and the maximum distance between the center of the ORF and the center of mass of the system, it is possible to consider this model a good approximation. In the case where larger distances intervene, it would be necessary to change the model, centering the ORF in the center of mass and calculating its instantaneous point-by-point orientation during integration. This, however, would increase the number of states and, consequently, the code would be more time-consuming.

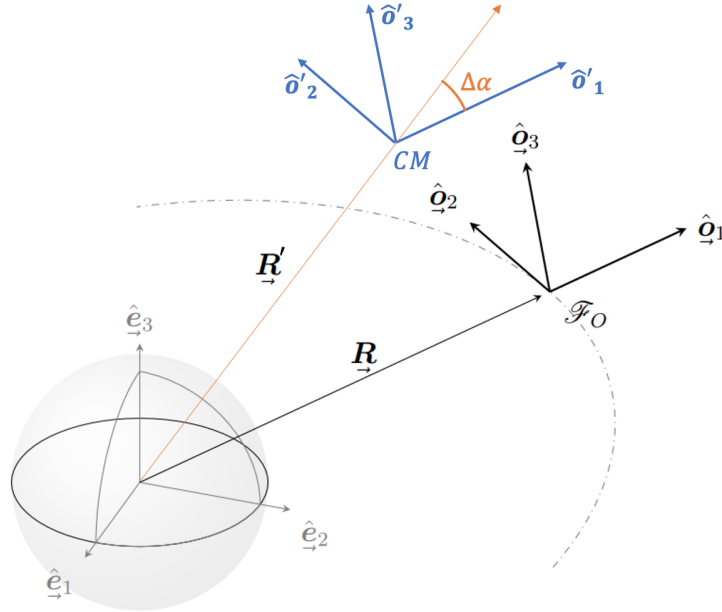


Figure 4.2: Schematization of the error ($\Delta\alpha$) between the real horizontal and vertical axes and those of the ORF that incurs when the system moves too far away from it.

Once the data have been reprocessed, they are represented in different plots. The main plots provided as output by the post processing function are:

- Evolution of radial, along-track and across-track position of different bodies, represented with respect to the center of mass of the system;
- Evolution of radial, along-track and across-track velocity of different bodies, represented with respect to the center of mass of the system;
- Evolution of α (in-plane angle) and β (out-of-plane angle) representing the orientation of the EndFire array with respect to the ORF;
- The evolution of the orientation of different satellites, expressed both as quaternions referred to the ORF and as Roll, Pitch and Yaw;
- Evolution of angular velocities for each satellite, expressed in the body reference frame;
- Evolution of total tether length (L);
- In the case where the system is controlled, the evolution of forces and control torques acting on each satellite.

In addition to these plots, it is also possible to obtain data on a spectral analysis of tether oscillations and oscillations in terms of alpha and beta. Another function has been specially developed to make plots in case of Monte Carlo simulation for uncertainty propagation (which will be analyzed in the next chapter). In that case the nature of the data will be different, because the results of several simulations will have to be analyzed simultaneously, and histograms and plots will be provided as output to describe the evolution of uncertainty over the course of the orbits. Before finishing the execution of the code, it is also possible to save the data obtained in the simulation by exporting them by creating files in ".mat" format. Thanks to this function, it will then be possible to save the results of multiple simulations for later comparison.

4.2 Numerical optimization

This section will describe the process carried out to numerically optimize the code. In the first part we will describe how the first simulation was set up and describe the computational time problems that emerged, then we will describe the modal analysis performed to justify the detected computational time problem and describe the steps taken to solve it.

4.2.1 Simulation parameters

The code was then tested by performing a simulation of an orbit considering an 11-mass system positioned radially: 2 masses represent the satellites placed at the ends of the EndFire array while the remaining 9 represent the tether discretization. A schematic representation of the system can be seen in the figure 4.3.

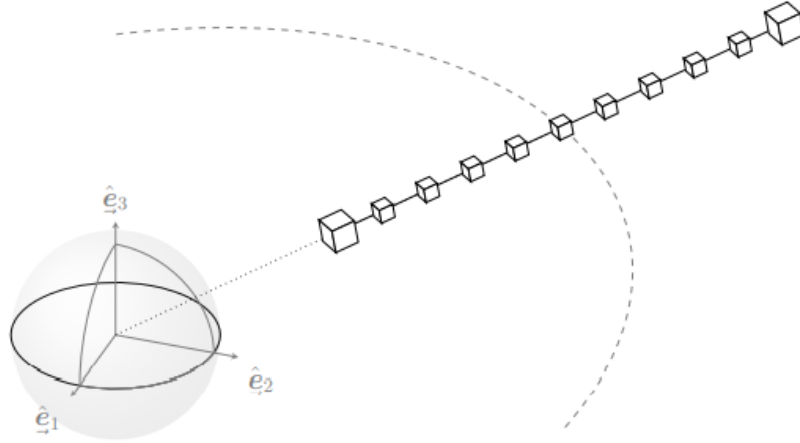


Figure 4.3: *Non-scale representation of the 11-mass EndFire array.*

To model the satellites and tether lumps in these simulations, the physical quantities contained in the two tables 4.1 and 4.2 were considered.

		Satellite
Mass	kg	100
Side length	m	0.5
Inertia matrix	kg m ²	$\begin{bmatrix} 4.1667 & 0 & 0 \\ 0 & 4.1667 & 0 \\ 0 & 0 & 3.3334 \end{bmatrix}$

Table 4.1: *Satellite characteristics*

		Tether lumps
Mass	kg	1
Side length	m	0.1
Inertia matrix	kg m ²	$\begin{bmatrix} 0.0017 & 0 & 0 \\ 0 & 0.0017 & 0 \\ 0 & 0 & 0.0014 \end{bmatrix}$

Table 4.2: *Tether lumps characteristics*

The data in table 4.3 were used for the tether, data that are analogous to those used by Quadrelli and Lorenzini for their study of a Kevlar tether.

Length	m	1000
Linear Density	kg/km	10
Diameter	mm	1.7
Young Modulus	GPa	20.844
Axial Stiffness	N	47312
Damping	Ns	47.312
Static Friction	-	0.374
Dynamic Friction	-	0.264

Table 4.3: *Tether characteristics*

Finally, the reference orbit is described by the orbital parameters in table 4.4.

Semi-major Axis	km	6940.5
Eccentricity	-	0.01
Inclination	deg	30
Right Ascension of Ascending Node	deg	0
Argument of Periapsis	deg	0
Initial Anomaly	deg	0

Table 4.4: *Orbit characteristics*

In this first simulations, Matlab's ode113 integrator was used, with an absolute tolerance of 10^{-6} and letting the integrator choose the necessary time steps so as to ensure convergence of the solution with the required accuracy.

4.2.2 Analysis of Results and Computational time

The results obtained through this simulation will then be analyzed, representing the most important plots. Specifically, we represent here the results for the evolution of the radial, along-track and across-track position of all 11 simulated masses expressed in relation to the position of the center of mass.

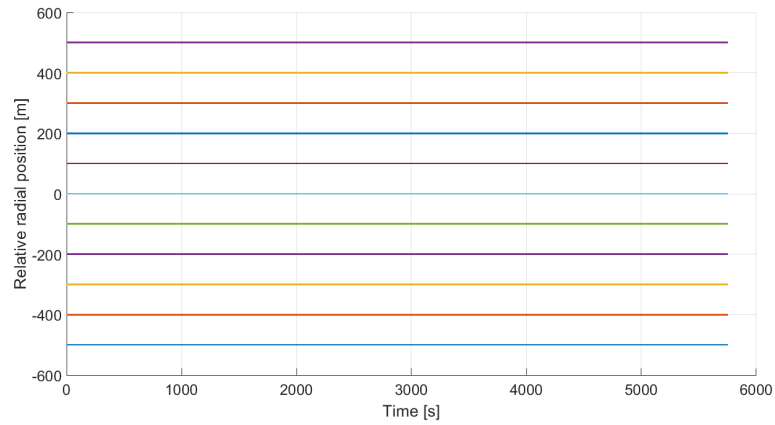


Figure 4.4: Evolution of the radial position of the 11 masses representing the EndFire Array. The graph is referred to the center of mass of the system.

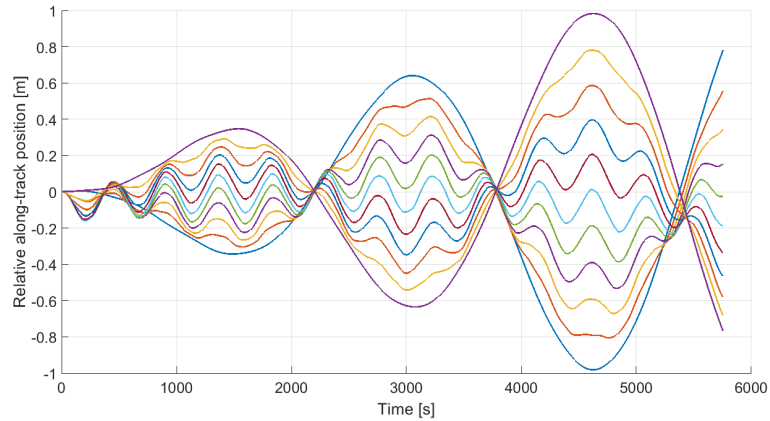


Figure 4.5: Evolution of the along-track position of the 11 masses representing the EndFire Array. The graph is referred to the center of mass of the system.

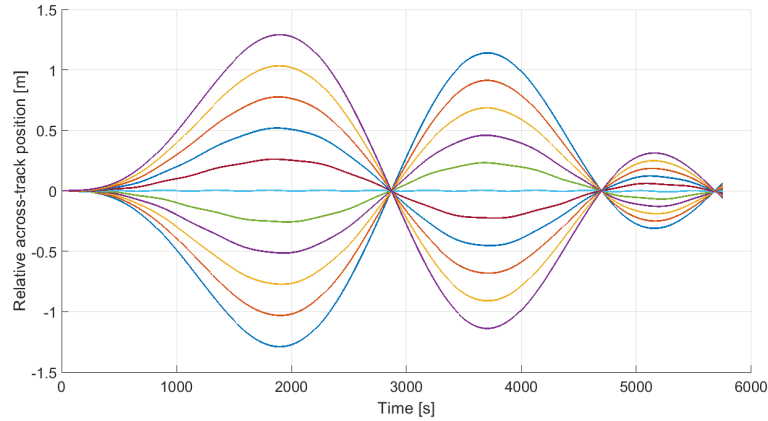


Figure 4.6: Evolution of the across-track position of the 11 masses representing the EndFire Array. The graph is referred to the center of mass of the system.

As we can see in the figure 4.4, the radially positioned EndFire array is stable, preserving orientation as predicted by theory. Furthermore, by analyzing Figures 4.5 and 4.6, we can observe oscillatory motions in the along-track and across-track directions, which are characterized by the superposition of oscillations at different frequencies.

From these results we can then verify the correctness of the written code, which provides an accurate representation of the system dynamics, similar to that obtained in other research on this configuration.

Despite this, if looking at the computational time taken by the code, it is immediately apparent that this is very time-consuming. The algorithm took more than 19 minutes to obtain the presented data, initially obtained without taking into account the rotational dynamics, presenting the solution on 222 411 points. Through Matlab's *Profiler* function, it is possible to analyze how the main cause of this phenomenon is due to the integration algorithm, which needs to evaluate the function calculating the derivative more 476 476 times to obtain a result that converges correctly with the required accuracy.

This issue becomes even more evident when we also introduce the attitude simulation, which, further complicating the problem, brings the time the required time to almost 7 hours, using 1 910 139 points and evaluating the function that calculates the derivative 4 803 986 times. It is therefore evident that the integration method used is not efficient, but in order to explain correctly understand what causes this problem, it is necessary to perform a modal analysis on the dynamics of the system.

4.2.3 Frequency Analysis of TSS Dynamics

Considering the configuration of the EndFire array described in the previous section, it is possible to determine the different modes to which the system is subjected. As shown by the studies of Quadrelli and Lorenzini [16], and by the analysis carried out by Pastori [17], the main frequencies involved in this kind of problem are due to pendular motion, the natural frequency of a mass-spring system, and the frequency of transversal and longitudinal oscillations intervening on a cable subject to tension, which is perturbed by external forces.

It is therefore necessary to analyze these different modes one at a time, analytically describing a typical frequency expression as a function of the quantities that characterize the system:

- **Pendular motion**

Pendular motion of the system is characterized by two modes, one occurring in the orbital plane, affecting α (in-plane angle), the other occurring outside the orbital plane, affecting β (out-of-plane angle). Both of these modes are proportional to the average orbital rate Ω :

$$f_{in-plane} = \frac{1}{2\pi} \sqrt{3\Omega^2} \quad (4.6)$$

$$f_{ou-of-plane} = \frac{1}{2\pi} \sqrt{4\Omega^2} \quad (4.7)$$

- **Spring-mass system**

It is easy to see how this configuration, consisting of two satellites connected by a cable, creates a spring-mass system. The mode of this system is characterized by a natural frequency which is a function of the stiffness of the spring " K_t " (in this case the tether) and the equivalent mass " m_{eq} ", calculated as a function of the masses of the satellites alone (m_1 and m_2), neglecting the masses of the tether lumps. It is necessary to point out how this mode is present only in tension and not in compression, since it is a cable and not a real spring.

$$K_t = \frac{EA}{L} \quad m_{eq} = \frac{m_1 \cdot m_2}{m_1 + m_2} \quad (4.8)$$

$$f_{spring-mass} = \frac{1}{2\pi} \sqrt{\frac{K_t}{m_{eq}}} \quad (4.9)$$

- **Longitudinal and Transversal oscillation**

As mentioned this type of motion intervenes when there is the presence of external perturbations on the tether, and it is necessary to take these

frequencies into account when the system has more than 4 tether lumps. The frequencies of these longitudinal and transverse modes are proportional, respectively, to the elastic constant and mass of the tether (E and A) and the average tension to which it is subjected (T). Moreover, in both cases we have a dependence with the distance between the different nodes (l_t), their mass (m_t) and their number (N_t). It is possible to calculate these frequencies with analytical formulas:

$$f_{longitudinal} = \frac{1}{\pi} \sqrt{\frac{EA}{m_t l_t}} \sin\left(\frac{n\pi}{2(N_t + 1)}\right) \quad (4.10)$$

$$f_{transversal} = \frac{1}{\pi} \sqrt{\frac{T}{m_t l_t}} \sin\left(\frac{n\pi}{2(N_t + 1)}\right) \quad (4.11)$$

By introducing the reference values for the system under consideration, the formulas described can be used to calculate the frequency of the analyzed modes. The frequencies of the described modes are observed in the table 4.5, considering $n = 1, 2, 3, 4$ for Longitudinal and Transversal modes.

Mode	Frequency [Hz]
Libration (in-plane)	$3.07 \cdot 10^{-4}$
Libration (out-of-plane)	$3.55 \cdot 10^{-4}$
Transversal (1st)	$2.2 \cdot 10^{-3}$
Transversal (2nd)	$4.4 \cdot 10^{-3}$
Transversal (3rd)	$6.5 \cdot 10^{-3}$
Transversal (4th)	$8.4 \cdot 10^{-3}$
Spring mass	0.15
Longitudinal (1st)	1.08
Longitudinal (2nd)	2.14
Longitudinal (3rd)	3.14
Longitudinal (4th)	4.07

Table 4.5: *Natural frequencies of the modes of the system under examination.*

The same modes were analyzed in Pastori's study, which verified the presence of these through spectral analysis on simulations on the free oscillation of this type of system.

The presence of these modes, characterized by such a wide range of frequencies, justifies the oscillatory phenomena visible in the simulation results, and, as will be seen in the next section, explains the difficulty in integration encountered with the `ode113` algorithm.

4.2.4 Choice of Integration Method

As seen, several modes with a large frequency range intervene in the dynamics of the tether. The overall kinematics of the tether is generated by the superposition of these modes, which make the solution strongly oscillatory. For solving these kinds of ODE systems, classical integration methods are not optimized, often requiring a large number of points to properly integrate the solution ensuring that it does not diverge.

This issue was precisely the cause of the problem in the integration time of this first version of the code. Although `ode113` is a good integrator, able to efficiently provide a solution in the case where there are stringent tolerances and fairly expensive functions to evaluate, this is not optimal for stiff ODE systems, which require special techniques of solving. For this reason, it was decided to test all the methods of solving for stiff equations found in Matlab.

An analysis was then conducted to compare the performance of the different integration algorithms; specifically, an orbit was chosen to be simulated, neglecting attitude and using the same parameters as described in the paragraph above.

Again, it was chosen to use an absolute tolerance of 10^{-6} and to leave the integrator free to choose the necessary time step.

Using the Matlab Profiler, it was possible to obtain the data in the table 4.6.

	time [s]	N of nodes	N of evaluations
<code>ode15s</code>	137.231	27 749	57 089
<code>ode23s</code>	>7200	-	>2 000 000
<code>ode23t</code>	15.254	923	6 347
<code>ode23tb</code>	48.147	864	19 925

Table 4.6: Comparison of the performance of different `matlab` built-in integration methods for systems of stiff equations.

As can be seen, the `ode23t` method provides the best performance, and was therefore used as the integrator in the Matlab version of the code.

However, for the Python version, it was chosen to use the integration methods for stiff ODE systems contained in the `Scipy.solve_ivp` package. Specifically, the *LSODA* method was implemented, which guarantees automatic detection of the stiffness of a ODE system and adapts the method to integrate the system as efficiently as possible.

4.2.5 Results of the optimization

Thanks to the code optimization carried out, it was possible to improve the performance of the code by far. Although the results were already astounding (taking less than one seventieth of the original time), these are even more evident in simulations of longer periods.

As can be seen in the figure 4.7, the optimization of the choice of integration method makes it much easier to obtain results for longer simulations. Indeed, as the simulation time increases, the benefits of optimization are more evident, as they are not linear with respect to the number of orbits simulated.

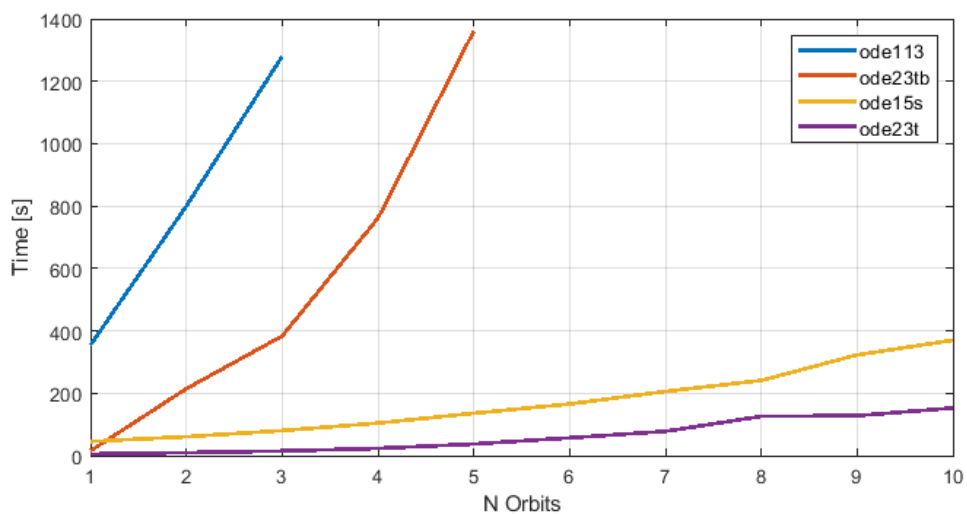


Figure 4.7: Comparison of the integration time required by different integration methods against the number of orbits simulated

It is important to note that the data obtained for the graph in the figure were calculated during the execution of the code without using the Profile application of Matlab. By not having to count the individual calls of the various functions and not having to measure the time spent within each function, the actual computation time is smaller than that measured by the Profiler.

Also the Python code, using proper integration methods, manages to obtain results in similar times as Matlab. Although the two codes manage to simulate the evolution of the system at a similar number of points, the time taken by Python for an evaluation of the function to be integrated is longer (~ 5 ms for Python vs the ~ 2 ms for Matlab), thus making it inconvenient to use this code.

Nevertheless, this still represents a good alternative, given the vast number of libraries on Python and their possible implications on the study under consideration.

As a result of this work, it was then possible to obtain a code capable of providing results for medium-term simulations in moderate computation times. This made possible the study described in the next chapter, during which a Monte Carlo analysis was performed to study uncertainty propagation for a freely propagating EndFire Array.

Chapter 5

Monte-Carlo Analysis on Uncertainty Propagation

Obtaining accurate and precise simulation for the study of complex-dynamics systems, as mentioned in the previous chapter, is particularly important. Indeed, it is necessary to be able to predict the behavior of the system in such a way that any problems in the mission can be effectively prevented. Although the code described in the last chapter makes it possible to obtain accurate predictions of the behavior of the system by accurately simulating its evolution over time, this considers a perfect knowledge of the characteristics of the system, both in terms of its initial conditions and in terms of the physical characteristics of the satellites that compose it. For this reason, it is necessary to introduce a study that analyzes how the system responds to a certain initial uncertainty, so that its sensitivity to certain parameters that affect its dynamics can be observed. [18]

This chapter will describe the uncertainty propagation study performed on an EndFire Array system consisting of 11 masses. In the first part we will describe the methodology used for this analysis, and then in the second part we will present the results for uncertainties on the initial position of the constellation (α, β) and then on its physical characteristics (m, A, CD, CR) .

5.1 Methodology applied in the study

A similar study has already been carried out by Apa et al [19] for the analysis of a Helix satellite formation. For the study of the latter, the *DACE*[20] toolbox was used, which allows the dynamics of the system to be analyzed with algorithms based on *Differential Algebra*. [21] The use of this toolbox is particularly convenient since it allows to greatly lower the computational time required for the study. In fact, through this method, once the final state has been mapped, it is possible to

evaluate the effect of an initial uncertainty in as little time as a single evaluation of a polynomial function. For this reason, using Differential Algebra, performing a study of uncertainty propagation using Monte-Carlo methods is particularly convenient (DA based Monte-Carlo). After the initial mapping, a very large number of samples can easily be obtained with minimal computing power.

The initial idea of this work was to implement an algorithm based on Differential Algebra for the study of uncertainty propagation of an EndFire Array system, so that the great advantages of the DACE toolbox in terms of computational time could be used to be able to evaluate the response of the system to an initial uncertainty. Unfortunately, however, this was not possible. DACE, in fact, allows the work with systems composed of up to 20 states, a number too small for a tethered system, which, as seen, implies the use of a much larger state vector. The study of Helix formations of multiple satellites has been possible due to the fact that the dynamics of each body is not affected by the other elements in the constellation, so it is sufficient to perform an uncertainty study on one satellite at a time and then pool the results. For a tethered system this is not possible because, due to the mechanical constraint that binds the various bodies in the system, the dynamics of each satellite is highly dependent on the others.

Therefore, a study on uncertainty propagation using classical Monte-Carlo methods was chosen for the problems described.

This was possible due to the code optimization described above, thanks to which it is possible to obtain the results of a simulation in a modest amount of time.

In spite of this, it was necessary to change a little bit the parameters of the simulations so that results could be obtained in a useful time. In fact, 500 samples were used for each study (as opposed to 2000 used for the Helix formation study), and the number of simulated orbits was limited to 10 (as opposed to 25 simulated for the Helix formation). Nevertheless, the results between the two cases are still comparable, having modified similar characteristics.

For all simulations performed, the same parameters as described in the tables 4.1, 4.3, 4.2, 4.4 were taken into account, considering a system with 11 masses.

An uncertainty was then added to these values for the parameter analysed, modelled as a zero mean Gaussian noise. Using the results obtained from the different simulations, it is possible to approximate the evolution of the main statistic moments (Mean " μ " and Covariance " P ") using the expressions :

$$\begin{cases} \mu = \frac{1}{N} \sum_{i=0}^N X_{f,i} \\ P = \frac{1}{N-1} \sum_{i=0}^N (X_{f,i} - \mu)(X_{f,i} - \mu)^T \end{cases} \quad (5.1)$$

By evaluating these moments, it will then be possible to understand how an initial uncertainty about the system affects the time evolution, and how this changes over time.

5.2 Position Uncertainties

In this section, the system's response to uncertainties relating to its initial position will be analysed. Specifically, the response of the EndFire system to an uncertainty relating to its initial orientation will be observed.

In the study of the Helix formation, the uncertainty on the initial position was modelled in terms of the uncertainty on the position of the different satellites with respect to the orbital reference frame. In the case of the tethered system, since the various masses are bound together by a mechanical link, considering an independent variation on the position of the various bodies has little physical sense, since it would result in an initial tension in the tether that would be unnatural.

For this reason, a study was carried out on an uncertainty about the overall position of the system, which is a more realistic and useful case.

Specifically, the system's response to an uncertainty related to the in-plane angle (α) and out-of-plane (β) angle was analyzed, observing how this uncertainty propagates throughout the 10 orbits simulated.

5.2.1 Uncertainty on the In-plane Angle (α)

The first uncertainty simulated is the in-plane angle. To do this, data from 500 simulations were collected, which considered the system with a starting state located radially ($\alpha = 0, \beta = 0$), on which there was an uncertainty on the alpha with a standard deviation of 1 degree (figure 5.1).

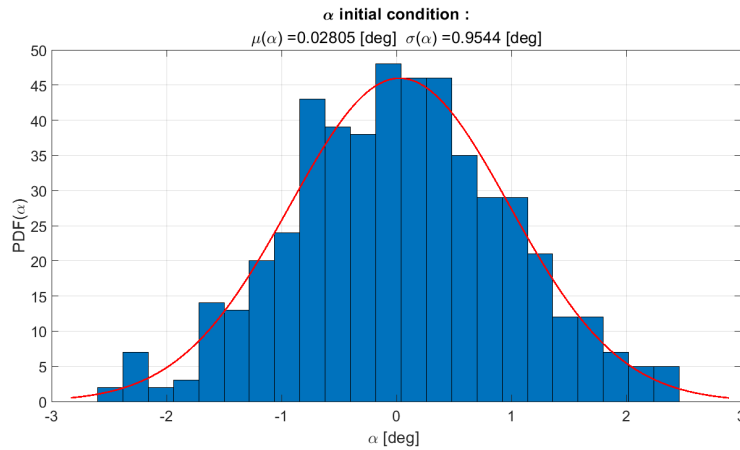


Figure 5.1: Distribution of in-plane angle for the initial condition of the different samples employed.

An equal number of simulations were then obtained from these 500 samples. These, due to small differences in the initial conditions, led to different evolution. In the

figures 5.2, 5.3 we can observe all the different final states of the different samples after the 10 orbits simulated.

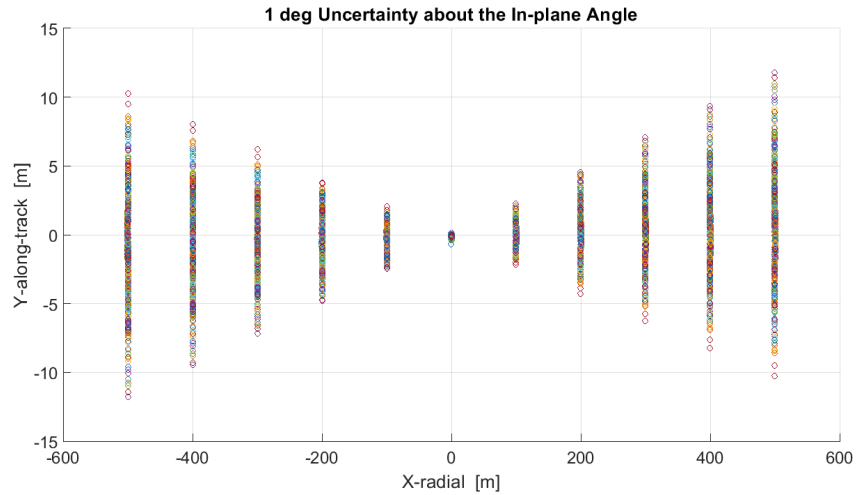


Figure 5.2: Representation of the final condition (after 10 orbits) of the 500 samples differing in the initial condition of the in-plane angle (X - Y plane)

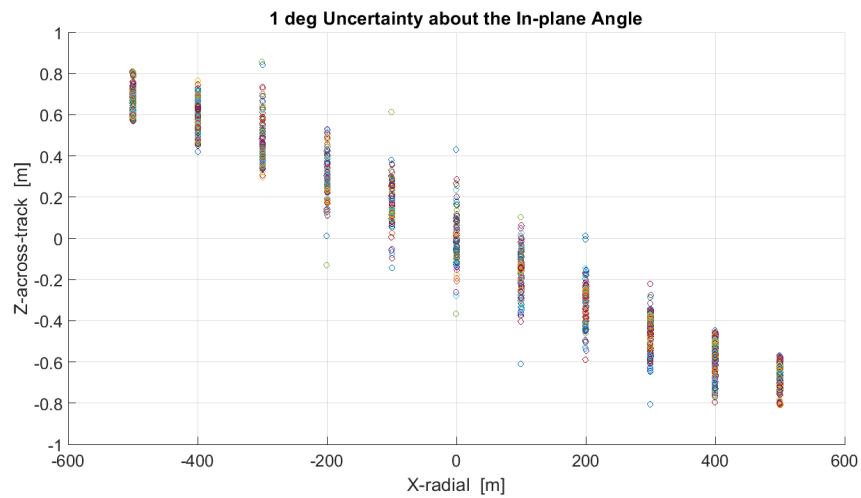


Figure 5.3: Representation of the final condition (after 10 orbits) of the 500 samples differing in the initial condition of the in-plane angle (X - Z plane)

From these different simulations, the evolution of the standard deviation of the two angles was extrapolated, which can be seen in the figure 5.4

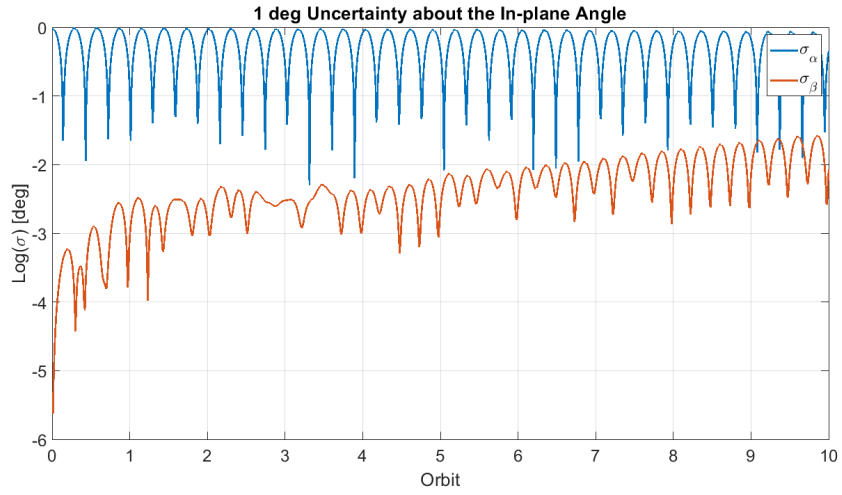


Figure 5.4: Evolution of the standard deviation of the α and β angles due to an uncertainty in the in-plane angle.

5.2.2 Uncertainty on the Out-of-Plane Angle (β)

For the out-of-plane angle, simulations similar to those carried out for the in-plane angle were performed, this time, however, considering the uncertainty on β (figure 5.5).

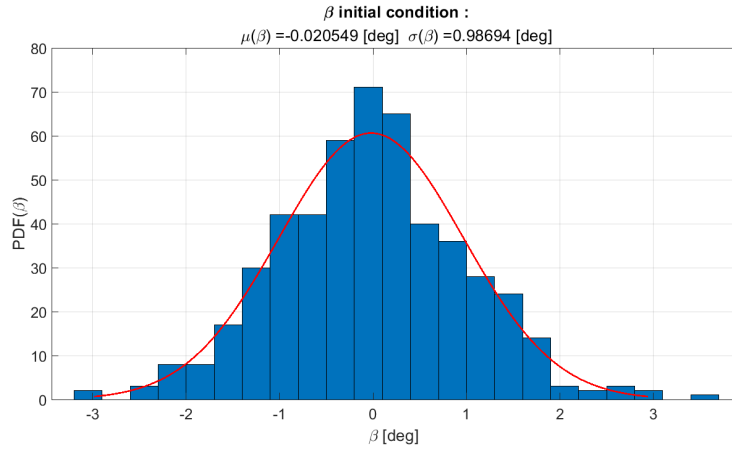


Figure 5.5: Distribution of out-of-plane angle for the initial condition of the different samples employed.

At the end of the simulations, the 500 analysed samples are distributed as shown in the figures 5.6 and 5.7.

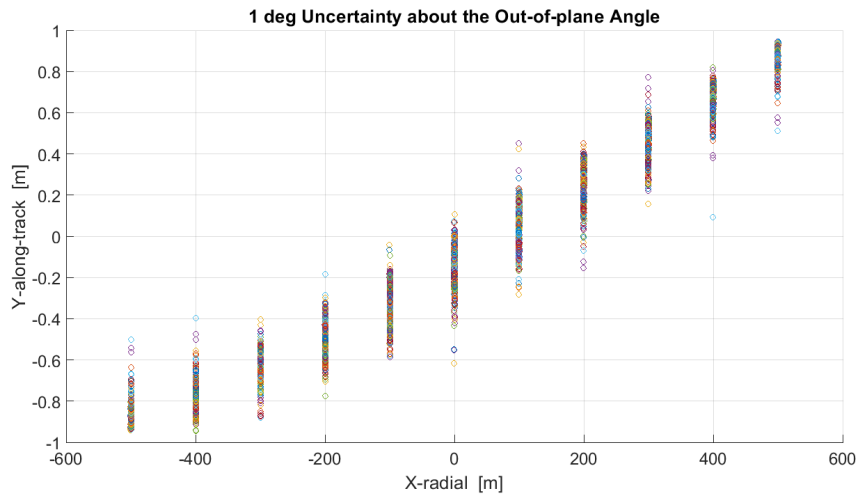


Figure 5.6: Representation of the final condition (after 10 orbits) of the 500 samples differing in the initial condition of the out-of-plane angle (X-Y plane)

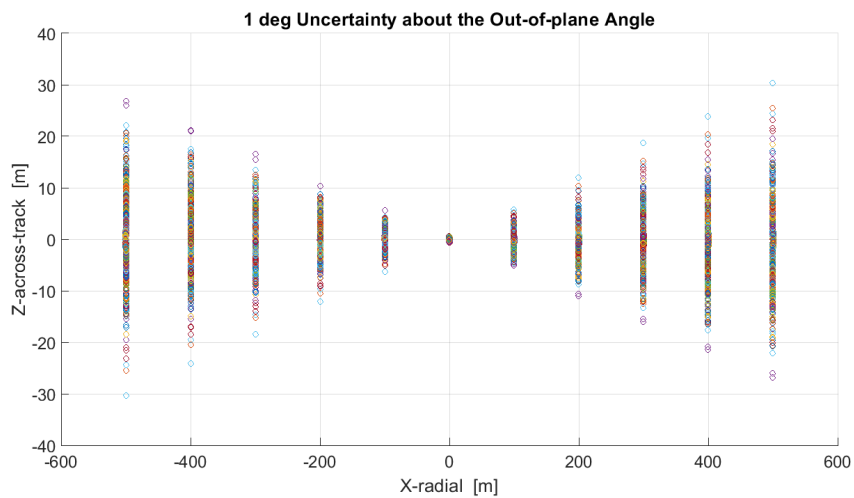


Figure 5.7: Representation of the final condition (after 10 orbits) of the 500 samples differing in the initial condition of the out-of-plane angle (X-Z plane)

The evolution of the standard deviation over time can be seen in figure 5.8.

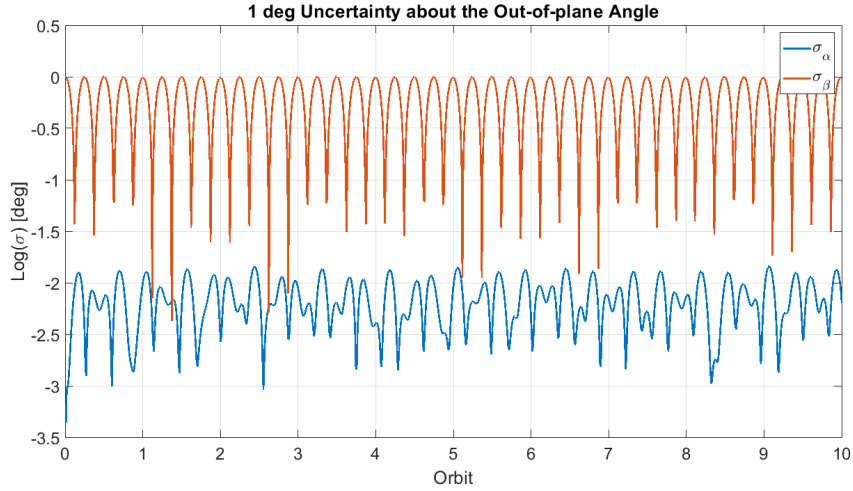


Figure 5.8: Evolution of the standard deviation of the α and β angles due to an uncertainty in the out-of-plane angle.

5.2.3 Analysis of Results for Position Uncertainties

Analysing the results described in the previous two sections, it is possible to observe a certain similarity in the system's response to small uncertainties in the in-plane and out-of-plane angles. From the graphs describing the final state of the system after the 10 orbits (Figures 5.2 and 5.3 for α and 5.6 and 5.7 for β), we can see that the distribution is similar in the two cases. In fact, the hourglass-shaped distribution that we can observe in the Y-X plane in the case of uncertainty in the α angle, can be seen in the Z-X plane in the case of uncertainty in the β angle. This type of distribution, as can easily be guessed, leads to a very large standard deviation for the position of the extremity satellites in terms of Y in the case where the uncertainty is on the in-plane angle, of Z in the case where it is on the out-of-plane angle.

Analysing the evolution of the standard deviations of the two angles in the two cases (figures 5.4 5.8), we can see that they present a certain lobed pattern. This can easily be traced back to the oscillatory motion due to the pendular motion that characterises the system. In fact, it is possible to imagine how the standard deviation is greater as the system oscillates away from the radial position, while it decreases as it approaches the radial position. Since the period of the pendulum motion, as seen, depends only on the orbital period, in all simulations we will have an in-phase oscillation, which will determine the lobes visible in the graphs.

In spite of this behaviour, we can observe that, in both cases, the standard deviation of the parameter on which an uncertainty was imposed remains relatively constant (barring the described oscillations), always showing peaks of the order of 1 [deg]. In

both cases, the other angle always shows similar oscillations but with lower peaks, of the order of 10^{-2} [deg] .

5.3 Satellites' Characteristics Uncertainties

In this section, the system's response to uncertainties relating to the physical characteristics of the bodies forming the EndFire array will be analyzed.

In contrast to the previous section, in which the overall variations of the entire system were considered, in this section an independent variation in each individual component of the system will be considered. Specifically, it will be observed how variations in mass (m_i), surface area (A_i), drag coefficient (CD_i) and reflectivity coefficient (CR_i) affect the evolution of the system over the 10 orbits.

For clarity, the satellites will be numbered from 1 to 11, where 1 indicates the satellite closest to the earth and 11 the satellite furthest away.

In the first part of this section, the results concerning the uncertainty of these parameters will be shown, and then analyzed in the second part.

5.3.1 Uncertainty on Masses (m_i)

With regard to the uncertainty about mass, it was considered that each body belonging to the system has an uncertainty with a standard deviation of 10%. Each body, consequently, will have a slightly different mass in each of the 500 samples from that predicted in the nominal simulation. In the figure, the mass distribution of the samples can be observed in the case of satellite 1, which has a nominal mass of 100.5 [kg]. The same procedure was used for all the other masses in the system.

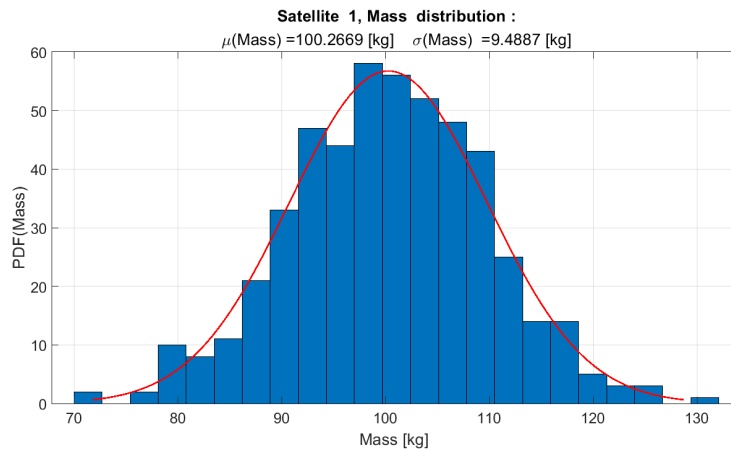


Figure 5.9: Distribution of the masses used for the different samples of satellite 1.

From the different samples, simulations of 10 orbits were run, resulting in the final distribution of samples that can be observed in figures 5.10, 5.11.

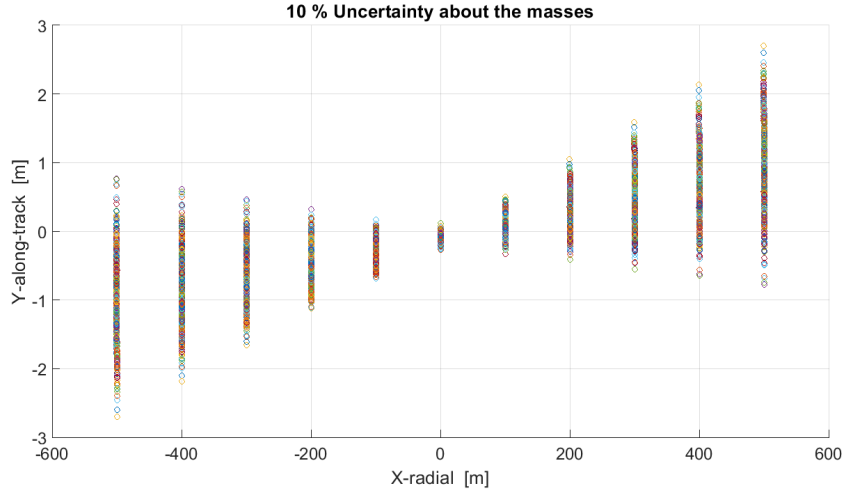


Figure 5.10: Representation of the final condition (after 10 orbits) of the 500 samples differing in the mass of each body (X-Y plane)

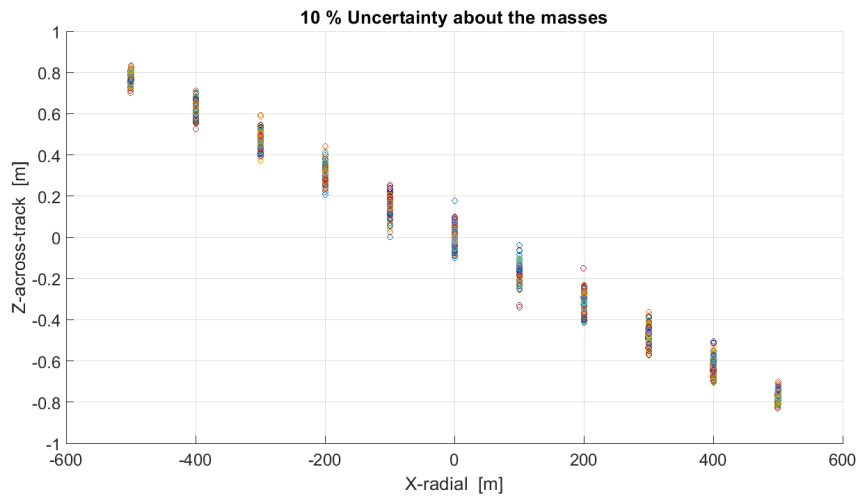


Figure 5.11: Representation of the final condition (after 10 orbits) of the 500 samples differing in the mass of each body (X-Z plane)

The uncertainty propagation in terms of velocity and position was also extrapolated from the simulations. To get an overall view of the system, this was represented for the two bodies at the ends (1 and 11) and the central body (6).

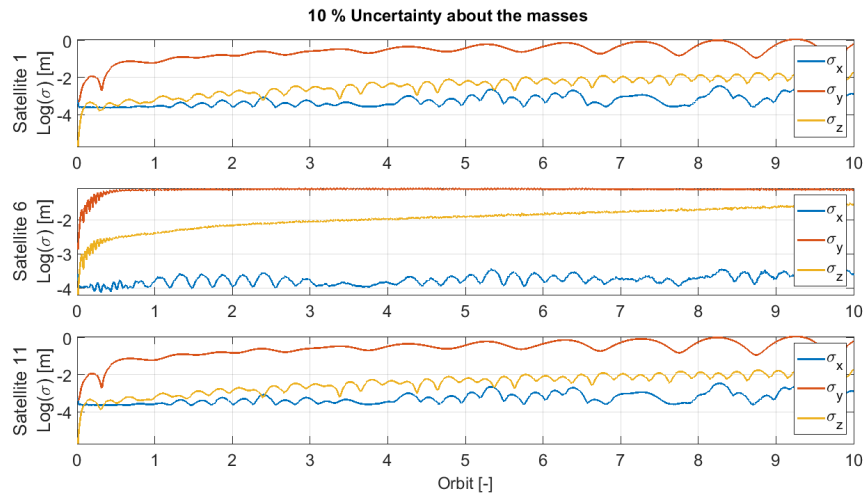


Figure 5.12: Evolution of position standard deviation due to 10% uncertainty in mass for satellites 1, 6 and 11.

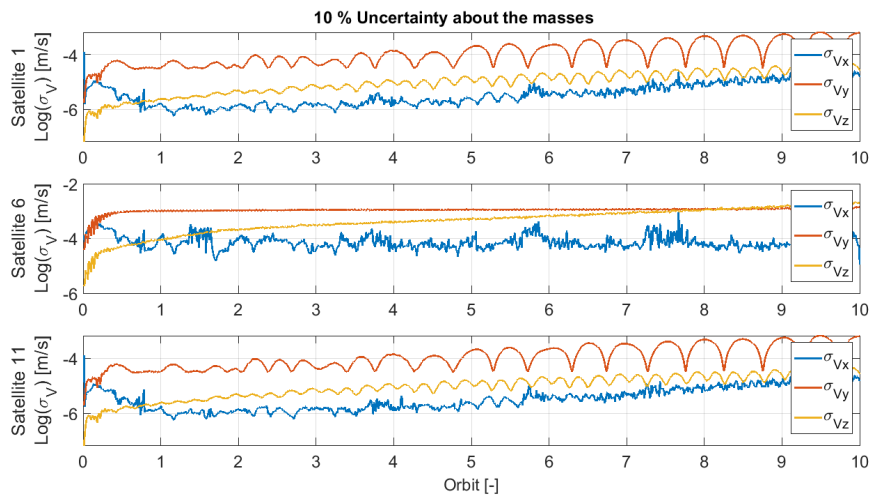


Figure 5.13: Evolution of velocity standard deviation due to 10% uncertainty in mass for satellites 1, 6 and 11.

5.3.2 Uncertainty on Surfaces (A_i)

An uncertainty with a standard variation of 10% from the nominal value was also considered for the surface of the various satellites. Again, all bodies belonging to the system have an uncertainty independent of the other values.

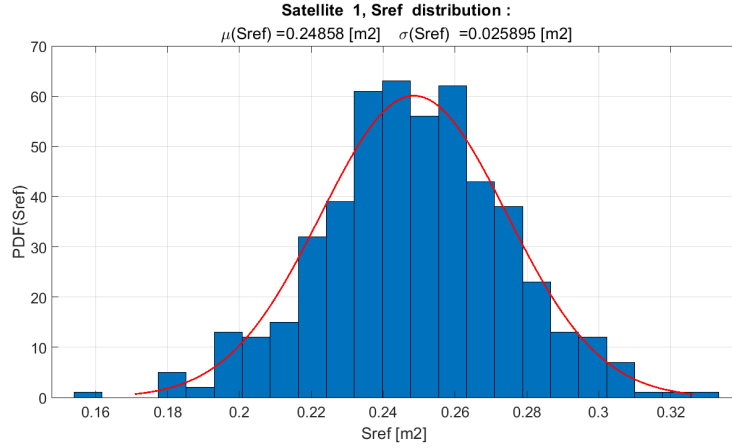


Figure 5.14: *Distribution of the surfaces used for the different samples of satellite 1.*

The final distributions of the samples obtained in this case are represented in the figures 5.15 and 5.16.

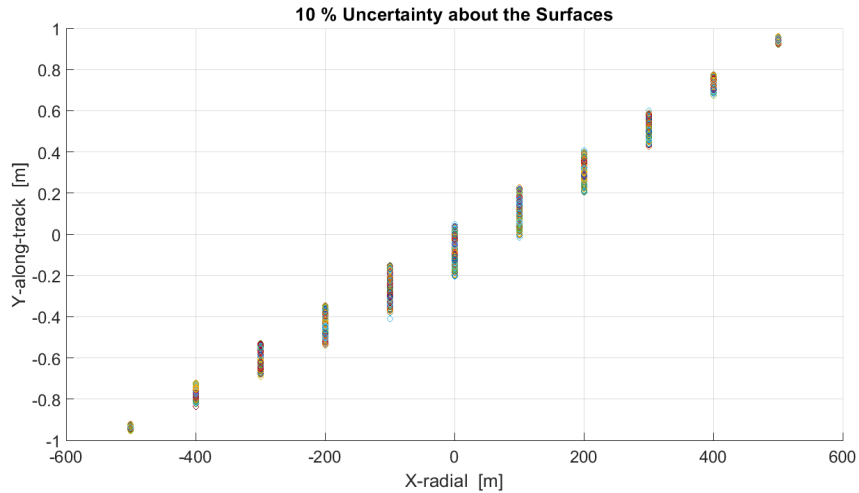


Figure 5.15: *Representation of the final condition (after 10 orbits) of the 500 samples differing in the surfaces of each body (X-Y plane)*

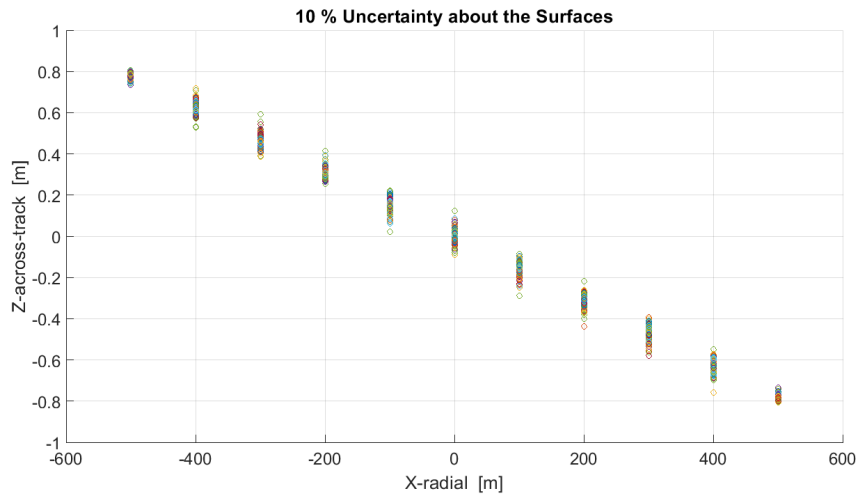


Figure 5.16: Representation of the final (after 10 orbits) condition of the 500 samples differing in the surfaces of each body (X - Z plane)

The propagation of the standard variation of velocity and position for satellites 1, 6 and 11 is shown in the figures 5.17 and 5.18.

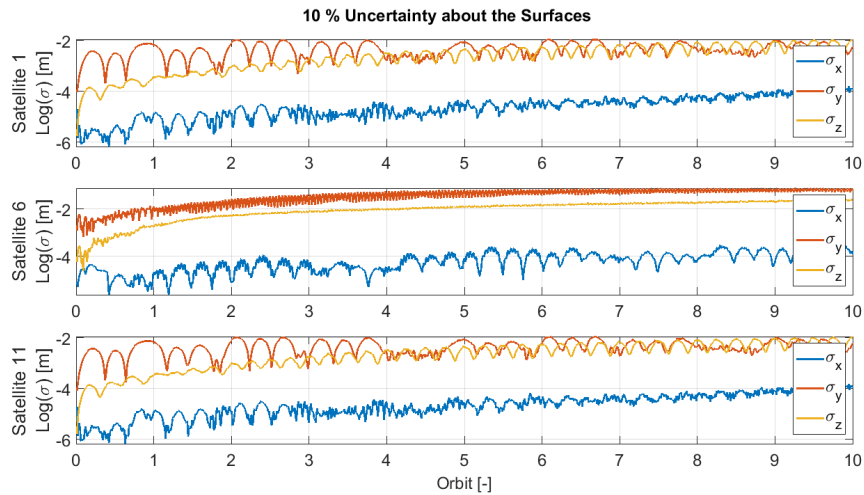


Figure 5.17: Evolution of position standard deviation due to 10% uncertainty in surfaces for satellites 1, 6 and 11.

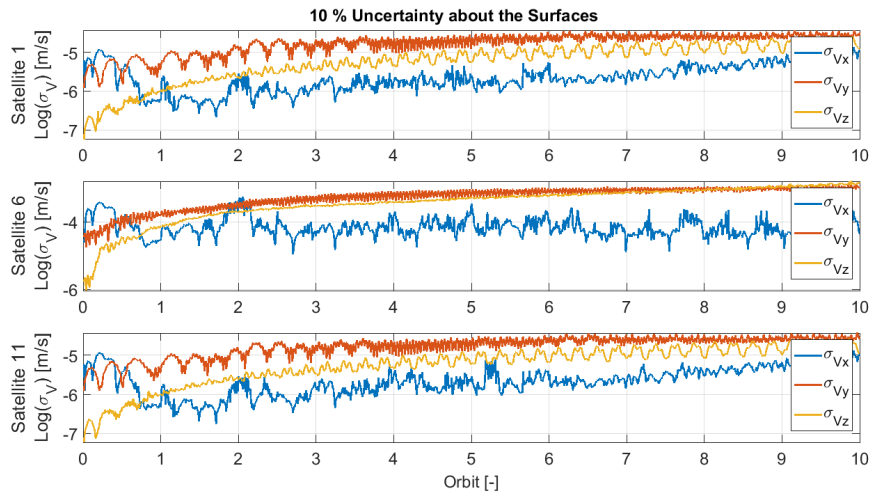


Figure 5.18: Evolution of velocity standard deviation due to 10% uncertainty in surfaces for satellites 1, 6 and 11.

5.3.3 Uncertainty on Drag Coefficients (CD_i)

Similar to the previous cases, an uncertainty with standard variation of 10% from the nominal value was also considered for the drag coefficient of all bodies.

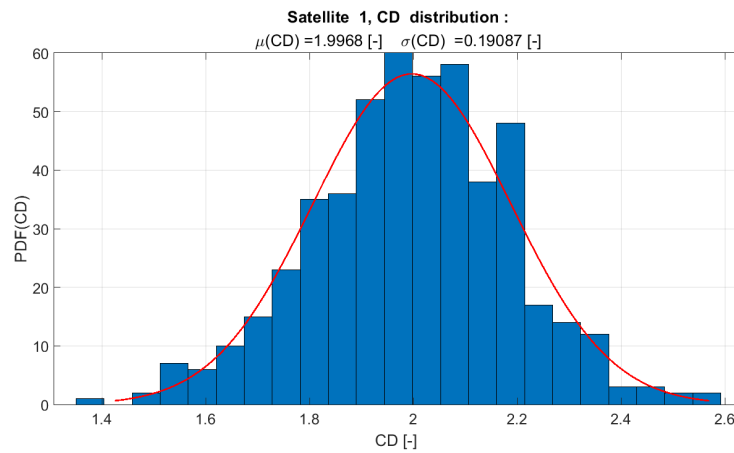


Figure 5.19: Distribution of the drag coefficients used for the different samples of satellite 1.

From this uncertainty, the sample distribution shown in the figures 5.20 and 5.21 was obtained.

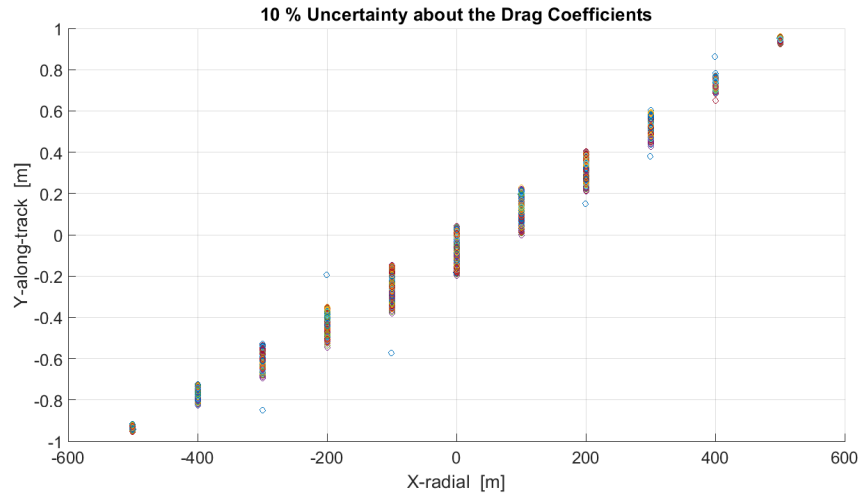


Figure 5.20: Representation of the final condition (after 10 orbits) of the 500 samples differing in the drag coefficients of each body (X-Y plane)

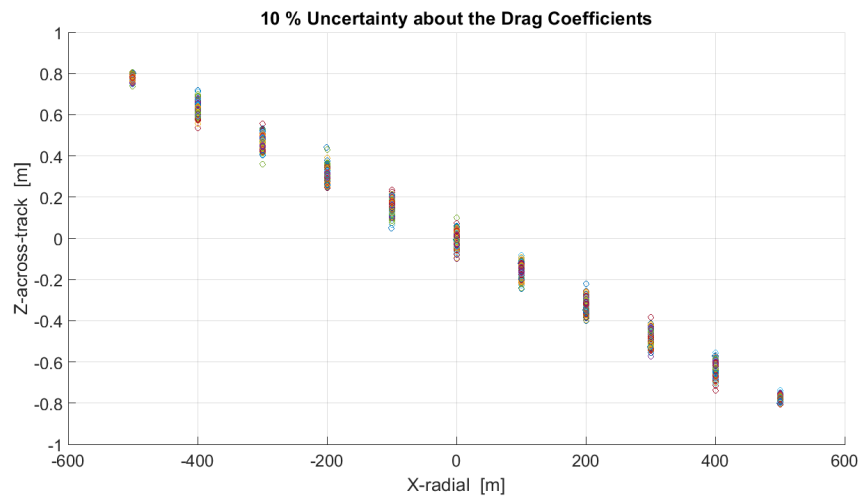


Figure 5.21: Representation of the final (after 10 orbits) condition of the 500 samples differing in the drag coefficients of each body (X-Z plane)

The evolution of position and velocity standard deviations for satellites 1, 6 and 11 are shown in figures 5.22 and 5.23.

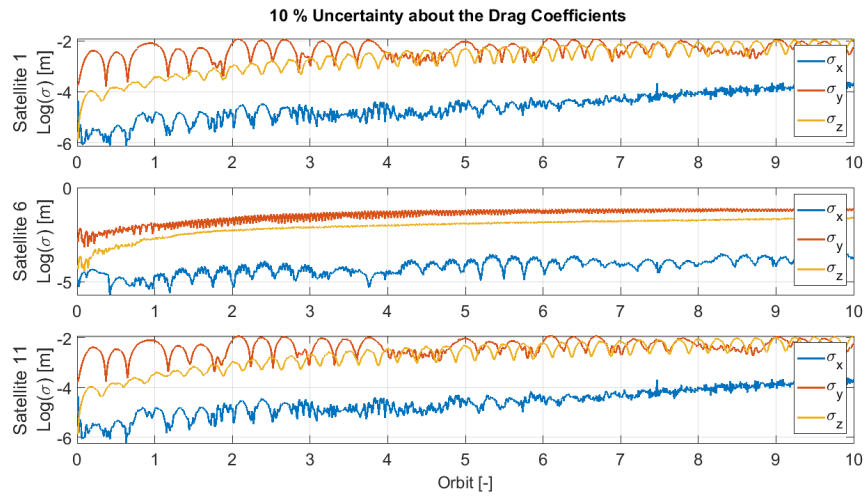


Figure 5.22: Evolution of position standard deviation due to 10% uncertainty in drag coefficients for satellites 1, 6 and 11.

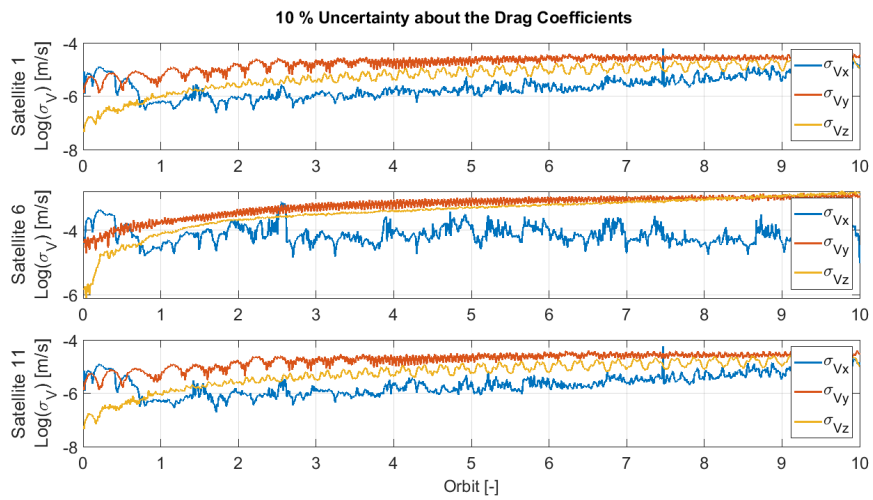


Figure 5.23: Evolution of velocity standard deviation due to 10% uncertainty in drag coefficients for satellites 1, 6 and 11.

5.3.4 Uncertainty on Reflectivity Coefficients (CR_i)

Finally, the last uncertainty that was considered is related to the reflectivity coefficient, which also has a standard deviation of 10% respect to the nominal value.

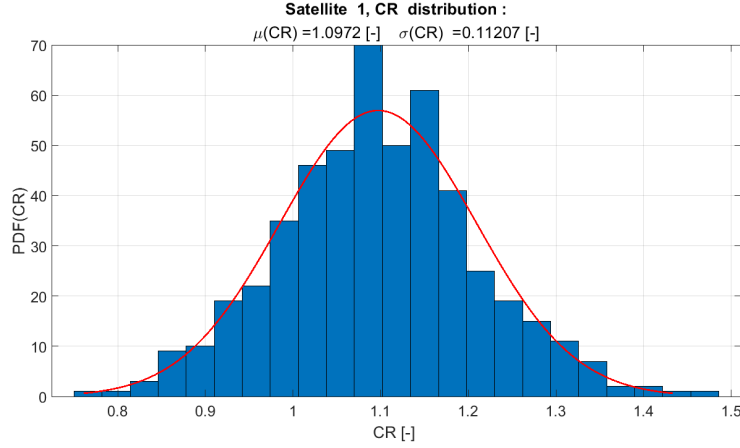


Figure 5.24: Distribution of the reflectivity coefficients used for the different samples of satellite 1.

From this uncertainty, the sample distribution shown in the figures 5.25 and 5.26 was obtained.

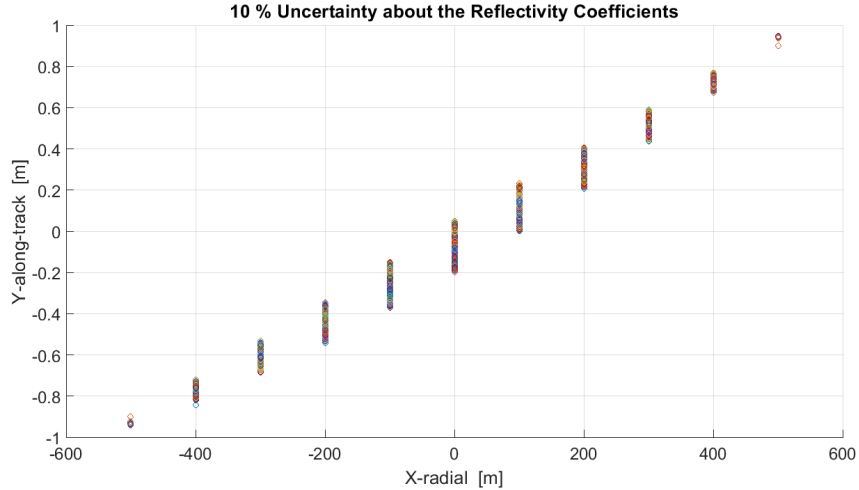


Figure 5.25: Representation of the final condition (after 10 orbits) of the 500 samples differing in the reflectivity coefficients of each body (X-Y plane)

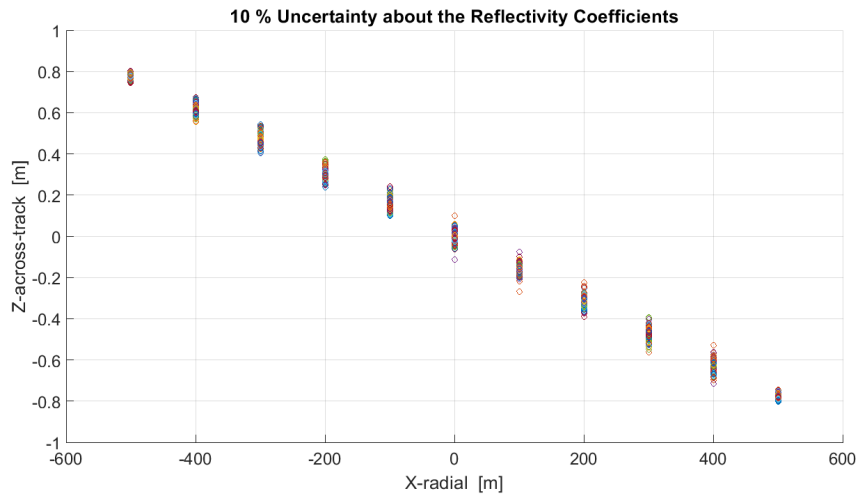


Figure 5.26: Representation of the final (after 10 orbits) condition of the 500 samples differing in the reflectivity coefficients of each body (X-Z plane)

The evolution of position and velocity standard deviations for satellites 1, 6 and 11 are shown in figures 5.27 and 5.28.

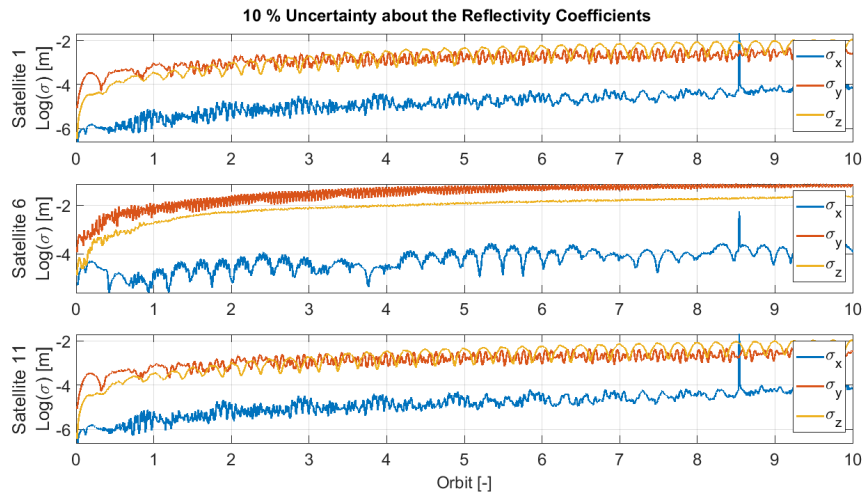


Figure 5.27: Evolution of position standard deviation due to 10% uncertainty in reflectivity coefficients for satellites 1, 6 and 11.

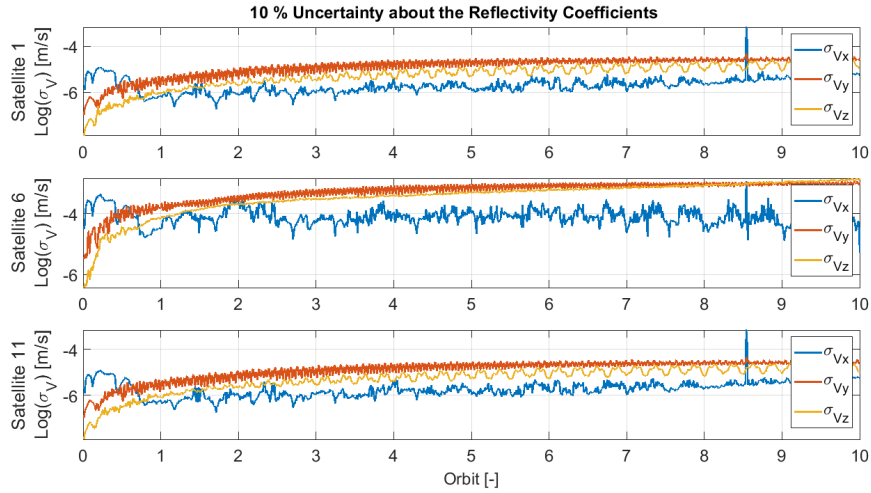


Figure 5.28: Evolution of velocity standard deviation due to 10% uncertainty in reflectivity coefficients for satellites 1, 6 and 11.

5.3.5 Analysis of Results for Satellites' Characteristics Uncertainties

From the data illustrated in the previous section, it is possible to analyze how the uncertainties related to the physical characteristics of the bodies constituting the system have much less pronounced repercussions than the uncertainties of the initial positions, described earlier.

The parameter that creates the most repercussions, as could be imagined, is mass. This is due to the fact that, given the same forces applied on the different satellites, a change in mass results in a change in all the accelerations experienced by that body. The second most important is the surface, which influences both atmospheric and solar pressure effects. Finally, unlike previous ones, the parameters related to drag or reflectivity coefficients affect, respectively, only the accelerations due to atmospheric drag and solar pressure, resulting, consequently, in less perturbation of the system.

From the analysis performed, the convenience of the tethered system is evident. Analyzing the standard deviation in terms of radial position, it can be seen that the stabilizing effects of the gravitational gradient in combination with the tension generated in the tether in the event of displacement result in a very small change in position in this direction, which, even in the worst case, is of the order of magnitude of 10^{-4} [m]. This analysis also reveals another effect caused by tether dynamics. In contrast to the case of uncertain orientation, the central body (satellite 6) in

this case has more freedom of movement than the end bodies. It can be seen that it has higher standard deviations than bodies 1 and 11.

This can be explained by the fact that, in contrast to what happens in the case of uncertainties in the orientation of the system and in the mass, in which the pendular motion of the system is excited by generating large mass displacements at the end, small perturbations along the tether excite the Longitudinal and Transverse modes. Specifically, the first mode creates a greater displacement in the central mass, which results in a greater uncertainty in its position.

Nevertheless, the analysis shows that a tethered system has much smaller uncertainties than a Helix formation.[19] In fact, the standard deviations of the positions calculated for the different cases are limited to values of less than a centimeter, much smaller than the standard deviation of the position of the order of a meter presented by a Helix formation with the same uncertainties.

Furthermore, given the dynamics of the tether, it can be observed that in all cases under analysis the uncertainties remain strongly bound to the modes of the system, which influence its evolution.

Knowing the dynamics of the system, it is possible to predict the modes that will be excited, and, consequently, to be able to guess in which manner and in which directions the greatest uncertainties will occur.

Chapter 6

Feasibility Study of an Across-Track Configuration

In this chapter, the behavior of an EndFire Array placed in an across-track configuration will be analyzed.

This type of configuration is particularly interesting, because, as mentioned in chapter 1, it would be possible to combine the Synthetic Aperture Radar (SAR) technique with Phased Array Beamforming, creating a spatial sampling both in the along-track direction (thanks to the movement of the constellation) and in the across-track direction (thanks to the distribution of these satellite).

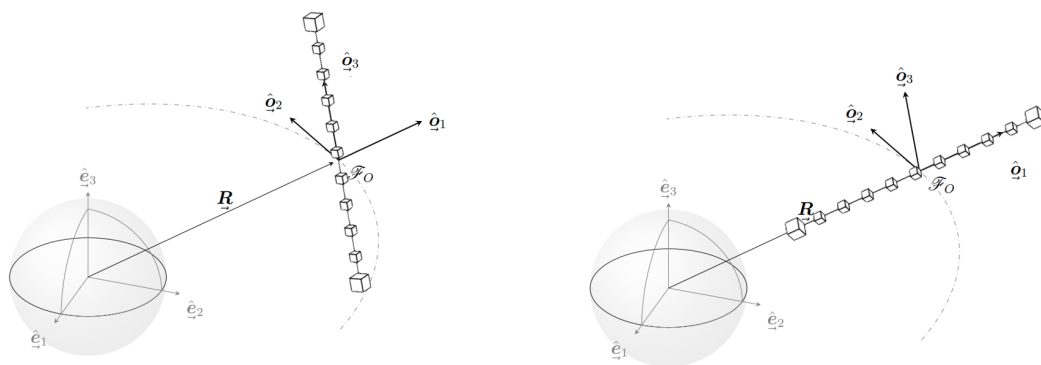


Figure 6.1: Comparison between the radial configuration (on the right) and across-track configuration (on the left).

Nevertheless, it is necessary to consider that this type of configuration does not

benefit from the stabilizing effects due to the gravitational gradient, having all satellites in the horizontal plane and, therefore, at the same altitude.

For this reason, maintaining this configuration leads to the need to introduce more frequent and more expensive control.

In the first part of this chapter the behavior of this type of configuration will be studied by analyzing its free evolution in the long long term. Then a control law will be computed using *Optimal Control*, linearizing the system and considering an estimation of the state of the system obtained with a *Discrete Time Kalman Filter*. Finally, simulations on the controlled system with the calculated control law will be analyzed, discussing the feasibility of a mission of this kind.

6.1 Free propagation of an EndFire Array oriented across-track

For an initial study of this type of configuration, a simplified model was chosen, which considers only the two satellite at the ends, without modeling a discretized distribution of the mass of the tether.

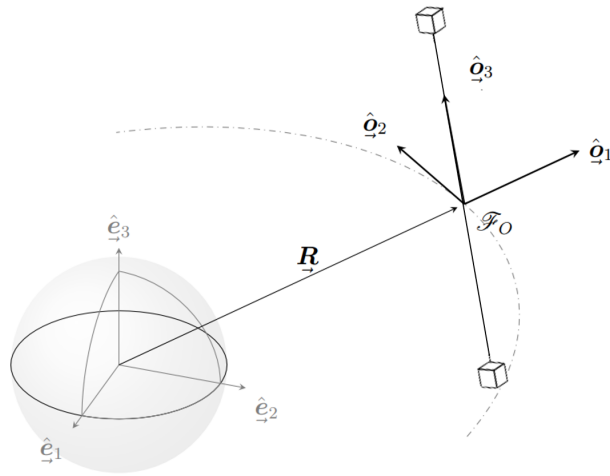


Figure 6.2: Schematization of the simplified system in the across-track configuration.

To carry out this simulation, the same characteristics introduced in the chapter 4 regarding the reference orbit and tether characteristics were used (tables 4.4, 4.3). Regarding the satellites, however, a slight modification was made to their mass, in order to distribute the mass of the tether between the two (table 6.1).

		Satellite
Mass	kg	105
Side length	m	0.5
Inertia matrix	kg m ²	$\begin{bmatrix} 4.1667 & 0 & 0 \\ 0 & 4.1667 & 0 \\ 0 & 0 & 3.3334 \end{bmatrix}$

Table 6.1: *Satellite characteristics for simplified simulation*

In this simulation, the system was placed in the across-track direction and was allowed to evolve freely for a total time of 50 orbits. The `Matlab` function `ode23t` was used for integration, with an absolute tolerance of 10^{-6} .

From these simulations, it was possible to analyze the behavior of the system through the analysis of the evolution of radial (figure 6.3), along-track (figure 6.4) and across-track (figure 6.5) position.

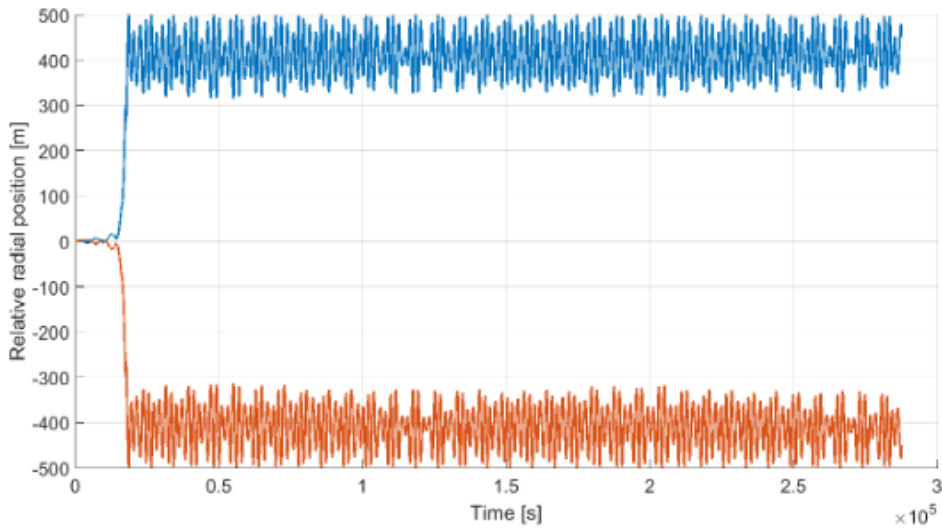


Figure 6.3: *Evolution of the radial position of the 2 masses representing the EndFire Array, initialized in the across-track configuration. The graph is referred to the center of mass of the system.*

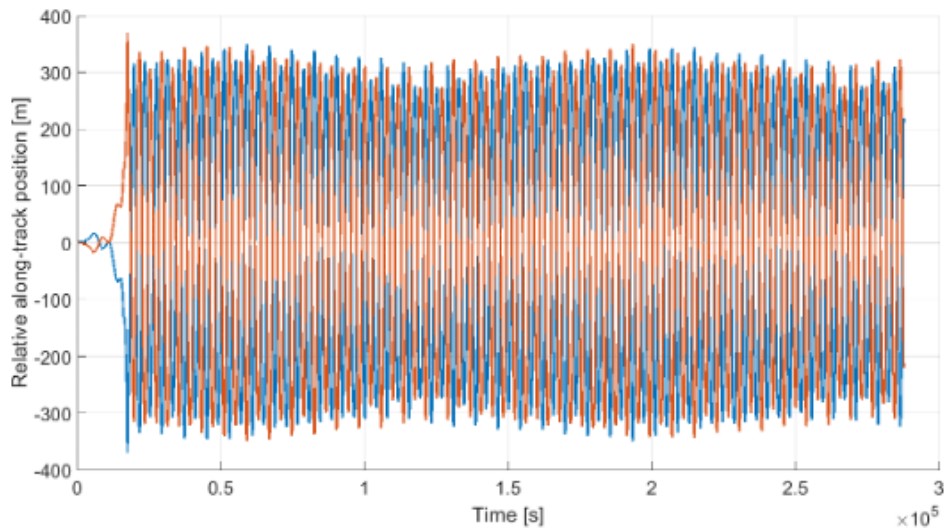


Figure 6.4: Evolution of the along-track position of the 2 masses representing the EndFire Array, initialized in the across-track configuration. The graph is referred to the center of mass of the system.

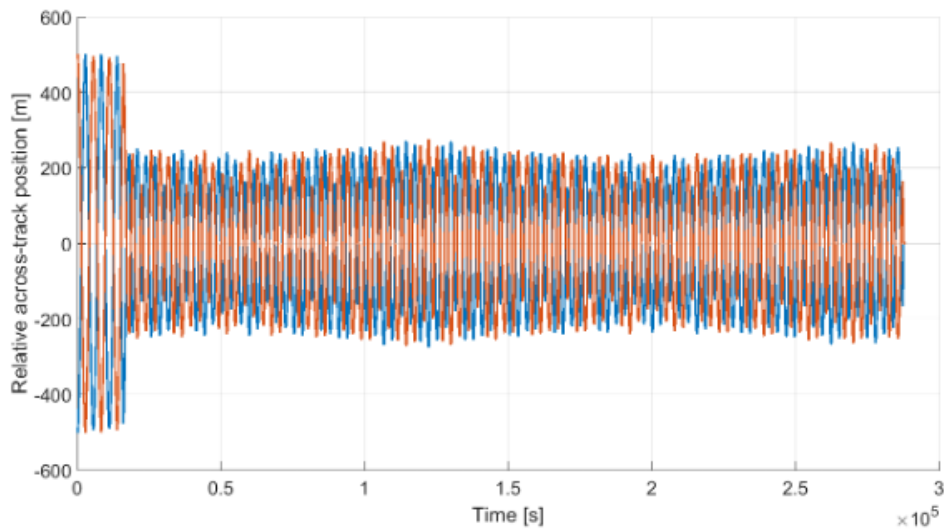


Figure 6.5: Evolution of the across-track position of the 2 masses representing the EndFire Array, initialized in the across-track configuration. The graph is referred to the center of mass of the system.

As we can observe, the system starts from the across-track position, with the two satellites positioned at $z_1 = -500$ m and $z_2 = 500$ m, respectively, while $x_1 = x_2 = 0$ m, $y_1 = y_2 = 0$ m.

From this initial position the system begins to oscillate, in the first few orbits maintaining small displacements in the along-track and radial directions and moving only in the across-track direction.

Thereafter these oscillations also shift in the radial and along-track directions, causing the system to fall back to a quasi-radial position, around which it rotates oscillating in both α (in-plane angle) and β (out-of-plane angle)

This simulation gives us further confirmation of the stability of the EndFire system in the radial configuration, on which it falls despite different initial conditions.

In fact, as might be expected, the across-track configuration is not stable. Consequently, due to external perturbations, the system tends to diverge from this initial position, falling back into the radial configuration which is stabilized by the gravitational gradient.

Therefore, in order to obtain a stable system, it is necessary to introduce a control law that can counter external perturbations so as to ensure the stability of the system even in a naturally unstable configuration.

6.2 Stabilization using Optimal Control

As seen in the previous section, an EndFire Array placed in the across-track configuration is not stable, and it is therefore necessary to apply active control to ensure that the configuration is maintained.

This section will examine the procedure carried out for obtaining a control law capable of maintaining the across-track position.

Therefore, the following points will be analyzed:

- The steps taken to obtain a linearized model of the system;
- The implementation of a *Discrete Time Kalman Filter* (DTFK) for estimating the system state necessary for feedback control;
- The calculation of the *LQR* command law.

Once all the steps taken to obtain a model of the controlled system have been explained, the results of simulations in which this command is applied will be analyzed.

It is necessary to point out that in the present case, contrary to what Quadrelli and Pastori describe regarding orbital corrections of an EndiFire Array in the radial position, it is necessary to maintain a continuous command to preserve the configuration, and not corrective maneuvers that occur periodically.[17][14]

6.2.1 Model linearization

For model linearization we start from the equation of dynamics described in the equation 3.31, approximating with a two-body gravitational acceleration (equation 3.1) and neglecting the third body perturbation.

In addition, accelerations due to solar pressure and atmospheric drag will be considered as unknown external perturbations.

Proceeding in this way results in the equation:

$$m_i \ddot{\boldsymbol{\rho}}_i = GM_{\oplus} m_i \left(\frac{\mathbf{r}_i}{\|\mathbf{r}_i\|^3} - \frac{\mathbf{R}}{\|\mathbf{R}\|^3} \right) + \mathbf{T}_i - \mathbf{T}_{i-1} - m_i \boldsymbol{\Omega} \times \boldsymbol{\Omega} \times \boldsymbol{\rho}_i - 2m_i \boldsymbol{\Omega} \times \dot{\boldsymbol{\rho}}_i + \mathbf{F}_{ext,i} \quad (6.1)$$

By binomial expansion and neglecting higher-order terms, it is possible to linearize the gravitational stiffness term:

$$\frac{\mathbf{r}_i}{\|\mathbf{r}_i\|^3} - \frac{\mathbf{R}}{\|\mathbf{R}\|^3} = \frac{\mathbf{R} + \boldsymbol{\rho}_i}{\|\mathbf{R} + \boldsymbol{\rho}_i\|^3} - \frac{\mathbf{R}}{\|\mathbf{R}\|^3} \quad (6.2)$$

$$(\boldsymbol{\rho}_i \cdot \mathbf{R}) \boldsymbol{\rho}_i = \boldsymbol{\rho}_i \times (\boldsymbol{\rho}_i + \mathbf{R}) + \boldsymbol{\rho}_i^2 \mathbf{R} \quad (6.3)$$

$$(\boldsymbol{\rho}_i \cdot \mathbf{R}) \mathbf{R} = \mathbf{R} \times (\boldsymbol{\rho}_i + \mathbf{R}) + \mathbf{R}^2 \boldsymbol{\rho}_i \quad (6.4)$$

$$\frac{\mathbf{r}_i}{\|\mathbf{r}_i\|^3} - \frac{\mathbf{R}}{\|\mathbf{R}\|^3} \simeq \frac{-2(\|\mathbf{R}\|^2 \mathbf{I} + 3\mathbf{R} \times \mathbf{R} \times)}{\|\mathbf{R}\|^5} \boldsymbol{\rho}_i \quad (6.5)$$

Substituting into the equation 6.1 gives the expression:

$$m_i \mathbf{I}_3 \ddot{\boldsymbol{\rho}}_i = -2m_i \boldsymbol{\Omega} \times \dot{\boldsymbol{\rho}}_i - m_i \left(-GM_{\oplus} \frac{2(\|\mathbf{R}\|^2 \mathbf{I} + 3\mathbf{R} \times \mathbf{R} \times)}{\|\mathbf{R}\|^5} + \boldsymbol{\Omega} \times \boldsymbol{\Omega} \times \right) \boldsymbol{\rho}_i + \mathbf{T}_{tot,i} + \mathbf{F}_{ext,i} \quad (6.6)$$

The simplified model introduced earlier, in which only the masses of the two satellites at the end are considered, can be used to calculate the corrector. As a consequence, it is possible to express the tether tension as:

$$\mathbf{T}_1 = EA \frac{\|\boldsymbol{\rho}_2 - \boldsymbol{\rho}_1\| - L}{L} \boldsymbol{\tau} \quad \mathbf{T}_2 = -\mathbf{T}_1 \quad \boldsymbol{\tau} = \frac{\boldsymbol{\rho}_2 - \boldsymbol{\rho}_1}{\|\boldsymbol{\rho}_2 - \boldsymbol{\rho}_1\|} \quad (6.7)$$

It is possible to reformulate the expression of \mathbf{T}_1 as:

$$\mathbf{T}_1 = EA \frac{\boldsymbol{\rho}_2 - \boldsymbol{\rho}_1}{L} - EA \boldsymbol{\tau} \quad (6.8)$$

Defining the tether stiffness as $\mathbf{K}_t = \frac{EA}{L}\mathbf{I}_3$ and considering that in the initial conditions, around which the linearization is made, the system is positioned across-track and therefore $\boldsymbol{\tau}_0 = [0,0,1]^T$, the expression becomes:

$$\mathbf{T}_1 = \mathbf{K}_t(\boldsymbol{\rho}_2 - \boldsymbol{\rho}_1) - EA\boldsymbol{\tau}_0 \quad (6.9)$$

$$\mathbf{T}_2 = \mathbf{K}_t(\boldsymbol{\rho}_1 - \boldsymbol{\rho}_2) + EA\boldsymbol{\tau}_0 \quad (6.10)$$

Substituting into the equation 6.6 and considering $i=1,2$ gives the two equations :

$$\begin{cases} \mathbf{M}_1\ddot{\boldsymbol{\rho}}_1 + \mathbf{D}_{orb,1}\dot{\boldsymbol{\rho}}_1 + \mathbf{K}_{orb,1}\boldsymbol{\rho}_1 = \mathbf{K}_t(\boldsymbol{\rho}_2 - \boldsymbol{\rho}_1) - EA\boldsymbol{\tau}_0 + \mathbf{F}_{ext,1} \\ \mathbf{M}_2\ddot{\boldsymbol{\rho}}_2 + \mathbf{D}_{orb,2}\dot{\boldsymbol{\rho}}_2 + \mathbf{K}_{orb,2}\boldsymbol{\rho}_2 = \mathbf{K}_t(\boldsymbol{\rho}_1 - \boldsymbol{\rho}_2) + EA\boldsymbol{\tau}_0 + \mathbf{F}_{ext,2} \end{cases} \quad (6.11)$$

Where:

$$\mathbf{M}_i = m_i\mathbf{I}_3 \quad \mathbf{D}_{orb,i} = 2m_i\boldsymbol{\Omega}^\times$$

$$\mathbf{K}_{orb,i} = m_i \left(-GM_\oplus \frac{2(\|\mathbf{R}\|^2\mathbf{I}_3 + 3\mathbf{R}^\times\mathbf{R}^\times)}{\|\mathbf{R}\|^5} + \boldsymbol{\Omega}^\times\boldsymbol{\Omega}^\times \right)$$

By defining the vector $\boldsymbol{\rho} = [\boldsymbol{\rho}_1, \boldsymbol{\rho}_2]^T$, we obtain the equation:

$$\mathbf{M}\ddot{\boldsymbol{\rho}} + \mathbf{D}\dot{\boldsymbol{\rho}} + \mathbf{K}\boldsymbol{\rho} = \mathbf{F}_{tether} + \mathbf{F}_{ext} \quad (6.12)$$

Where:

$$\mathbf{M} = \begin{bmatrix} \mathbf{M}_1 & \mathbf{0}_3 \\ \mathbf{0}_3 & \mathbf{M}_2 \end{bmatrix}$$

$$\mathbf{D} = \begin{bmatrix} \mathbf{D}_{orb,1} & \mathbf{0}_3 \\ \mathbf{0}_3 & \mathbf{D}_{orb,2} \end{bmatrix}$$

$$\mathbf{K} = \begin{bmatrix} \mathbf{K}_{orb,1} + \mathbf{K}_t & -\mathbf{K}_t \\ -\mathbf{K}_t & \mathbf{K}_{orb,2} + \mathbf{K}_t \end{bmatrix}$$

$$\mathbf{F}_{tether} = EA \begin{bmatrix} 0 \\ 0 \\ -1 \\ 0 \\ 0 \\ 1 \end{bmatrix}$$

$$\mathbf{F}_{ext} = \begin{bmatrix} \mathbf{F}_{ext,1} \\ \mathbf{F}_{ext,2} \end{bmatrix}$$

At this point it is possible to linearize around the equilibrium point $\boldsymbol{\rho}_{eq}$ and making a change of variables so that the constant forces disappear:

$$\boldsymbol{\rho}_{eq} = -\mathbf{K}^{-1}\mathbf{F}_{tether} \quad \Delta\boldsymbol{\rho} = \boldsymbol{\rho} - \boldsymbol{\rho}_{eq} \quad (6.13)$$

The linearized equation is obtained:

$$\mathbf{M}\Delta\ddot{\boldsymbol{\rho}} + \mathbf{D}\Delta\dot{\boldsymbol{\rho}} + \mathbf{K}\Delta\boldsymbol{\rho} = \mathbf{F}_{ext} \quad (6.14)$$

By introducing the state vector $\mathbf{X} = [\Delta\boldsymbol{\rho}, \Delta\dot{\boldsymbol{\rho}}]^T$ and decomposing the external forces between perturbations forces (\mathbf{F}_{pert}) and control forces (\mathbf{F}_{ctr}), we can then derive the matrices \mathbf{A} , \mathbf{B} and \mathbf{L} . Through these we can derive a linearized state representation of our system, by which we will synthesize our command law:

$$\dot{\mathbf{X}} = \mathbf{A}\mathbf{X} + \mathbf{B}\mathbf{F}_{ctr} + \mathbf{L}\mathbf{F}_{pert} \quad (6.15)$$

Where:

$$\mathbf{A} = \begin{bmatrix} \mathbf{0}_6 & \mathbf{I}_6 \\ -\mathbf{M}^{-1}\mathbf{K} & -\mathbf{M}^{-1}\mathbf{D} \end{bmatrix} \quad \mathbf{B} = \mathbf{L} = \begin{bmatrix} \mathbf{0}_6 \\ \mathbf{I}_6 \end{bmatrix}$$

6.2.2 State Estimation

In order to properly implement a controller to ensure system stabilization, it is necessary to know the state of the system at each instant. In the present case, since it is implemented on a simulator, we know exactly the state of the system at each instant in time. Nevertheless, this does not reflect the real case, where, in order to know the state of the system, it is necessary to make measurements that can provide the required information.

For the problem under consideration, let us consider the same architecture presented by Quadrelli [14] and taken up by Pastori [17]. In this architecture, called the *De-centralized measurement strategy*, there is a leading satellite which calculates the command law from the measurements made by all the satellites in the system (figure 6.6). In fact, each satellite measures the distance to the next satellite, sending the information to the leader. This satellite, with the information gathered, generates the command law to control the system.

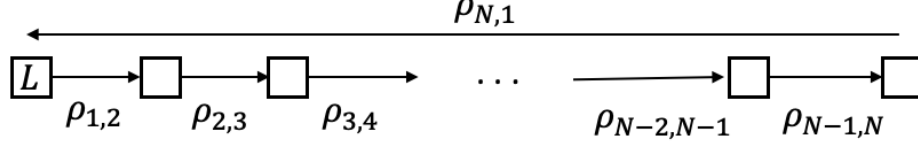


Figure 6.6: Schematization of a De-Centralized Measurement Architecture for a system of N bodies

The measurements under consideration will be obtained through the use of accelerometers and optical sensors, which will be subject to some measurement noise. As a consequence, it becomes apparent that it is necessary to introduce an estimation of the state of the system. To do this we implement a *Discrete Time Kalman Filter* (DTFK).

To define the filter algorithm, it is possible to start from a simplified model of relative dynamics:

$$\ddot{\boldsymbol{\rho}}_i = \mathbf{a}_i - \mathbf{a}_{ORF} + \mathbf{u}_i \quad (6.16)$$

Considering a state \mathbf{X} containing the position and velocity of each satellite, the state matrices \mathbf{A} , \mathbf{B} and \mathbf{L} are obtained:

$$\dot{\mathbf{X}} = \mathbf{A}\mathbf{X} + \mathbf{B}\mathbf{u} + \mathbf{L}\Delta\mathbf{a} \quad (6.17)$$

Where:

$$\mathbf{X} = \begin{bmatrix} \boldsymbol{\rho}_1 \\ \dots \\ \boldsymbol{\rho}_N \\ \dot{\boldsymbol{\rho}}_1 \\ \dots \\ \dot{\boldsymbol{\rho}}_N \end{bmatrix} \quad \mathbf{A} = \begin{bmatrix} \mathbf{0}_{3N} & \mathbf{I}_{3N} \\ \mathbf{0}_{3N} & \mathbf{0}_{3N} \end{bmatrix} \quad \mathbf{B} = \mathbf{L} = \begin{bmatrix} \mathbf{0}_{3N} \\ \mathbf{I}_{3N} \end{bmatrix}$$

Regarding the observations on the system, it is possible to consider the equation:

$$\mathbf{Y} = \mathbf{C}\mathbf{X} + \mathbf{n}_X \quad (6.18)$$

This will consist of $3N$ components, obtained from the observation made by each individual satellite in the constellation. As mentioned earlier, in the de-centralized architecture, each satellite measures the relative position between itself and the

next satellite. The matrix \mathbf{C} , consequently, will have the form:

$$\mathbf{C} = \begin{bmatrix} \begin{bmatrix} \mathbf{I}_3 & -\mathbf{I}_3 & \mathbf{0}_3 & \mathbf{0}_3 & \dots & \mathbf{0}_3 \\ \mathbf{0}_3 & \mathbf{I}_3 & \mathbf{I}_3 & \mathbf{0}_3 & \dots & \mathbf{0}_3 \\ \mathbf{0}_3 & \mathbf{0}_3 & \mathbf{I}_3 & -\mathbf{I}_3 & \dots & \mathbf{0}_3 \\ \dots & \dots & \dots & \dots & \dots & \dots \\ \mathbf{0}_3 & \mathbf{0}_3 & \dots & \dots & \mathbf{I}_3 & -\mathbf{I}_3 \\ -\mathbf{I}_3 & \mathbf{0}_3 & \dots & \dots & \mathbf{0}_3 & \mathbf{I}_3 \end{bmatrix} & \mathbf{0}_{3N} \end{bmatrix} \quad (6.19)$$

It is necessary to emphasize that, considering this \mathbf{C} matrix, it is assuming that each satellite is always in line of sight with the next.

The \mathbf{n}_X term, on the other hand, represents the measurement error, modeled as zero-mean random Gaussian noise.

With this model of the system, it is then possible to implement the discrete-time Kalman filter algorithm, which will provide the estimated state of the system a time $t_i = t_0 + i\Delta t$ denoted as $\hat{\mathbf{X}}_i$.

$$\begin{aligned} \hat{\mathbf{X}}_i^- &= \Phi \hat{\mathbf{X}}_{i-1}^+ + \Gamma \mathbf{u}_{i-1} \\ \mathbf{P}_i^- &= \Phi \mathbf{P}_{i-1}^+ \Phi^T + \mathbf{Q} \\ \mathbf{K} &= \mathbf{P}_i^- \mathbf{C}^T (\mathbf{C} \mathbf{P}_i^- \mathbf{C}^T + \mathbf{R}_d)^{-1} \\ \hat{\mathbf{X}}_i^+ &= \hat{\mathbf{X}}_i^- + \mathbf{K} (\mathbf{Y} - \mathbf{C} \hat{\mathbf{X}}_i^-) \\ \mathbf{P}_i^+ &= (\mathbf{I}_{6N} - \mathbf{K} \mathbf{C}) \mathbf{P}_i^- (\mathbf{I}_{6N} - \mathbf{K} \mathbf{C})^T + \mathbf{K} \mathbf{R}_d \mathbf{K}^T \end{aligned} \quad (6.20)$$

Where:

$$\Phi = e^{\mathbf{A}\Delta t}$$

$$\Gamma = \mathbf{A}^{-1} (e^{\mathbf{A}\Delta t} - \mathbf{I}_{6N}) \mathbf{B} \simeq (\mathbf{I}_{6N} + 1/2\Delta t \mathbf{A}) \mathbf{B} \Delta t = \Lambda$$

$$\mathbf{Q} = q_{acc} \Delta t \Lambda \mathbf{I}_{3N} \Lambda^T$$

$$\mathbf{R}_d = \frac{q_{rf}}{\Delta t} \mathbf{I}_{3N}$$

Denoting q_{acc} and q_{rf} as the covariance of the measurement errors of the accelerometer and the optical sensor, respectively.

6.2.3 Definition of an LQR controller

Using the state estimate computed through the discrete Kalman filter, a feedback loop can be determined by computing a matrix of constant gains through optimal control.

To do this, the matrices \mathbf{A} and \mathbf{B} determined during linearization of the system (equation 6.15) will be used to solve the Riccati equation:

$$-\mathbf{Q} - \mathbf{A}^T \mathbf{P}_\infty - \mathbf{P}_\infty \mathbf{A} + \mathbf{P}_\infty \mathbf{B} \mathbf{R}^{-1} \mathbf{B}^T \mathbf{P}_\infty \quad (6.21)$$

Where \mathbf{Q} and \mathbf{R} represent the state weight matrix and control weight matrix, respectively, defined as:

$$\mathbf{Q} = q_w \begin{bmatrix} \frac{1}{10} \mathbf{I}_6 & \mathbf{0}_6 \\ \mathbf{0}_6 & \frac{1}{10^{-3}} \mathbf{I}_6 \end{bmatrix} \quad (6.22)$$

$$\mathbf{R} = r_w \begin{bmatrix} \frac{1}{u_{max}} \mathbf{I}_6 & \mathbf{0}_6 \\ \mathbf{0}_6 & \frac{1}{u_{max}} \mathbf{I}_6 \end{bmatrix} \quad (6.23)$$

Denoting q_w and r_w as constant weights while u_{max} as the maximum value of the command.

By solving the equation, it is possible to derive the value of the return gains matrix:

$$\mathbf{K}_{LQR} = \mathbf{R}^{-1} \mathbf{B}^T \mathbf{P}_\infty \quad (6.24)$$

Through this matrix, considering the equilibrium state defined by the equation 6.13, and the state estimation obtained from the Discrete Time Kalman Filter, described by the algorithm 6.20, the expression of the command law is obtained:

$$\mathbf{F}_{ctr} = \mathbf{K}_{LQR} (\hat{\mathbf{X}} - \mathbf{X}_{eq}) \quad (6.25)$$

6.2.4 Results of controlled simulation

The discrete-time Kalman filter model and the LQR control law were then introduced into the simulation. The following considerations were made for these simulations:

- The simulation parameters are similar to those described in section 6.1, to which the control and Discrete Time Kalman Filter were implemented;
- Each satellite is able to always relay the next one, considering it always in line of sight with the instrumentation;
- Measurements obtained from the accelerometer and optical sensor are subject to zero mean Gaussian noise with covariance of $q_{acc} = 10^{-6}$ [22] and $q_{rf} = 10^{-7}$ [23];

- Control is active from the beginning of the simulation and keeps the system in the equilibrium condition with respect to the Orbital Reference Frame (ORF);
- The weights $q_w = 10$ and $r_w = 1$ were used for synthesis of the LQR controller, and the maximum command was limited to $u_{max} = 1 N$;
- Control is omnidirectional and performed by cold gas thrusters with specific impulse of $I_{sp} = 70 s$.

With these assumptions, the behavior of the controlled system was simulated for a total of 50 orbits. The method ode23t with an absolute tolerance of 10^{-6} was used for integration.

As can be seen from the results of the simulation shown in figures 6.7,6.8 6.9, the implemented control law succeeds in maintaining the across-track configuration during the 50 simulated orbits.

From the figures 6.7 6.8, it can be seen that the small oscillations of the satellites in the along-track and radial direction are of the order of magnitude of a tenth of millimeter, while the across-track configuration is perfectly maintained, holding the positions of the two satellites constant at $z_1 = 500 m$, $z_2 = -500 m$ respectively.

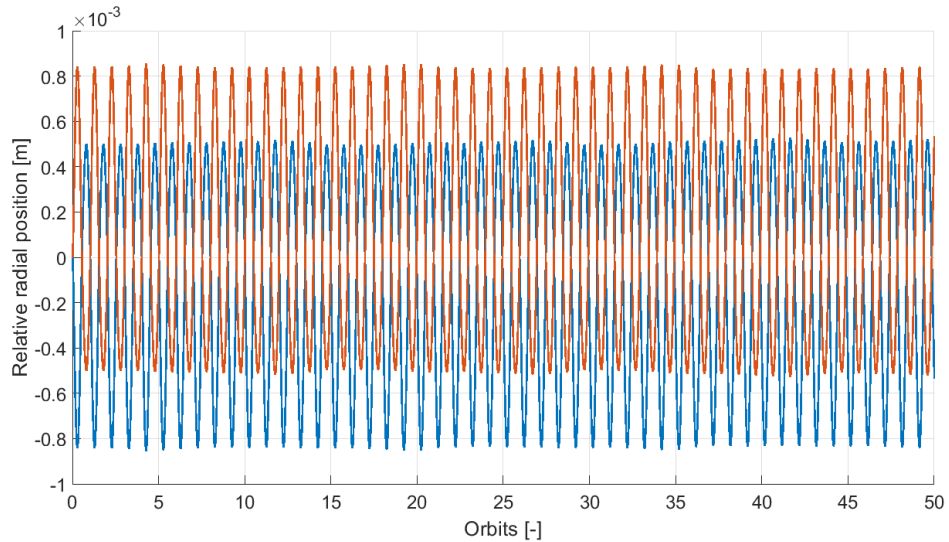


Figure 6.7: Evolution of the radial position of the 2 masses representing the EndFire Array, controlled in order to maintain the across-track configuration.

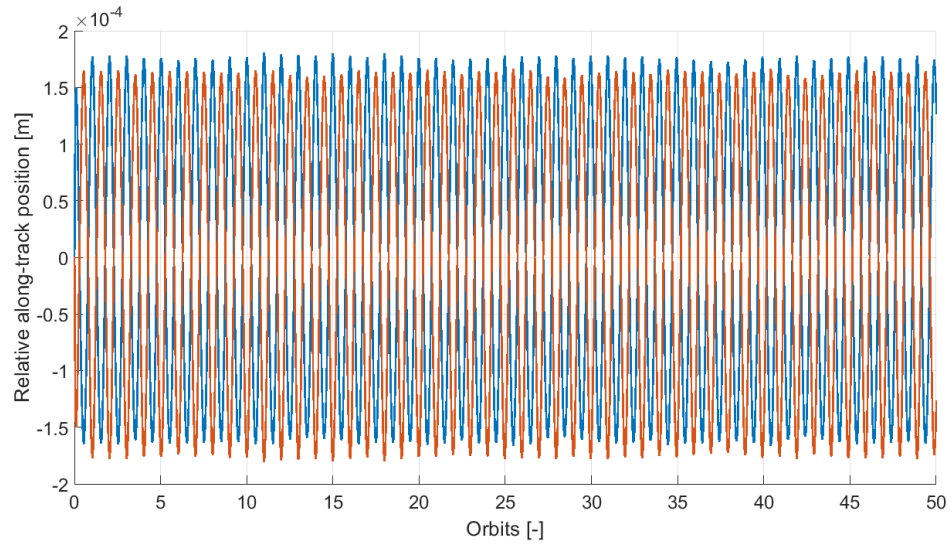


Figure 6.8: Evolution of the along-track position of the 2 masses representing the EndFire Array, controlled in order to maintain the across-track configuration.

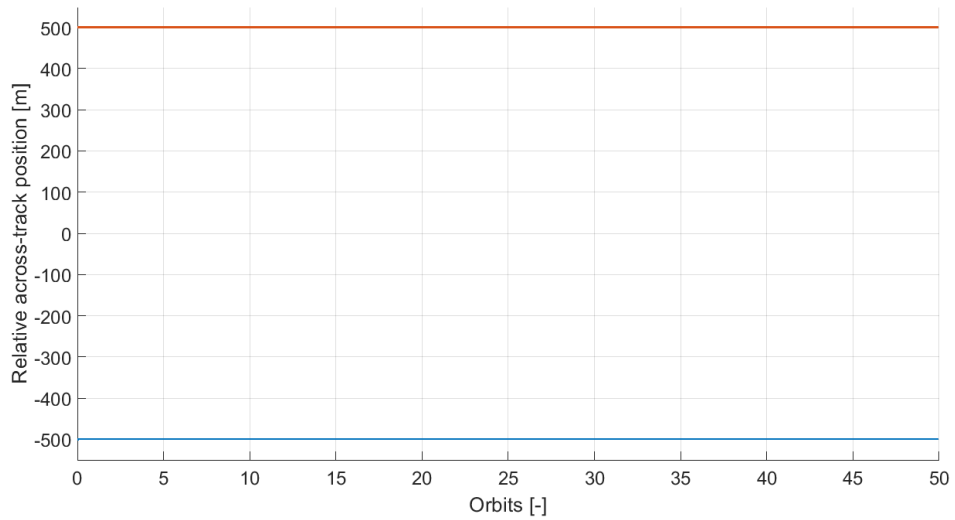


Figure 6.9: Evolution of the across-track position of the 2 masses representing the EndFire Array, controlled in order to maintain the across-track configuration.

Observing the control forces generated by LQR controller for maintaining the configuration, illustrated in the figures 6.10 6.11 6.12, it can be observed that, during all 50 simulated orbits, these all maintain a level of lower than 0.1 N.

The pattern that these forces follow during the orbits appears to be particularly periodic. Moreover, the forces in the along-track and radial directions, turn out to be similar between the two satellites while the across-track forces are opposite. These characteristics will be analyzed and exploited specifically in the next chapter. Although the control forces are moderate, maintaining the configuration using chemical propulsion is particularly expensive.

By calculating the flow rate needed to generate the required forces and integrating it over time, it is possible to obtain the mass of propellant needed to maintain the configuration:

$$\dot{m} = \frac{F}{I_{sp}g_0} \quad m_p = \int_0^T \dot{m} dt \quad (6.26)$$

By performing the calculation for both satellites, it can be obtained:

	m_p (1 Orbit)	m_p (10 Orbit)	m_p (50 Orbit)
Satellite 1	0.645 kg	6.453 kg	32.264 kg
Satellite 2	0.671 kg	6.709 kg	33.544 kg

Table 6.2: *Propellant consumption for the maintenance of the across-track configuration for 1, 10 and 50 orbits*

Taking into account that the mass of the satellites under consideration is 105 kilograms, it is immediate to see how this type of correction turns out to be too expensive and not advantageous.

In spite of this, it is necessary to consider that, with the controller used, not only is the system maintained in the across-track configuration, but this is also maintained in an equilibrium position with respect to the orbiting reference system. Consequently, the costs of maintaining in position include both the cost of maintaining it in configuration and the costs of orbital corrections necessary to counteract losses due to external perturbations.

In the next chapter a decomposition of the applied control forces will be made, filtering those really needed for maintaining the across-track configuration from those needed for orbital corrections, so that possible alternative methods for stabilizing the configuration can be evaluated.

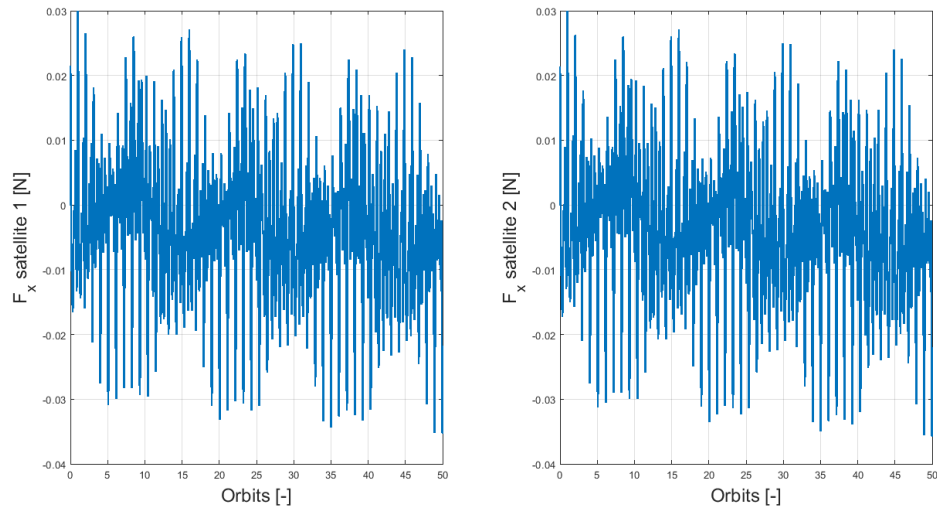


Figure 6.10: Control forces in the radial direction acting on the two satellites generated by the command law in order to maintain the system in the across-track configuration.

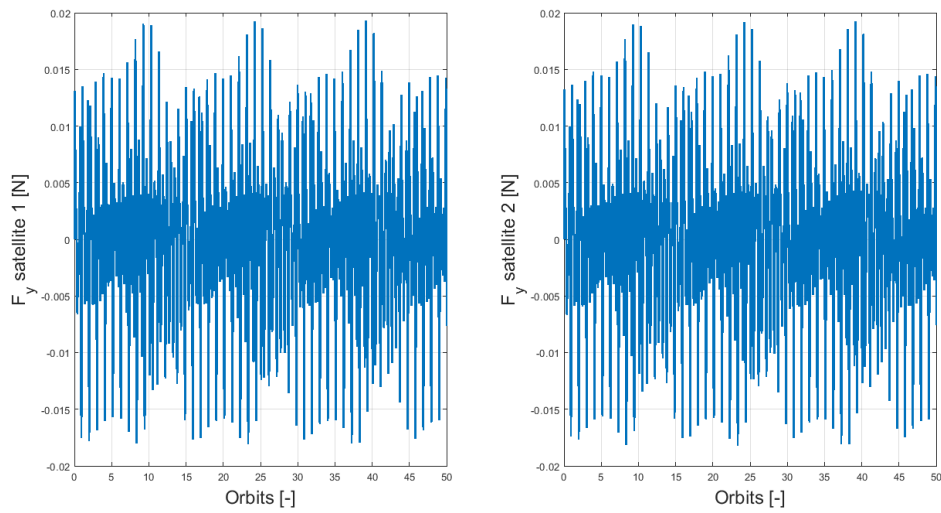


Figure 6.11: Control forces in the along-track direction acting on the two satellites generated by the command law in order to maintain the system in the across-track configuration.

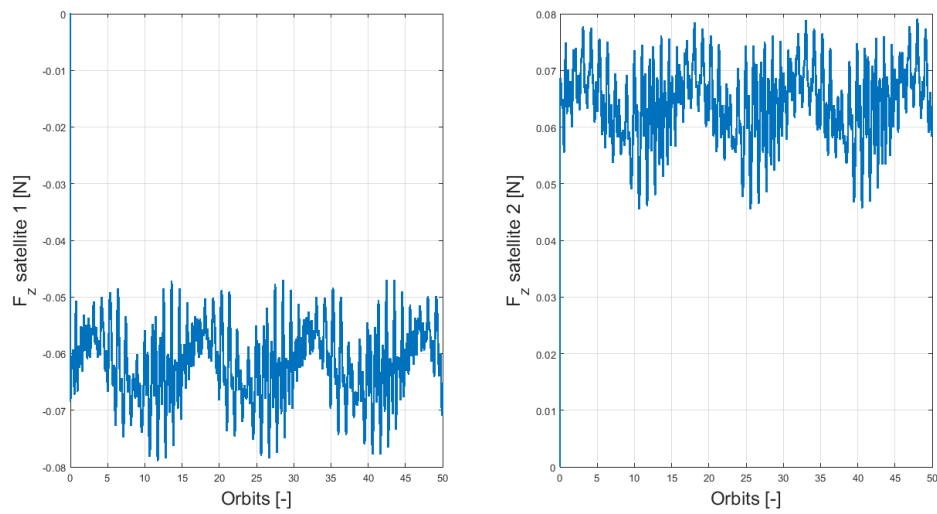


Figure 6.12: Control forces in the across-track direction acting on the two satellites generated by the command law in order to maintain the system in the across-track configuration.

Chapter 7

Aerodynamic Stabilization of the Across-Track Configuration

In the previous chapter, it was observed how it is possible to keep an EndFire array stable in across-track configuration and centered with respect to the orbital reference frame using forces of the order of magnitude of 0.06 [N].

Nevertheless, since it is necessary to maintain a constant control throughout the life cycle, it has been shown that using thrusters for the generation of this kind of control force is very expensive, and, consequently, not very convenient.

In this chapter we will analyze the control forces necessary for the control of the configuration, decomposing those really needed to maintain the across-track configuration from those needed to keep the system centered with respect to the Orbital Reference Frame.

Once this is done, the possibility of using aerodynamic phenomena to help generate the necessary forces will be analyzed, so as to limit the use of thrusters.

7.1 Decomposition of Control Forces

From the calculation made in the last chapter, the different control forces needed to maintain the configuration were obtained. From an initial analysis of the graphs showing the trend of these forces over time, it can be immediately observed that these are almost identical for the two satellites with regard to the radial and along-track components, while they are symmetrical for the across-track component.

Focusing on the relative dynamics, it is easy to imagine how these forces can be decomposed into two components:

- **Average Forces**

Calculating the average force between the two satellites isolates the component of control forces that generates a rigid translation of the system, with no relative displacement between the two bodies.

From the forces calculated in the controlled simulation described in the last chapter, the average forces were calculated as:

$$F_{xm} = \frac{1}{2}(F_{x1} + F_{x2}) \quad F_{ym} = \frac{1}{2}(F_{y1} + F_{y2}) \quad F_{zm} = \frac{1}{2}(F_{z1} + F_{z2}) \quad (7.1)$$

The evolution of these forces over time can be seen in figure 7.1.

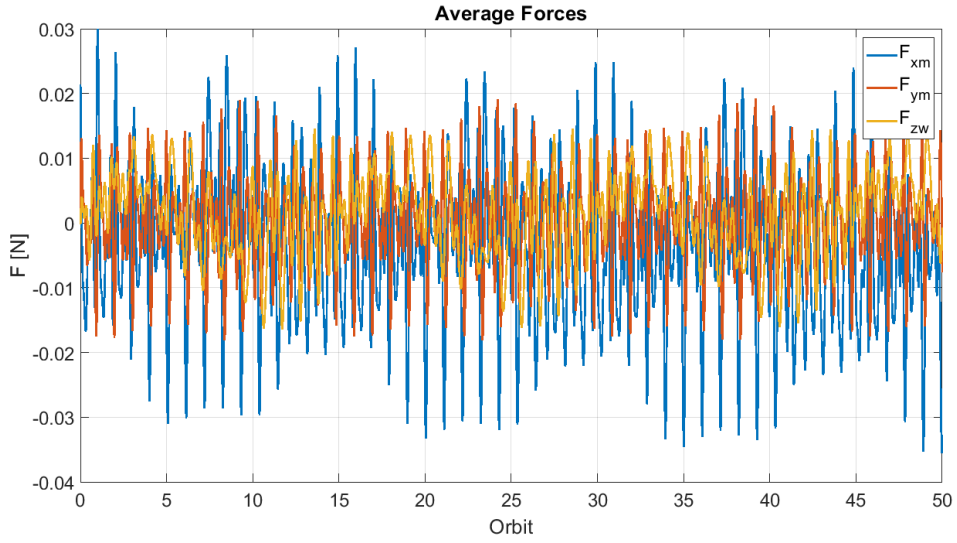


Figure 7.1: Evolution of average command forces during 50 orbits.

- **Differential Forces**

By subtracting the control forces acting on each satellite from the average of the forces calculated earlier, the differential forces acting on the different bodies can be obtained.

As it is possible to guess from the equation of relative dynamics, the differential forces cause relative motion between the satellites in the system. Indeed, thanks to these forces it is possible to control the position of one satellite relative to the other.

These can be calculated as:

$$\begin{aligned} \Delta F_{x1} &= F_{x1} - F_{xm} & \Delta F_{y1} &= F_{y1} - F_{ym} & \Delta F_{z1} &= F_{z1} - F_{zm} \\ \Delta F_{x2} &= F_{x2} - F_{xm} & \Delta F_{y2} &= F_{y2} - F_{ym} & \Delta F_{z2} &= F_{z2} - F_{zm} \end{aligned} \quad (7.2)$$

The evolution of these forces over time can be seen in figure 7.2.

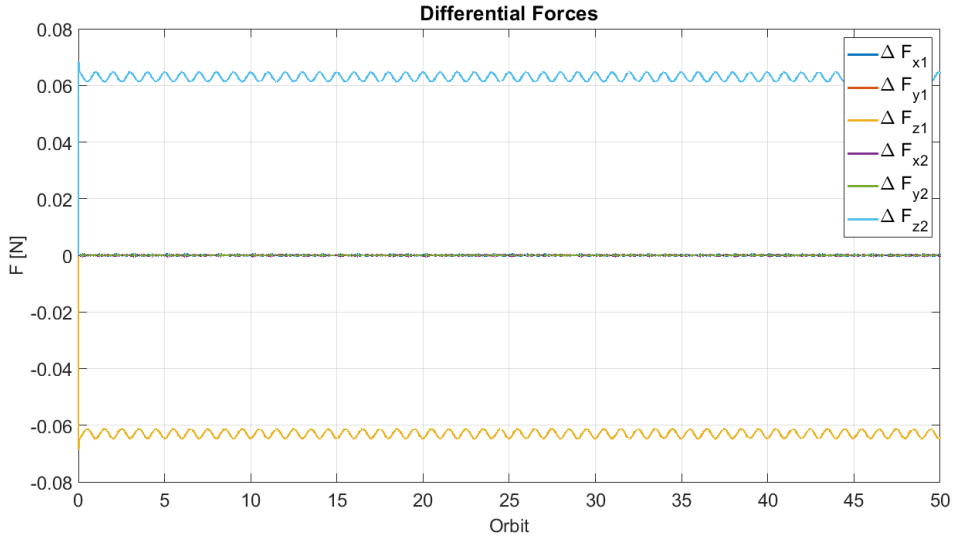


Figure 7.2: *Evolution of differential command forces during 50 orbits.*

As mentioned above, the only forces useful for managing the relative position between satellites in the system are differential forces. Analyzing the figure 7.2, depicting the trend of these forces over time, it is immediately apparent that the preponderant components are those in the across-track direction, which are orders of magnitude greater than the others. This can be easily explained by observing how these forces, being directed along the tether but in opposite directions, generate tension, analogous to what comes naturally due to the gravitational gradient, in the case where the system is oriented radially.

7.2 Validation of the Decomposition

To validate the decomposition made in the last section, a simulation was then carried out to attest that indeed differential forces alone are able to keep the system stable in the across-track configuration.

Given the small significance of the components of the differential forces in the radial and along-track directions, it was considered to apply only the force in the across-track direction to the two satellites of the system in order to verify that this is sufficient to keep it in the desired configuration.

The simulation performed, which lasted 5 orbits, took into account the same parameters used for the free propagation described in the last chapter, but adding the differential force only in the across-track direction on the two satellites.

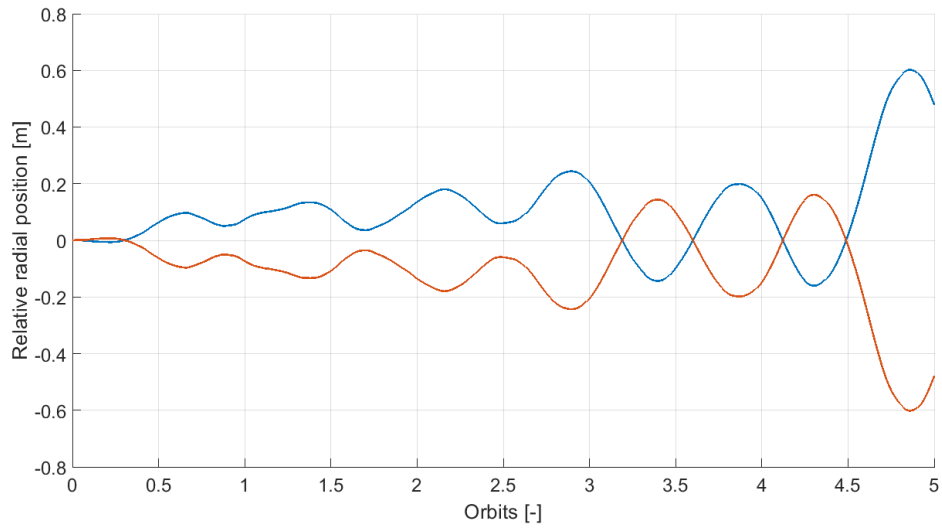


Figure 7.3: Evolution of the radial position of the 2 masses representing the EndFire Array, controlled using only the across-track force.

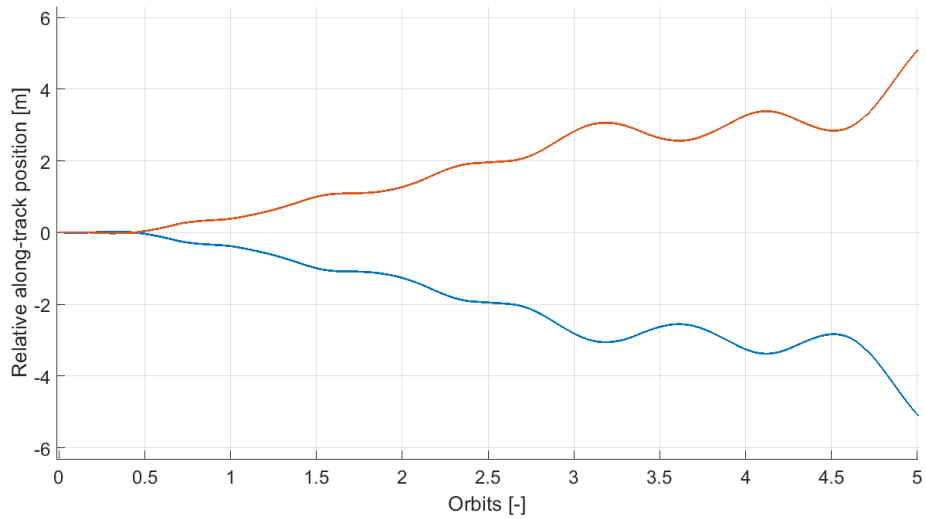


Figure 7.4: Evolution of the along-track position of the 2 masses representing the EndFire Array, controlled using only the across-track force.

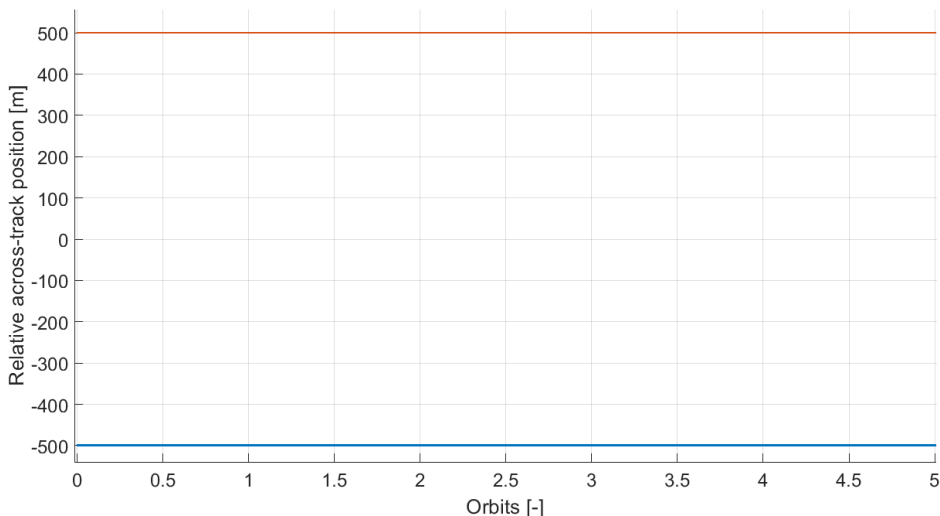


Figure 7.5: *Evolution of the across-track position of the 2 masses representing the EndFire Array, controlled using only the across-track force.*

As can be seen from the plot in the figure 7.5, the system manages to maintain its across-track position perfectly during the five orbits. Regarding the evolution of the along-track and radial positions (figures 7.3 and 7.4), it can be seen that these present oscillations of the order of magnitude of the meter. Oscillations of a similar order of magnitude could be observed in the case of free propagation of the system in radial configuration.

From this analysis, we can therefore conclude that it is possible to stabilize a system in an across-track configuration by introducing forces of the order of 60 [mN]. These forces, in fact, artificially generate the stabilizing effect that is naturally provided by the gravitational gradient when the system is in radial configuration.

7.3 Aerodynamic Stabilization

As seen, by generating a simple constant force on the two satellites at the end of the system, the stabilization of the across-track configuration can be achieved.

Given the near-constant nature in modulus and direction of the force required, the study of alternative methods for generating it is of particular interest. By being able to generate the force, or part of it, by alternative methods, the use of thrusters could be limited, thus saving propellant and extending mission duration.

These characteristics led to further studies and discussions that resulted in consideration of the possibility of introducing aerodynamic surfaces to generate the

required force, so as to take advantage of the rarefied atmosphere that characterizes Low Earth Orbit. [24]

7.3.1 Modeling Aerodynamic Surfaces

For the generation of the necessary aerodynamic forces, consider the introductions of two steerable surfaces for each end satellite. A schematic representation of the new model can be observed in figure 7.6.

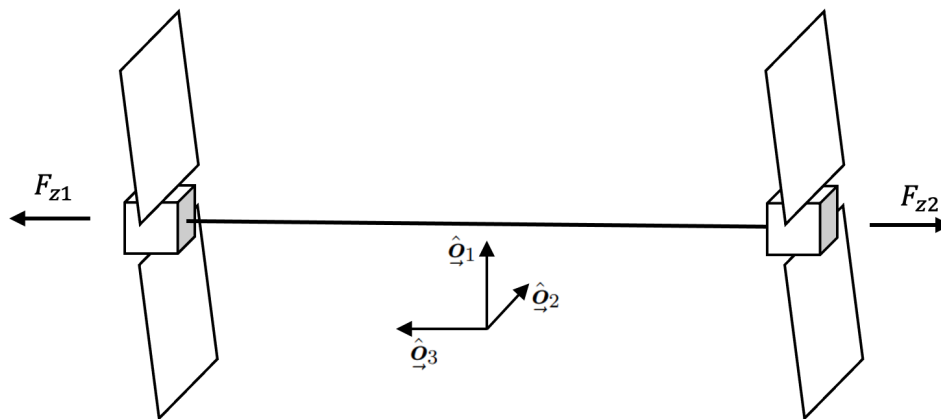


Figure 7.6: *Non-scale schematization of the system with aerodynamic surfaces.*

For the present study, given the size and mass of the leading satellites, each of the moving surfaces was considered to be rectangular and of the size of $A_w = 10 \text{ [m}^2\text{]}$. These, by electrical actuation, are able to change their angle in a range from 0 to 45 degrees, so that they can perform active force control.

Despite the considerable size of the surfaces, it is necessary to consider that, in reference orbits, due to atmospheric rarefaction, the dynamic pressure acting on these surfaces will be very small. Consequently, it is possible to obtain aerodynamic surfaces with very light structures.

Deployable systems are particularly suitable for this purpose. These systems would allow the necessary surfaces to be obtained while keeping the weight and dimensions of the satellite during launch limited.

Given the order of magnitude of the altitudes at which the system operates, the aerodynamic model of free molecular flow can be considered. This model is valid for very low pressures and densities, so it is particularly suited to modeling aerodynamic phenomena in Low Earth Orbit.

Considering the assumption of an infinitely thin flat plate in a completely rarefied flow regime and specular reflection, it is possible to obtain a first approximation of the value of the lift (C_{Lw}) and drag coefficient (C_{Dw}) of the surfaces as a function of the angle of attack of the surface (α). [25]

These can be determined through the formulas:

$$C_{Lw} = \frac{4}{\sqrt{\pi}s} \cos(\alpha) \sin(\alpha) e^{-s^2 \sin^2(\alpha)} + 2 \cos(\alpha) \left(2 \sin^2(\alpha) + \frac{1}{s^2} \right) \operatorname{erf}(s \sin(\alpha)) \quad (7.3)$$

$$C_{Dw} = \frac{4}{\sqrt{\pi}s} \sin^2(\alpha) e^{-s^2 \sin^2(\alpha)} + 4 \sin(\alpha) \left(\sin^2(\alpha) + \frac{1}{2s^2} \right) \operatorname{erf}(s \sin(\alpha)) \quad (7.4)$$

Where:

$$s = \frac{\|\mathbf{v}\|}{\sqrt{2RT}} \quad \operatorname{erf}(x) = \frac{2}{\sqrt{\pi}} \int_0^x e^{-t^2} dt$$

Denoting by \mathbf{v} the relative velocity between satellite atmosphere and by T the atmospheric temperature.

The Bates profile [26][27], which provides an approximation of temperature as a function of altitude for altitudes greater than 120 km, was used to model the temperature trend:

$$T = T_\infty - (T_\infty - T_0) e^{k(z-z_0)} \quad (7.5)$$

Where:

$$T_0 = 355 \text{ [K]} \quad z_0 = 120 \text{ [km]} \quad 740 \text{ [K]} < T_\infty < 740 \text{ [K]}$$

Using the values of the relative velocity the atmosphere extrapolated from the previous simulations and considering the range of temperatures between which T varies, it can be observed that the value of the parameter is always between:

$$s_{min} = \frac{\|\mathbf{v}_{min}\|}{\sqrt{2RT_{max}}} \simeq 8.7 < s < 17.2 \simeq s_{max} = \frac{\|\mathbf{v}_{max}\|}{\sqrt{2RT_{min}}}$$

Consequently, by entering the values of s into the equations, it can be seen that the two coefficients can be approximated as:

$$\widehat{C}_{Lw} = 4 \cos(\alpha) \sin^2(\alpha) \quad (7.6)$$

$$\widehat{C}_{Dw} = 4 \sin^3(\alpha) \quad (7.7)$$

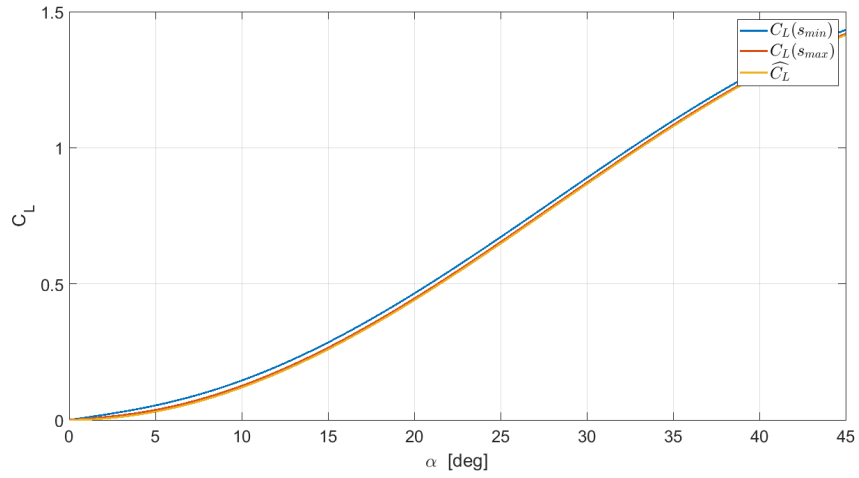


Figure 7.7: Comparison between the approximate value of the lift coefficient and that obtained by the complete formula for the maximum and minimum values of the parameter s .

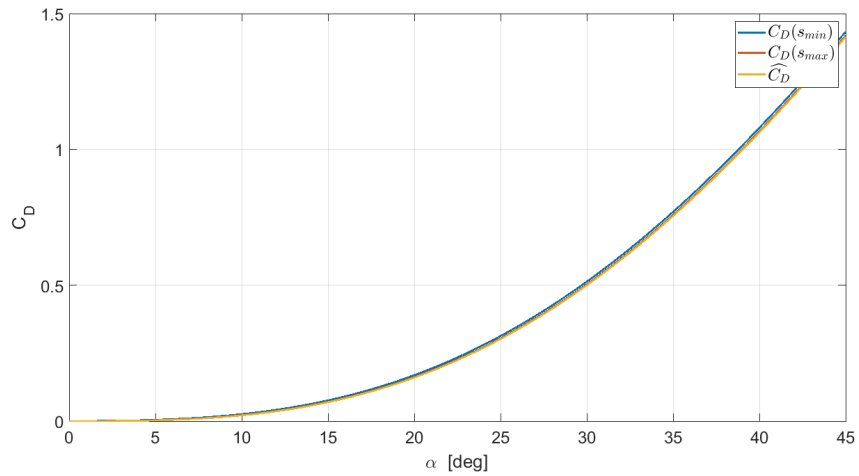


Figure 7.8: Comparison between the approximate value of the drag coefficient and that obtained by the complete formula for the maximum and minimum values of the parameter s .

Comparing the values of the approximation with those obtained with the complete formulas in the cases of s_{max} and s_{min} (figures 7.8, 7.7), it can be deduced that it is possible to consider in the first approximation the aerodynamic coefficients functions of the angle of attack alone, neglecting the small influence of temperature

and velocity.

From these coefficients, it will then be possible to determine the aerodynamic forces generated by these surfaces similarly to what was done previously for the drag perturbation (equation 3.5).

The modules of the forces generated by the surfaces could then be obtained as:

$$D_w = -\frac{1}{2}\rho_{atm}C_{Dw}A_w\mathbf{v}^2 \quad L_w = -\frac{1}{2}\rho_{atm}C_{Lw}A_w\mathbf{v}^2 \quad (7.8)$$

Analogous to what has been considered for drag perturbations, the force D_w will be directed parallel to the motion but in the opposite direction. In contrast, the force L_w generated by the surface will be perpendicular to the satellite's motion. Considering that in order to effect a stabilization of the system, it is necessary to obtain a force in the across-track direction, and that the drag will act exclusively in the along-track direction opposing the motion, it can be deduced that the component that will have to be relied upon to generate the necessary control force will be L_w .

7.3.2 Effectiveness Analysis of the Aerodynamic Control System

To test the operation and effectiveness of the aerodynamic control system, 3 different simulations were carried out over a period of 2 orbits.

The three different simulations used parameters similar to those used so far. The only parameter that differs and varies in the three simulations is the average altitudes of the orbit. The average altitudes used for the 3 simulations are 200 [km], 250 [km] and 300 [km], respectively.

Lower altitudes were chosen than the one used so far (500 [km]) because, as will be seen in the analysis, the generation of aerodynamic forces of the order of magnitude of those needed (using surfaces of a plausible size) is not possible at excessively high altitudes.

For each simulation presented, it was considered a combination of an *LQR* controller with a Discrete Time Kalman Filter, similar to that described in the previous chapter. The generated control forces were at this point decomposed, isolating the differential forces required to maintain the across-track configuration.

At this point it was considered to use the aerodynamic control system to generate the control forces, compensated by a thruster contribution in case this was not sufficient. Proceeding similarly for the three cases, it was possible to determine the utility of the aerodynamic contribution for the 3 different orbits, so that the limitations and advantages of this system could be understood.

In the figures 7.9, 7.10 and 7.11, it is possible to observe for the different cases the contribution of the aerodynamic forces (F_a) and that of thruster forces (F_t) on the

total control force (F) required can be observed. The graphs refer to only one of the two satellites, since both behave similarly.

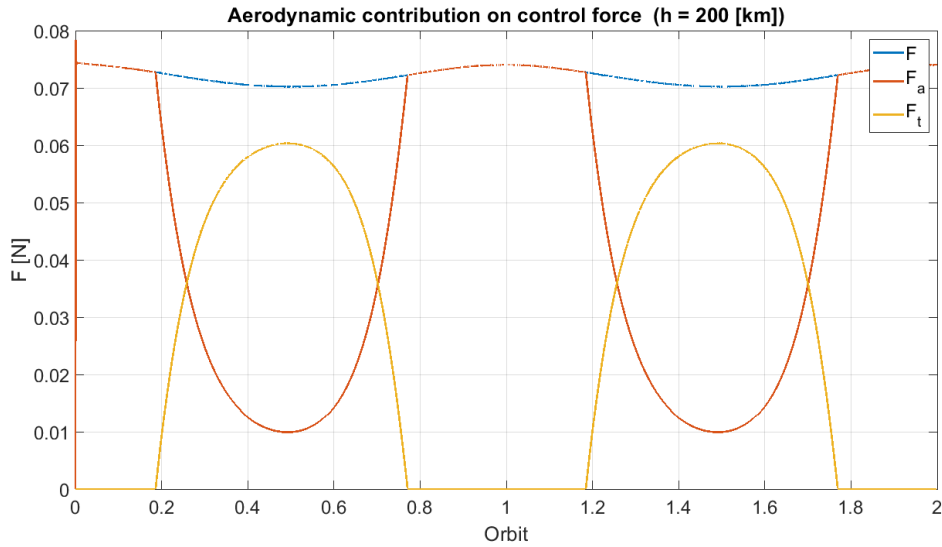


Figure 7.9: Contribution of aerodynamic forces (F_a) and thruster (F_t) forces on total control force (F) for an orbit with an average altitude of 200 km.

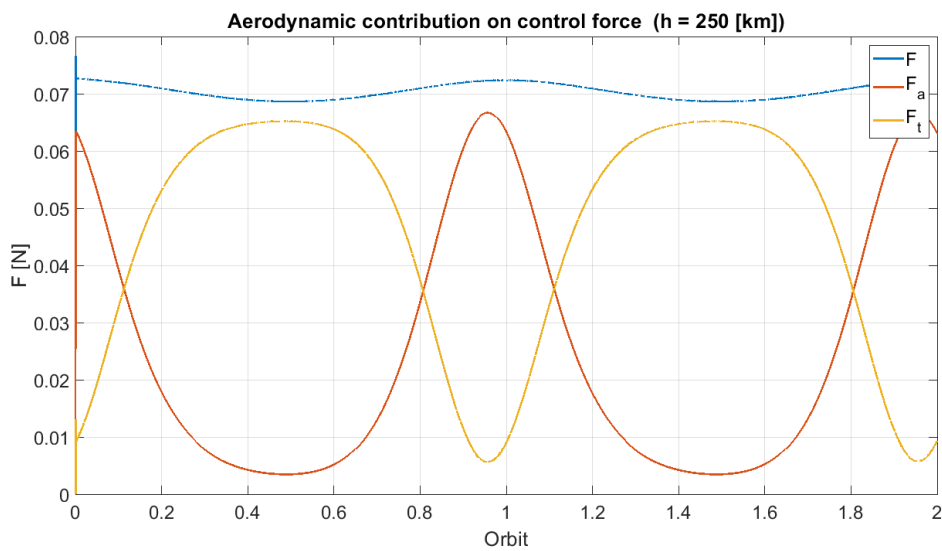


Figure 7.10: Contribution of aerodynamic forces (F_a) and thruster (F_t) forces on total control force (F) for an orbit with an average altitude of 250 km.

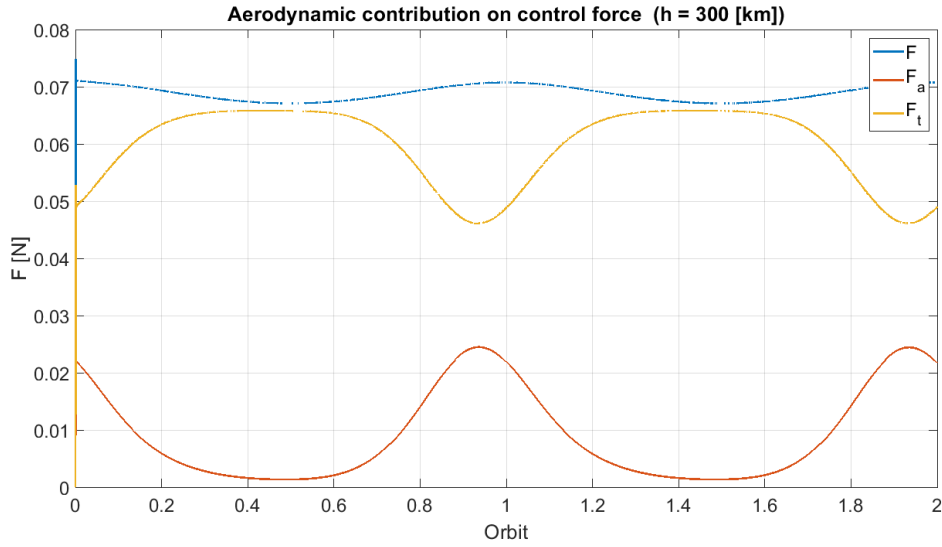


Figure 7.11: Contribution of aerodynamic forces (F_a) and thruster (F_t) forces on total control force (F) for an orbit with an average altitude of 300 km.

As can be seen from the graphs, the only case in which the aerodynamic surfaces are able to generate a force equal to or greater than that required is the orbit of a average altitude of 200 [km], the only case where the control of the angle of attack intervenes to limit the aerodynamic force to the necessary value.

In the other cases, the system is only able to generate a small part of the required force, despite always maintaining a maximum incidence.

From the analysis performed, it is immediately apparent that the aerodynamic contribution appears to be effective only in the first case (table 7.1).

In this case, the presence of the aerodynamic surfaces provides two-thirds of the force needed .

Average altitude	200 km	250 km	300 km
Aerodynamic Contribution	62.95%	35.25 %	13.29 %

Table 7.1: Aerodynamic contribution on the control force for the different orbits simulated.

It is apparent from the graphs that the main reason for the loss of effectiveness of the aerodynamic control system is due to the variation in altitude during orbit. In fact, although a nearly circular orbit ($e_0 = 0.01$) was considered in all simulations, the slight eccentricity causes a change in altitude which results in a change in density of about an order of magnitude [11], because of the exponential dependency

with altitude.

Since the control forces required to maintain the configuration remain approximately constant, the large variation in density makes it very difficult to size the system. In fact, if the system were sized to obtain the necessary force during the higher altitudes, it would result in an over-sized surface during the rest of the orbit. One possible interesting application of the system could be in perfectly circular orbits. Being always at a theoretically constant density and velocity, the dimensioning of this type of system would be simpler and more effective. However, it is necessary to consider how, since the system can only be used in low orbits, the problems relating to losses due to the atmosphere must be taken into account.

Nevertheless, it is still possible to think of other possible applications for this type of architecture. As it is feasible to obtain forces in any direction thanks to aerodynamic surfaces, it would be sufficient to use only one thruster per satellite to generate sufficient thrust to counter atmospheric drag.

If only one thruster has to be used, it could be consider using other, more complex technologies for thrust generation, such as electric propulsion. This type of propulsion has much higher specific impulses than those typical of cold gas thrusters, resulting in a much cheaper alternative.

Chapter 8

Conclusions and Future Work

In this chapter, the main results obtained during this research work will be summarized, and then possible future work to further investigate the topics of greatest interest that have emerged from the study of tethered space systems will be discussed.

8.1 Conclusions

By studying the dynamics of tethered systems, it was possible to develop and refine a calculation code capable of providing simulation of this type of system in relatively short timescales. As a result of the optimization carried out, the calculation time now required to run a simulation has been reduced to around one seventieth of the time used by the initial version of the code. Thanks to this improvement, it has been possible to work much more easily with these complex-dynamic systems, and it has been possible to carry out types of analysis that would have been impossible before.

Moreover, having both a `Python` version of the code and a `Matlab` version available, it is possible to exploit this simulation tool in different environments, taking advantage of the different extensions and toolboxes available for the two programming languages.

The simulator was then used for a study of a radially positioned EndFire Array system. Carrying out an Uncertainty Propagation analysis based on Monte Carlo methods, it was possible to further confirm the particular convenience of this

system. By analyzing the uncertainty propagation results, considering parameters similar to those used for the study of a Helix formation [19], it was possible to further deepen the work done by Mazouz et al [9] to compare these two distributed systems, being able to observe that this type of system is much more robust to uncertainty than the formation flight.

Thanks to the adaptability and versatility of the developed code, it was possible to introduce the study of another possible configuration.

Although it does not present the advantages related to the natural stabilization of a radially positioned tethered system, an across-track configuration can guarantee much more interesting performance for remote sensing.

Therefore, an analysis was performed to verify the actual costs involved in maintaining such a configuration. To do this, the problem of optimal control was introduced, explaining the linearization process of the system used to obtain an LQR corrector. In addition, the problem related to the determination of the system state was introduced, explaining the study of a centralized architecture with algorithms based on the of a Discrete Time Kalman Filter.

With this analysis, it was verified that it is possible to achieve stabilization of the system by using forces of the order of 60 mN that are constant in modulus and direction. By doing this it is indeed possible to artificially generate the effect that the gravitational gradient has on the radial configuration, making stable configurations that would normally collapse in less than one orbit.

From the results obtained, it was possible to hypothesize aerodynamic stabilization of the across-track system to limit the use of thrusters and take advantage of the atmospheric effects of Low Earth Orbit.

To do this, an aerodynamic model was introduced for free molecular flow, capable of simulating the aerodynamics of moving surfaces in a rarefied atmosphere. Using this model, it was possible to simulate the hypothetical behavior of the satellite on different reference orbits, so as to evaluate the concrete effects and possible benefits and problems of a system of this kind.

8.2 Future work

Several ideas for further investigation emerged during the study conducted, both to improve and carry forward some points already analyzed and to introduce new concepts that could be of considerable interest.

Therefore, the most interesting points for further work are presented below:

- **Development of a dedicated integration algorithm**

As mentioned in the chapter on code optimization, the critical problem for speeding up algorithms for complex dynamics systems is integration time. Introducing special integration methods for stiff equations has yielded some very interesting results. In spite of this, the algorithms used were chosen from those present by default in the available toolboxes. These methods use techniques to get good results in most application cases, but they are not optimized for the study of a specific problem. By developing an integration algorithm specifically for the case under analysis, it would be possible to further speed up the calculations so that even higher performance could be achieved.

- **Improvement of tether model**

Although the discretized mass tether model is a good approximation, it would be appropriate to introduce a model that would also simulate torsional and bending stiffness.

These would have a major impact on the attitude of the various satellites and could result in phenomenology not found with the current model.

- **Evaluation of the effectiveness of aerodynamic control on the radial configuration**

From the study on aerodynamic stabilization, it was found that due to the presence of atmosphere in Low Earth Orbit, it is possible to obtain control forces using aerodynamics surfaces. Although the forces generated is small, and are insufficient to stabilize an across-track system autonomously at high altitudes, these could be sufficient for active orbit control of already stable configurations, such as the radial one. In fact, if the control is performed continuously, the forces required to maintain the configuration do not spike, remaining constant at low values, making a continuous aerodynamic stabilization possible.

- **Evaluation of an along-track configuration with atmospheric drag control**

Finally, the latest architecture that could represent a point of interest for the future study consists of a tethered system placed on the radial plane with aerodynamic surfaces that allow the control of the atmospheric drag on the various satellites. The study of drag control of small satellites has already been deepened by other research.[28] The latter effect, however, would be particularly interesting in combination with the stabilizing effects of the gravitational gradient. In fact, it would be possible to control the orientation in terms of in-plane angle by managing the differential drag between the two satellites of the system. This would make it possible to obtain a system capable of moving at will between a radial configuration and an almost along-track configuration.

Bibliography

- [1] J. Leitner: «Formation flying: The future of remote sensing from space». In: *Proceedings 18th International Symposium on Space Flight Dynamics, ISSFD, Munich, Germany* (2004) (cit. on p. 1).
- [2] Quadrelli M.B. et al. «Formations of Tethered Spacecraft as Stable Platforms for Far IR and Sub-mm Astronomy». In: *Far IR and Submm Space Astronomy Workshop, University of Maryland College Park* (Mar. 2002) (cit. on p. 4).
- [3] Apa R. et al. «Dynamics and Control of Helical Arrays in Low Earth Orbit». In: *IEEE Aerospace Conference* (2022) (cit. on pp. 5, 6).
- [4] J. Pearson.: «Konstantin tsiolkovski and the origin of the space elevator». In: *Proceedings 48th International Astronautical Congress, IAF, Turin, Italy* (2005) (cit. on p. 6).
- [5] T. Hans et al. «Dynamics of Tethered Space Systems». In: *Routledge* (2017) (cit. on pp. 6, 23).
- [6] Quadrelli B.M. et al. «Investigation of Phase Transition-Based Tethered Systems for Small Body Sample Capture». In: *Acta Astronautica* (2011). URL: <https://doi.org/10.1016/j.actaastro.2010.08.040> (cit. on p. 6).
- [7] Wen et al. «Advances in dynamics and control of tethered satellite systems». In: *Acta Mechanica Sinica* (2008). URL: <https://doi.org/10.1007/s10409-008-0159-9> (cit. on p. 6).
- [8] P.C. Hughes.: «Spacecraft Attitude Dynamics». In: *Dover Pubns* (2004) (cit. on pp. 6, 29, 30).
- [9] R. Mazouz et al. «Dynamics and Optimal Control for Free- Flight and Tethered Arrays in Low Earth Orbit». In: *IEEE Aerospace Conference* (Mar. 2021). URL: <https://doi.org/10.1109/AERO50100.2021.9438513> (cit. on pp. 6, 97).
- [10] C. Balanis. *Antenna Theory (4th ed.)* Wiley, 2015. URL: <https://www.perlego.com/book/992658/antenna-theory-pdf> (cit. on p. 6).
- [11] O. Montenbruck and E. Gill: «Satellite Orbits - Models, Methods and Applications». In: *Pringer-Verlag Berlin Heidelberg* (2000) (cit. on pp. 20, 94).

- [12] Quadrelli B.M. et al. «Modeling and Simulation of Active Tether Systems for Planetary Exploration». In: *Acta Astronautica* 138 (Sept. 2017). URL: <https://doi.org/10.1016/j.actaastro.2016.11.010> (cit. on p. 23).
- [13] Quadrelli M.B.: «Modeling and Dynamics Analysis of Tethered Formations for Space Interferometry». In: *11th AAS/AIAA Spaceflight Mechanics Meeting, Santa Barbara, CA, USA* (Feb. 2001) (cit. on p. 23).
- [14] Quadrelli M.B.: «Effect of Distributed Rod and String Flexibility on Formation Dynamic Stability». In: *AAS/AIAA Spaceflight Mechanics Meeting, San Antonio, TX, USA* (Jan. 2002) (cit. on pp. 23, 72, 75).
- [15] Guangyan Xu and Danwei Wang. «Nonlinear Dynamic Equations of Satellite Relative Motion Around an Oblate Earth». In: *Journal of Guidance, Control, and Dynamics* (2008) (cit. on p. 35).
- [16] Quadrelli M.B. and Lorenzini E.: «Dynamics and Stability of a Tethered Centrifuge in Low Earth Orbit». In: *The Journal of the Astronautical Sciences* 40(1) (Jan. 1992) (cit. on p. 44).
- [17] M. Pastori et al. «Modeling, Dynamics, and Control of Variable Topology Tethered Space System». In: *IEEE Aerospace Conference, Big Sky, MT, USA* (Mar. 2022) (cit. on pp. 44, 72, 75).
- [18] Terejanu G. et al. «Uncertainty propagation for nonlinear dynamic systems using Gaussian mixture models». In: *Journal of guidance, control, and dynamics* 31(6) () (cit. on p. 49).
- [19] Apa R. et al. «Effective Sensitivity Analyses of Radar Systems in Formation Flying using Differential Algebra». In: (2022) (cit. on pp. 49, 67, 97).
- [20] Dinamica S.R.L. «Differential Algebra Space Toolbox». In: (). URL: <https://github.com/dacelib/dace> (cit. on p. 49).
- [21] Rasotto M. et al. «Differential algebra space toolbox for nonlinear uncertainty propagation in space dynamics». In: (2016) (cit. on p. 49).
- [22] V. Iafolla et al. «The isa accelerometer for bepicolombo mission». In: *Memorie della Societa' Astronomica Italiana Supplementi* (2011) (cit. on p. 78).
- [23] Quadrelli B.M.: «Dynamics and Control of Novel Orbiting Formations with Internal Dynamics». In: *J of Astronaut Sci* 51 (2003). URL: <https://doi.org/10.1007/BF03546301> (cit. on p. 78).
- [24] «Private discussion with Prof. Marcello Romano on the possible aerodynamic stabilization of a tethered array placed in across-track configuration». In: (June 2022) (cit. on p. 89).
- [25] Carlos L. Pulido. «Aerodynamic Lift and Drag Effects on the Orbital Lifetime Low Earth Orbit (LEO) Satellites». In: 2012 (cit. on p. 90).

- [26] K. Rawer. «Modelling of Neutral and Ionized Atmospheres». In: *Geophysik III / Geophysics III*. Ed. by Karl Rawer. Berlin, Heidelberg: Springer Berlin Heidelberg, 1984, pp. 223–535. ISBN: 978-3-642-68531-6. DOI: [10.1007/978-3-642-68531-6_3](https://doi.org/10.1007/978-3-642-68531-6_3). URL: https://doi.org/10.1007/978-3-642-68531-6_3 (cit. on p. 90).
- [27] A. E. Hedin. «A Revised thermospheric model based on mass spectrometer and incoherent scatter data: MSIS-83». In: *Journal of Geophysical Research: Space Physics* 88.A12 (1983), pp. 10170–10188. DOI: <https://doi.org/10.1029/JA088iA12p10170>. URL: <https://agupubs.onlinelibrary.wiley.com/doi/abs/10.1029/JA088iA12p10170> (cit. on p. 90).
- [28] Bevilacqua R. and Romano M. «Rendezvous Maneuvers of Multiple Spacecraft using Differential Drag under J2 Perturbation». In: *Journal of guidance, control, and dynamics* (2008) (cit. on p. 99).

Appendix A

Additional Plots Uncertainty Propagation

A.1 Uncertainty on the In-plane Angle (α)

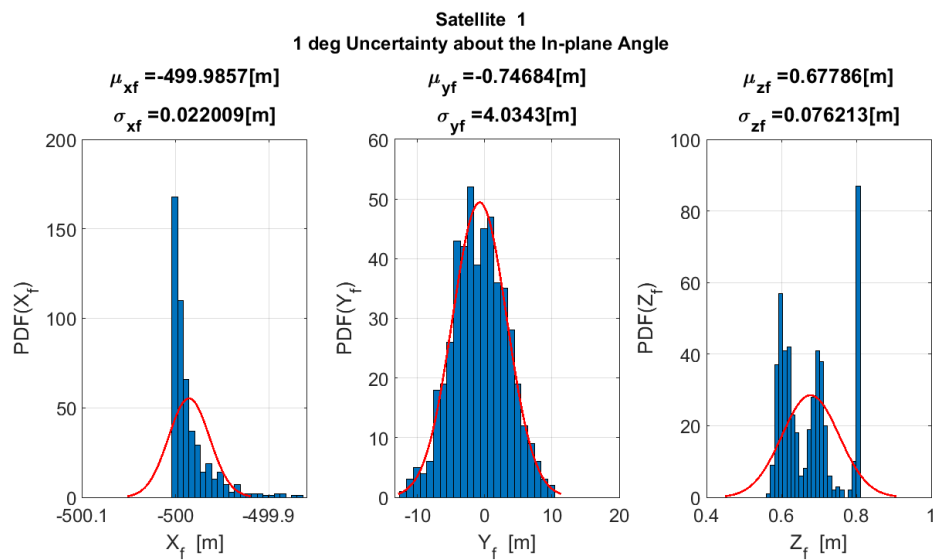


Figure A.1: Position distribution for satellite 1 after 10 orbits, uncertainty on In-plane angle

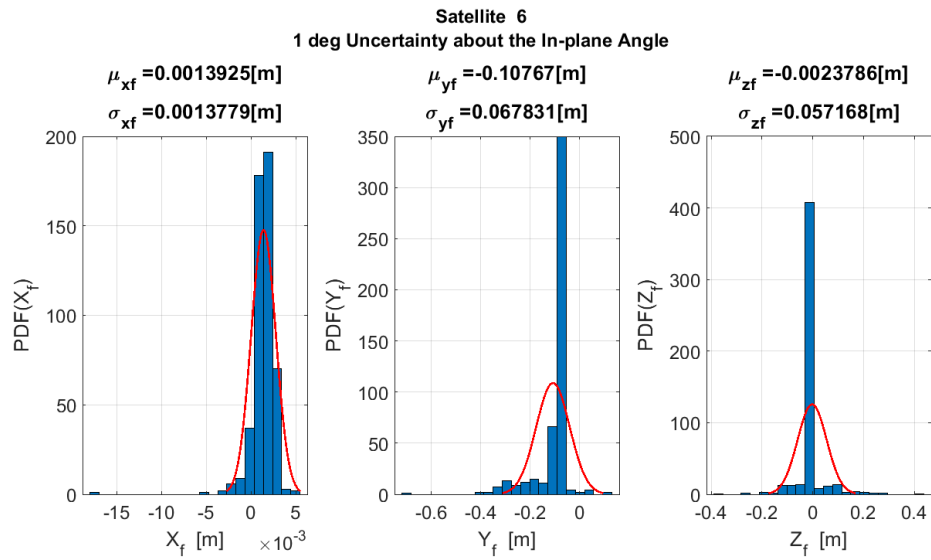


Figure A.2: Position distribution for satellite 6 after 10 orbits, uncertainty on In-plane angle

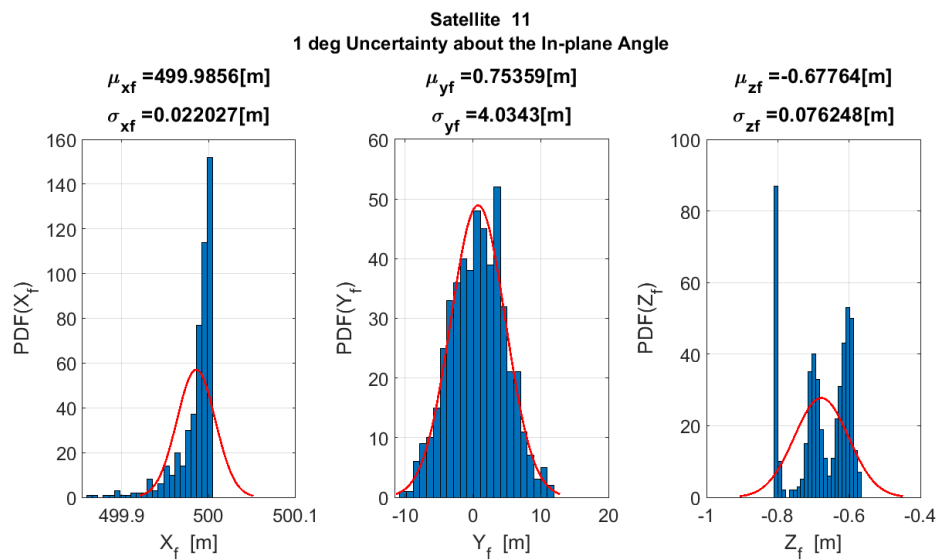


Figure A.3: Position distribution for satellite 11 after 10 orbits, uncertainty on In-plane angle

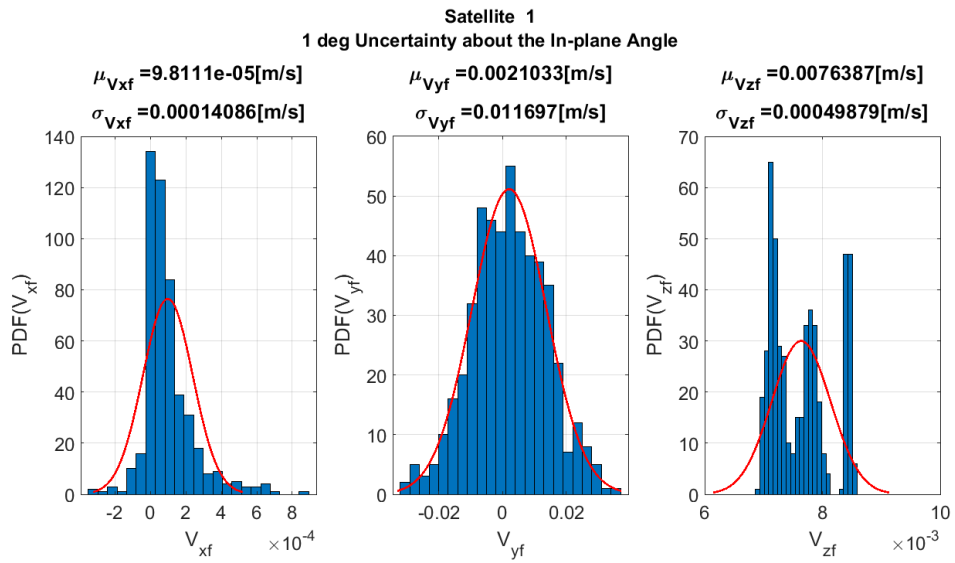


Figure A.4: Velocity distribution for satellite 1 after 10 orbits, uncertainty on In-plane angle

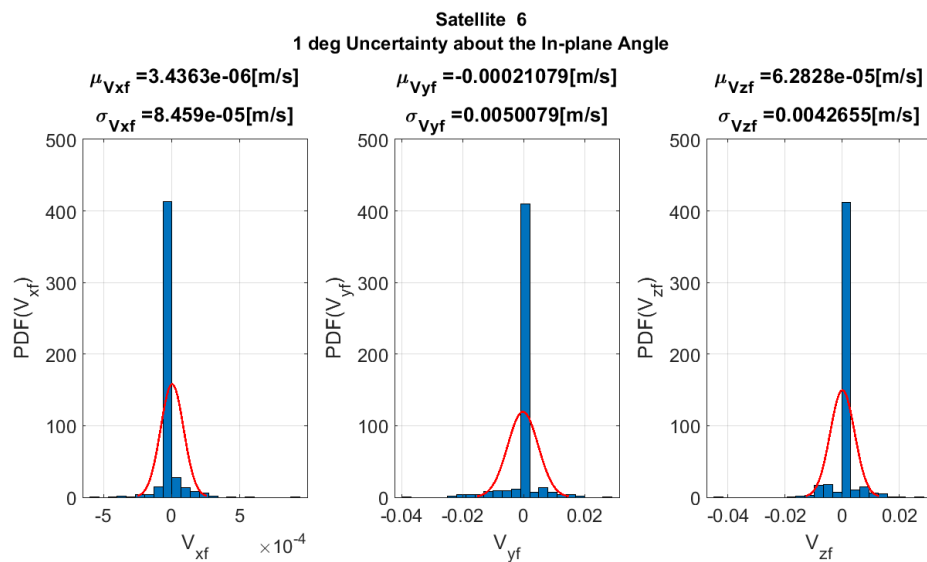


Figure A.5: Velocity distribution for satellite 6 after 10 orbits, uncertainty on In-plane angle

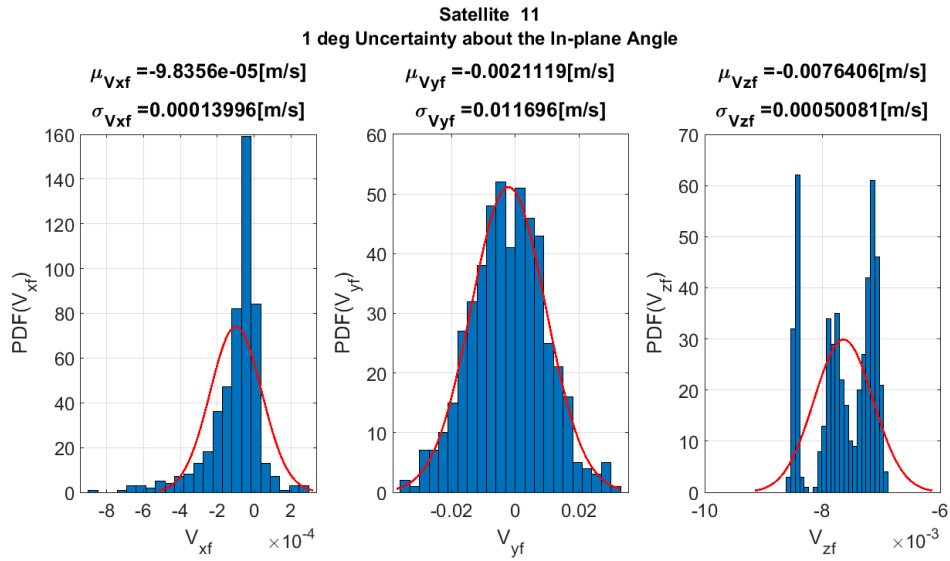


Figure A.6: Velocity distribution for satellite 11 after 10 orbits, uncertainty on In-plane angle

A.2 Uncertainty on the Out-of-plane Angle (β)

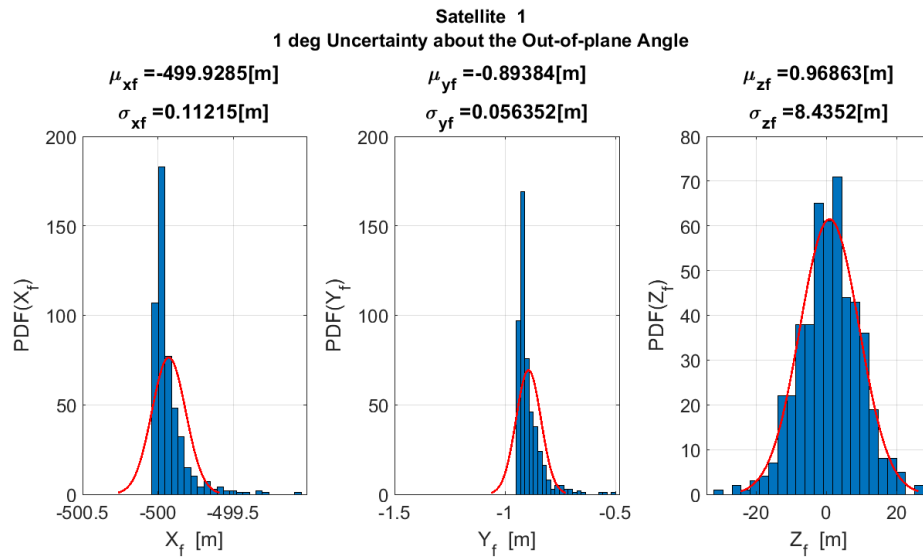


Figure A.7: Position distribution for satellite 1 after 10 orbits, uncertainty on Out-of-plane angle

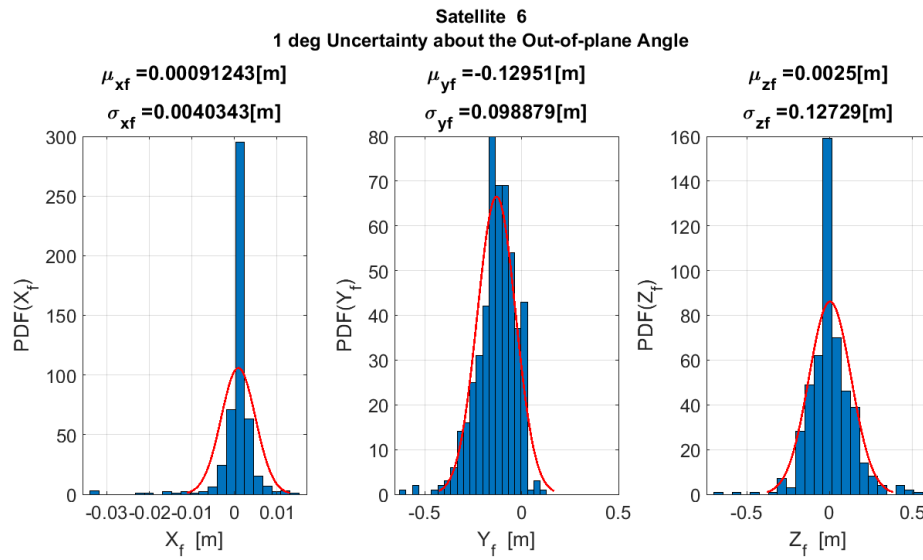


Figure A.8: Position distribution for satellite 6 after 10 orbits, uncertainty on Out-of-plane angle

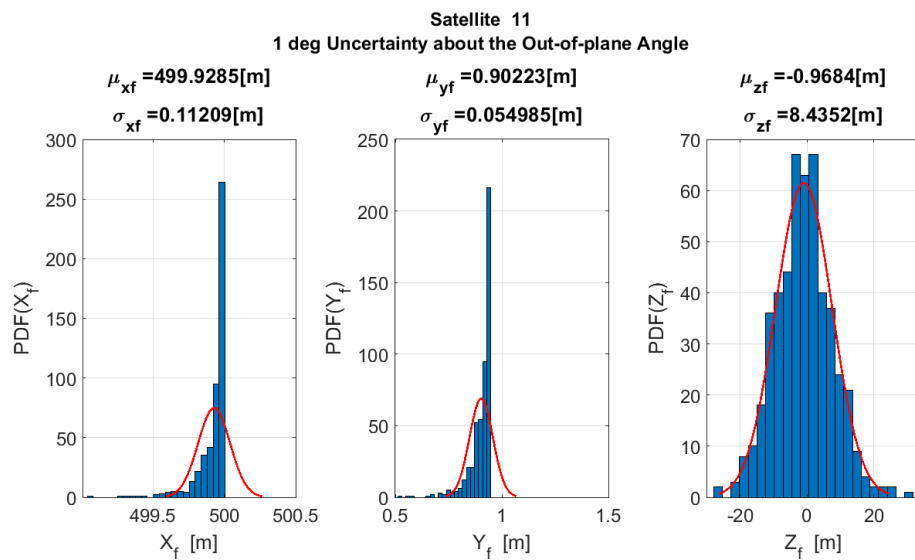


Figure A.9: Position distribution for satellite 11 after 10 orbits, uncertainty on Out-of-plane angle

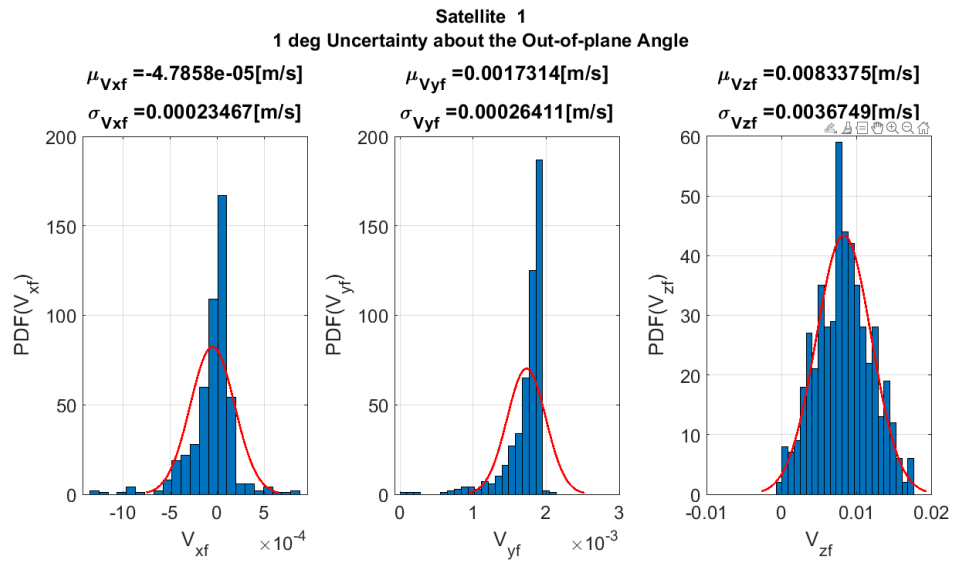


Figure A.10: Velocity distribution for satellite 1 after 10 orbits, uncertainty on Out-of-plane angle

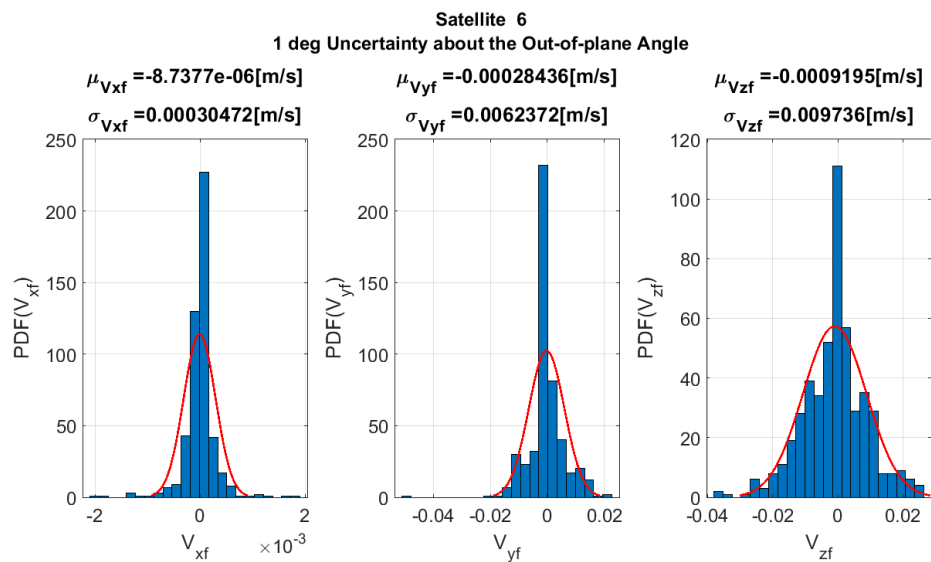


Figure A.11: Velocity distribution for satellite 6 after 10 orbits, uncertainty on Out-of-plane angle

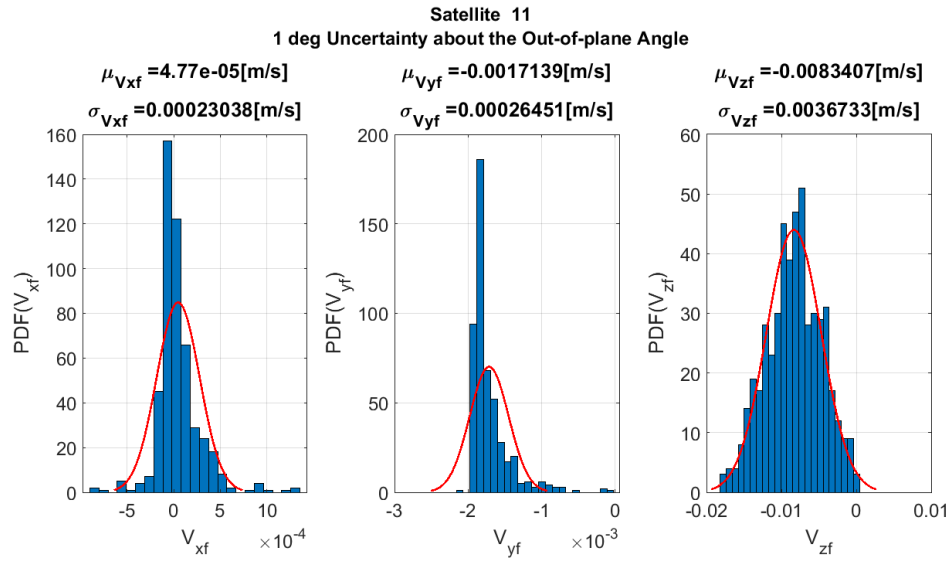


Figure A.12: Velocity distribution for satellite 11 after 10 orbits, uncertainty on Out-of-plane angle

A.3 Uncertainty on Masses (m_i)

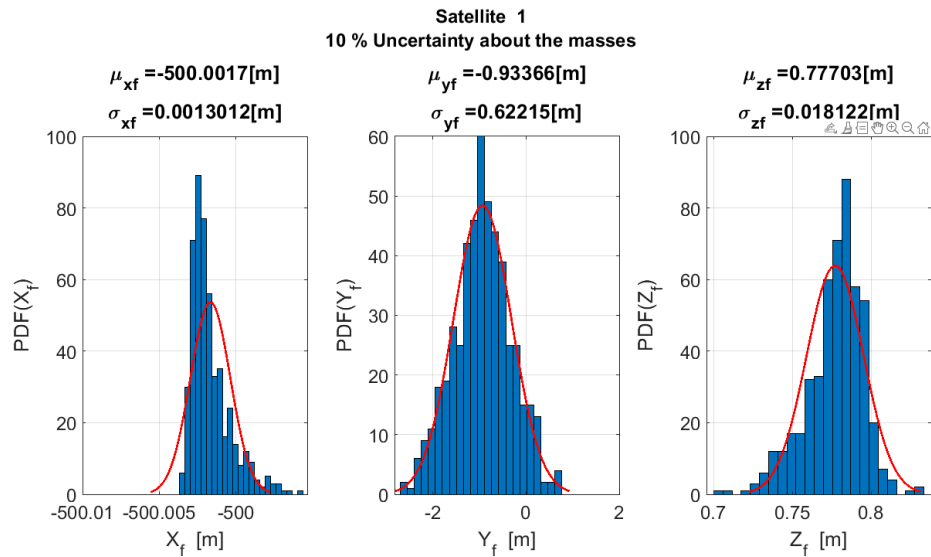


Figure A.13: Position distribution for satellite 1 after 10 orbits, uncertainty on masses

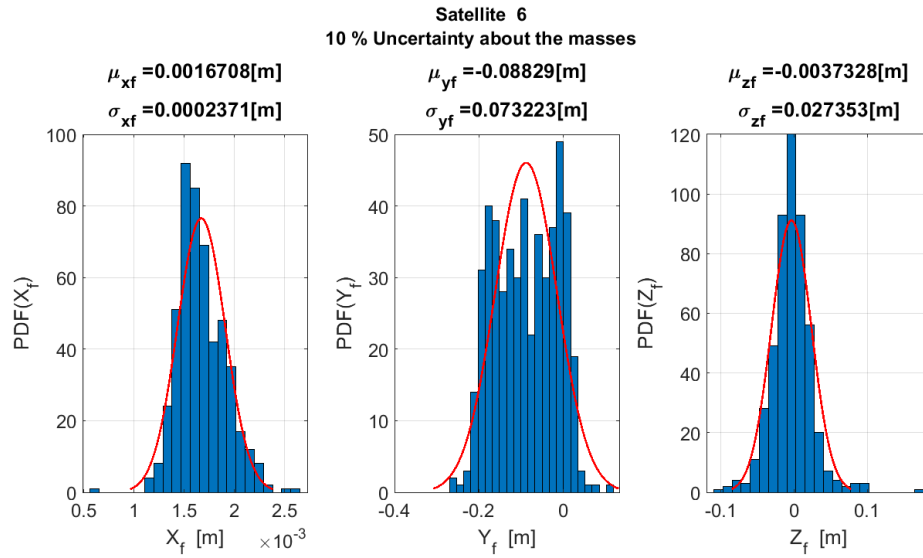


Figure A.14: Position distribution for satellite 6 after 10 orbits, uncertainty on masses

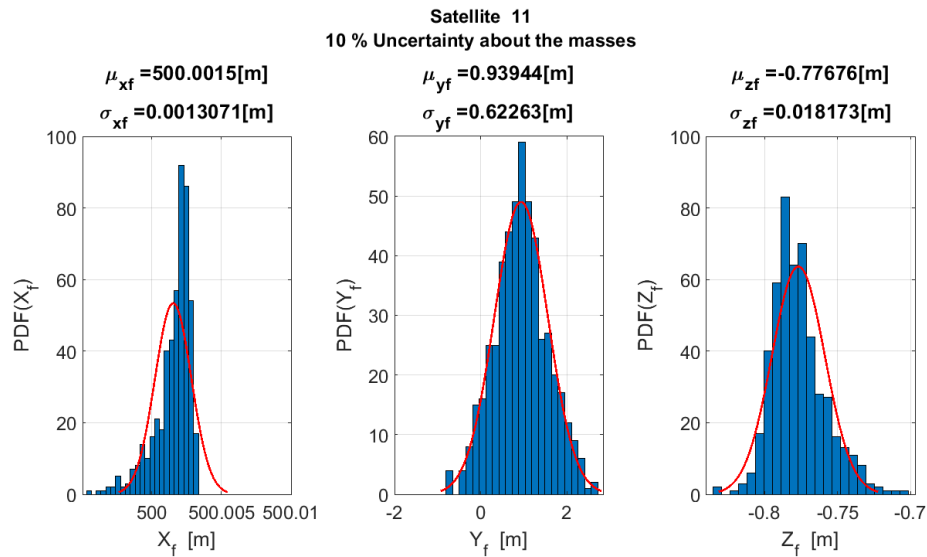


Figure A.15: Position distribution for satellite 11 after 10 orbits, uncertainty on masses

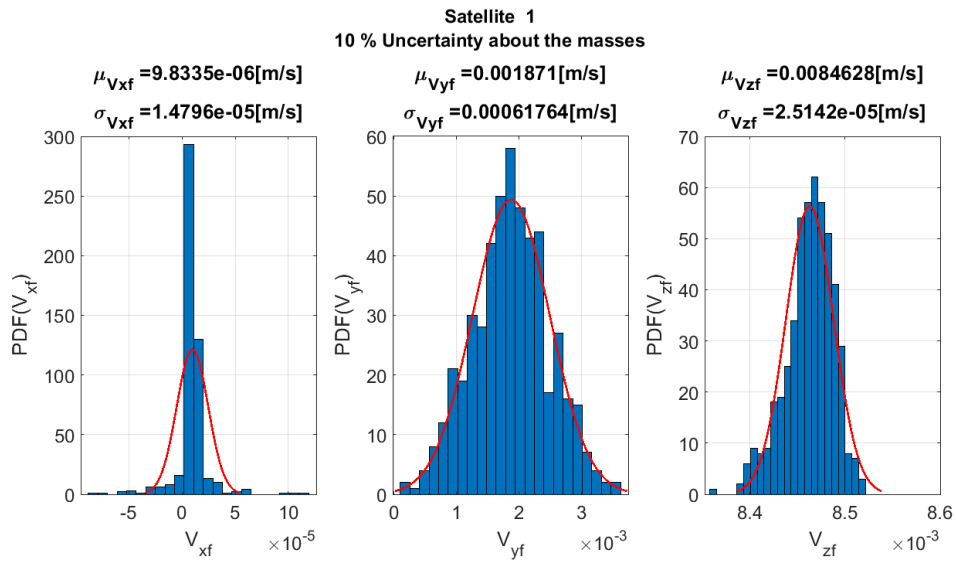


Figure A.16: Velocity distribution for satellite 1 after 10 orbits, uncertainty on masses

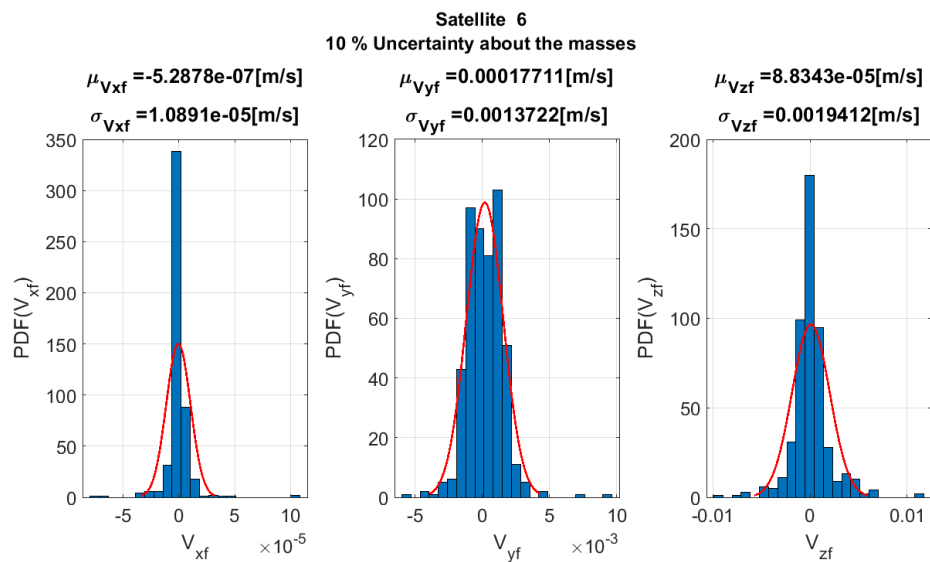


Figure A.17: Velocity distribution for satellite 6 after 10 orbits, uncertainty on masses

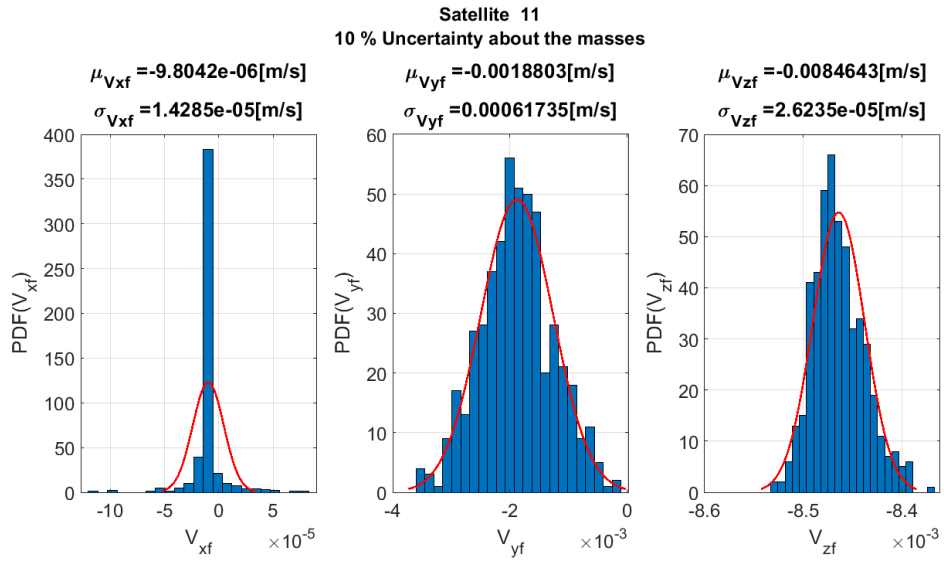


Figure A.18: Velocity distribution for satellite 11 after 10 orbits, uncertainty on masses

A.4 Uncertainty on Surfaces (A_i)

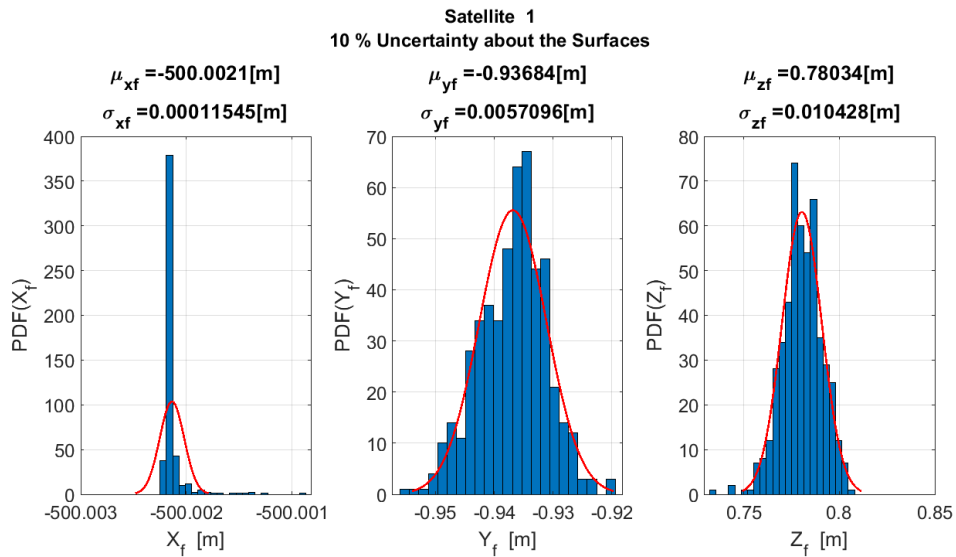


Figure A.19: Position distribution for satellite 1 after 10 orbits, uncertainty on surfaces

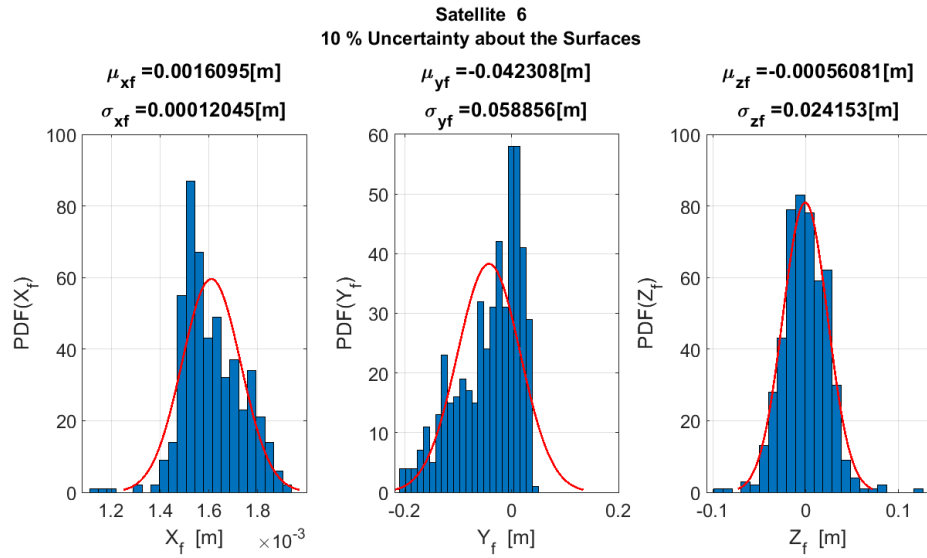


Figure A.20: Position distribution for satellite 6 after 10 orbits, uncertainty on surfaces

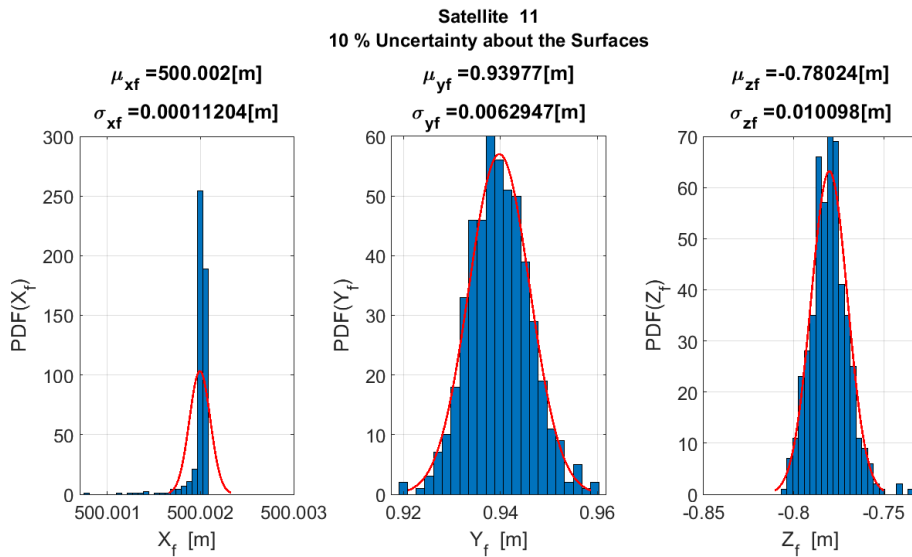


Figure A.21: Position distribution for satellite 11 after 10 orbits, uncertainty on surfaces

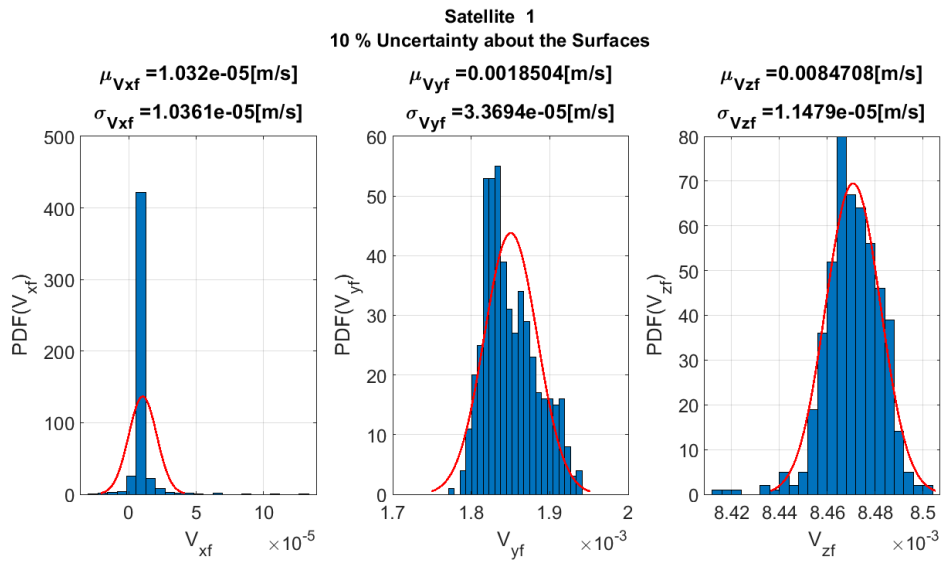


Figure A.22: Velocity distribution for satellite 1 after 10 orbits, uncertainty on surfaces

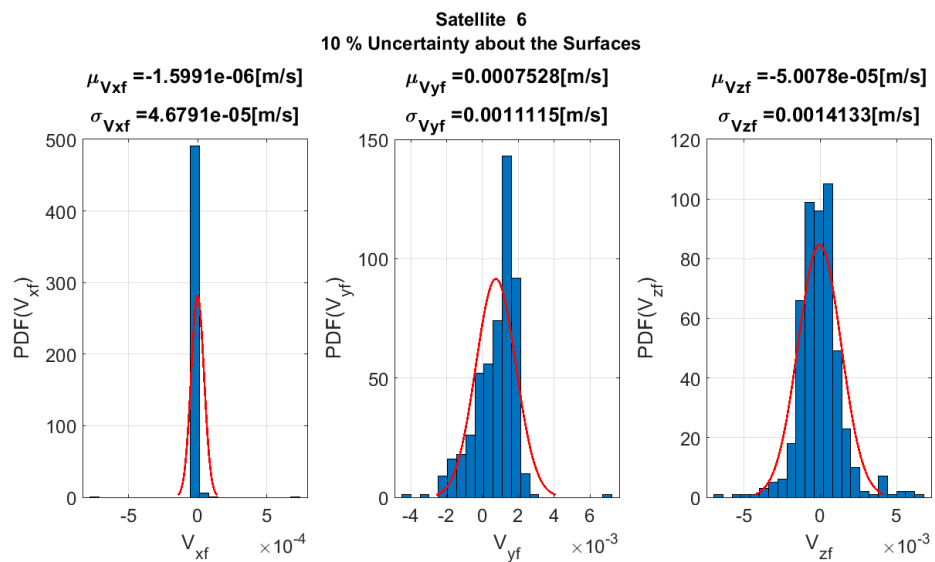


Figure A.23: Velocity distribution for satellite 6 after 10 orbits, uncertainty on surfaces

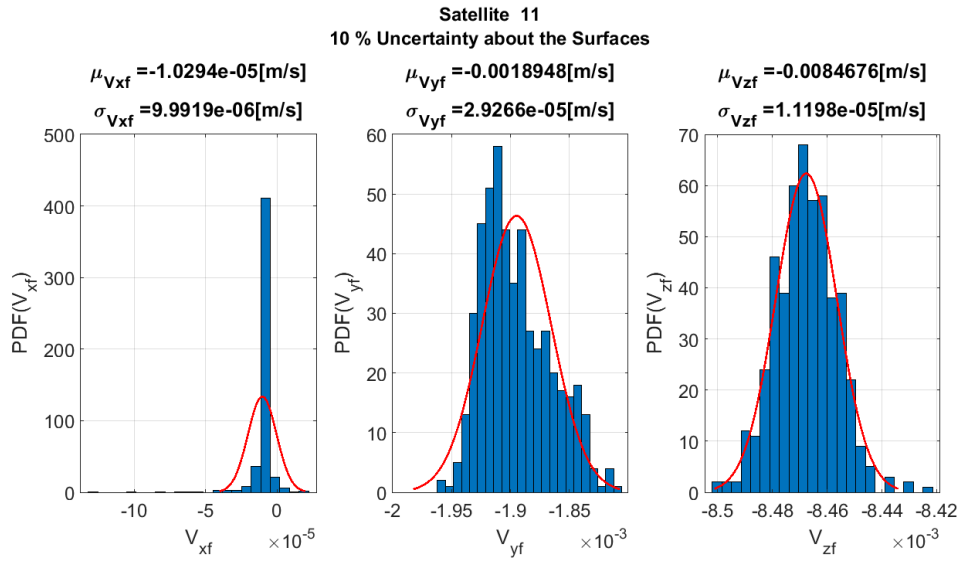


Figure A.24: Velocity distribution for satellite 11 after 10 orbits, uncertainty on surfaces

A.5 Uncertainty on Drag Coefficients (CD_i)

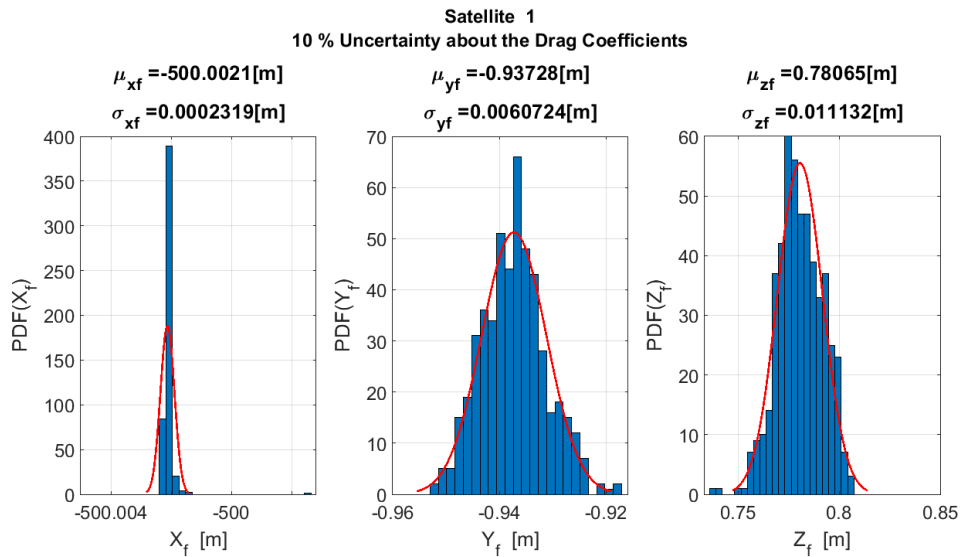


Figure A.25: Position distribution for satellite 1 after 10 orbits, uncertainty on drag coefficients

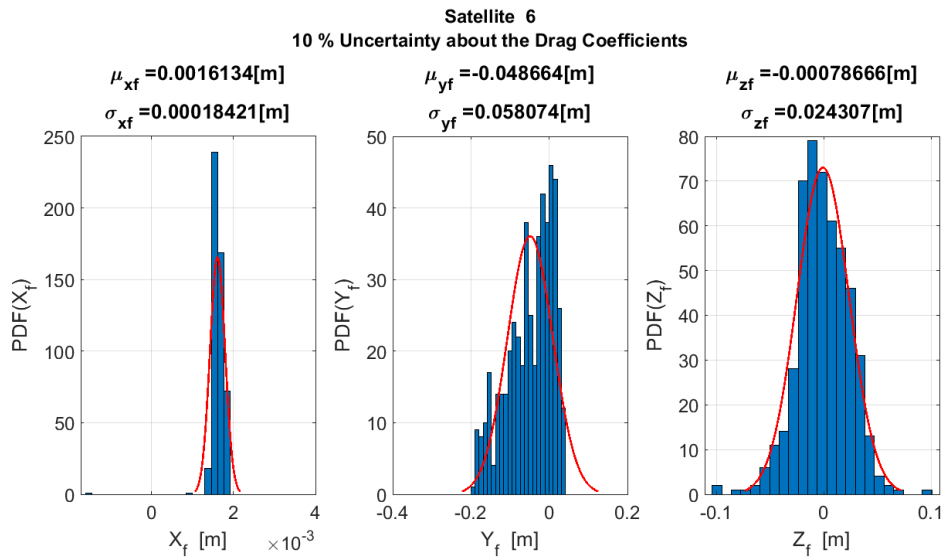


Figure A.26: Position distribution for satellite 6 after 10 orbits, uncertainty on drag coefficients

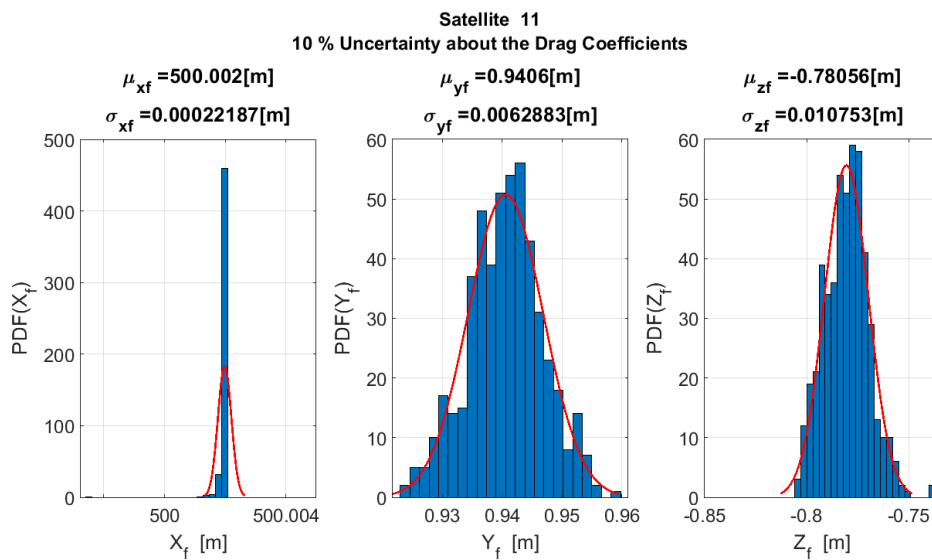


Figure A.27: Position distribution for satellite 11 after 10 orbits, uncertainty on drag coefficients

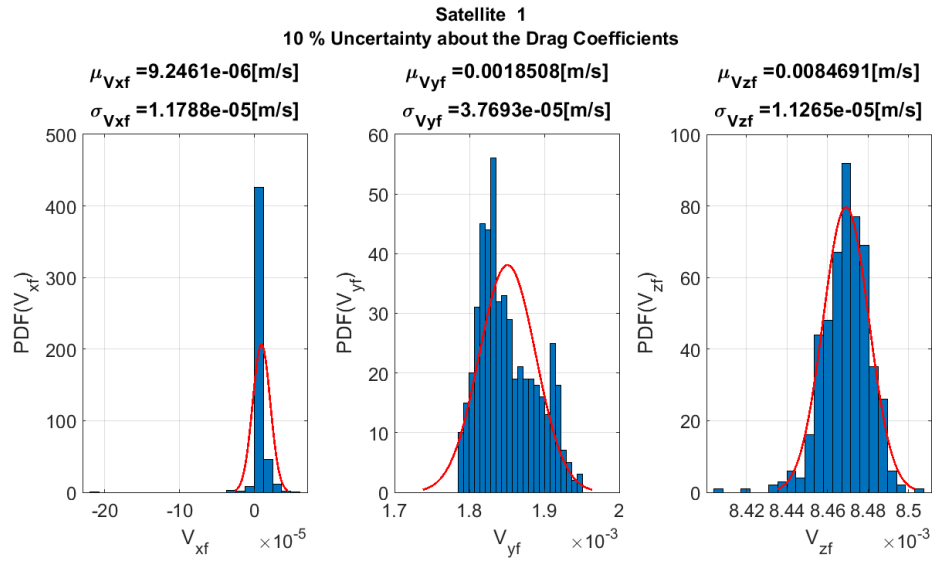


Figure A.28: Velocity distribution for satellite 1 after 10 orbits, uncertainty on drag coefficients

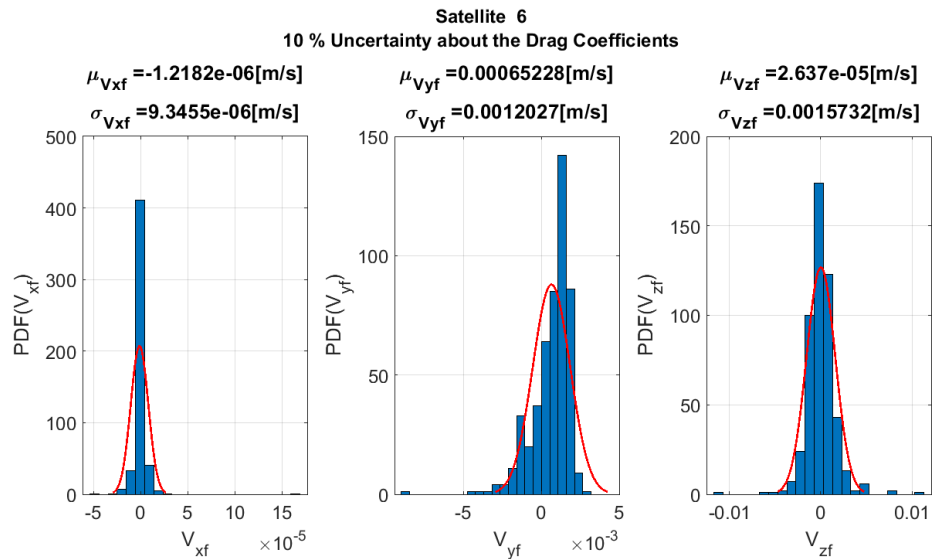


Figure A.29: Velocity distribution for satellite 6 after 10 orbits, uncertainty on drag coefficients

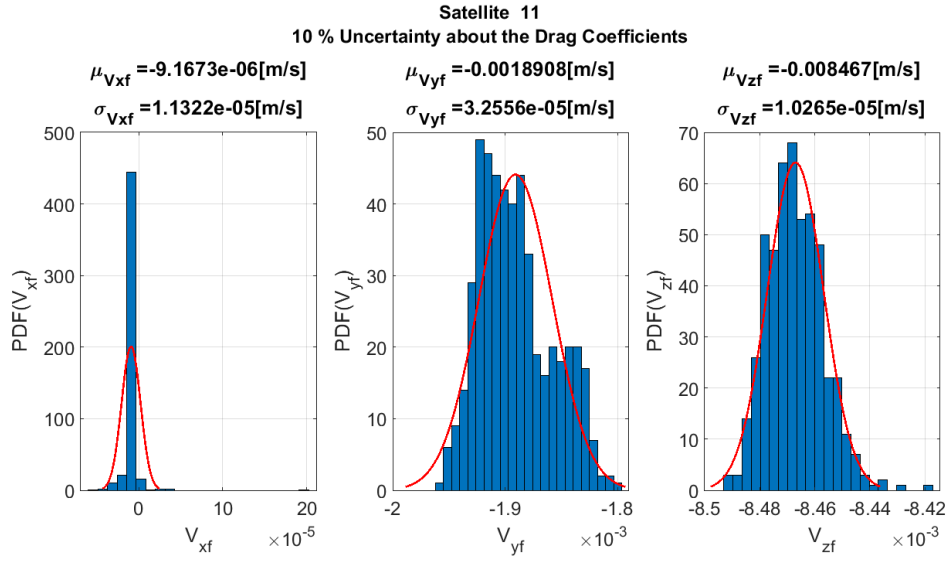


Figure A.30: Velocity distribution for satellite 11 after 10 orbits, uncertainty on drag coefficients

A.6 Uncertainty on Reflectivity Coefficients (CD_i)

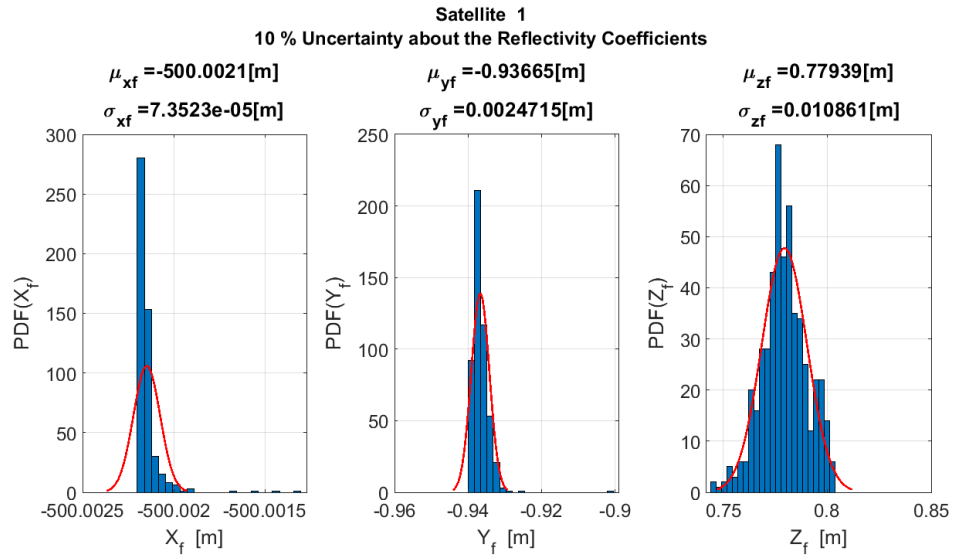


Figure A.31: Position distribution for satellite 1 after 10 orbits, uncertainty on reflectivity coefficients

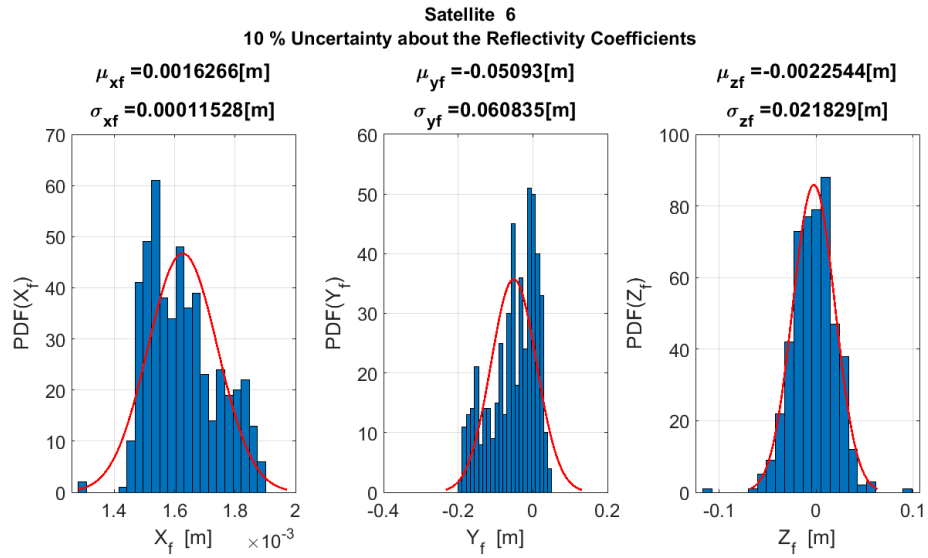


Figure A.32: Position distribution for satellite 6 after 10 orbits, uncertainty on reflectivity coefficients

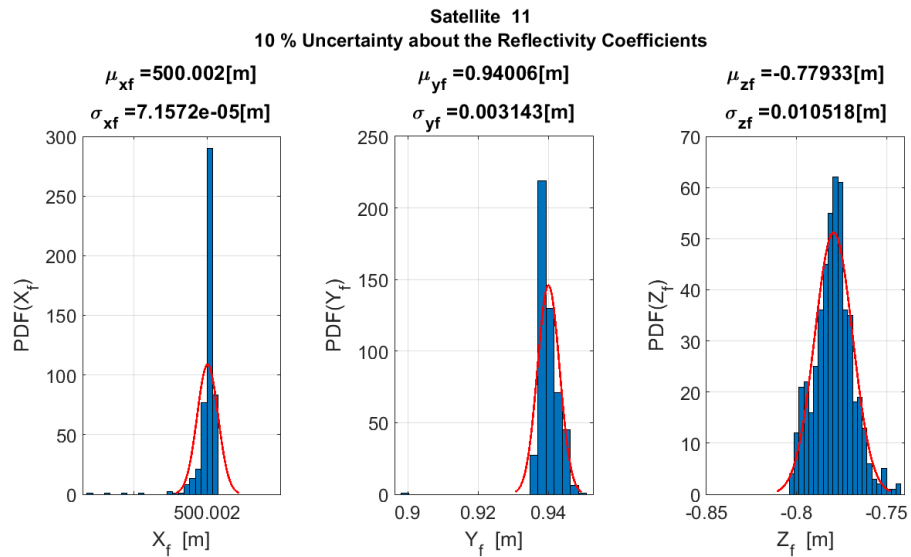


Figure A.33: Position distribution for satellite 11 after 10 orbits, uncertainty on reflectivity coefficients

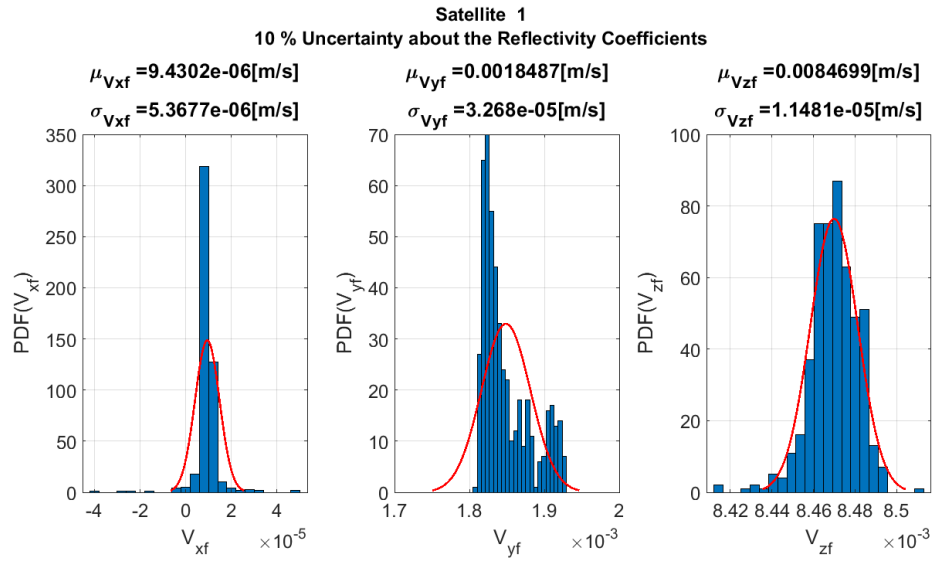


Figure A.34: Velocity distribution for satellite 1 after 10 orbits, uncertainty on reflectivity coefficients

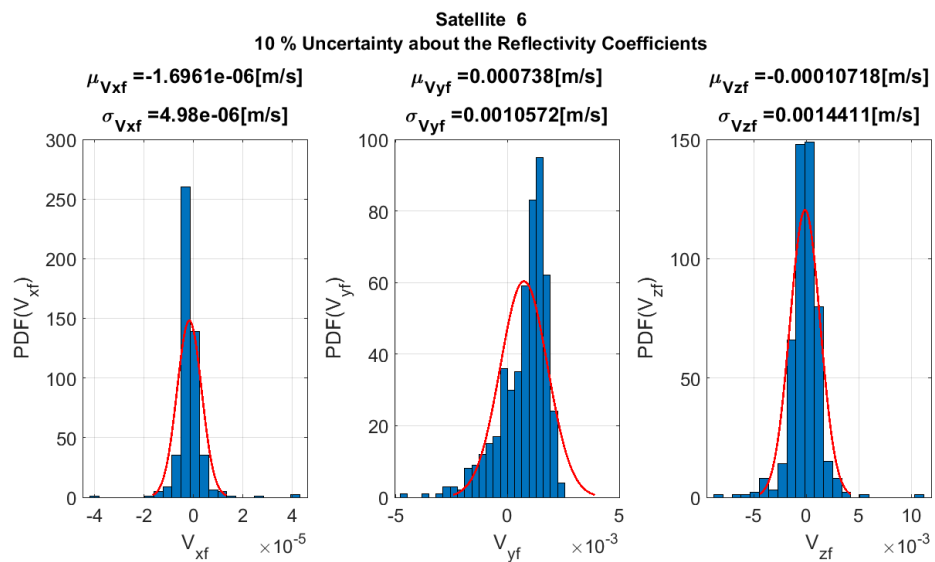


Figure A.35: Velocity distribution for satellite 6 after 10 orbits, uncertainty on reflectivity coefficients

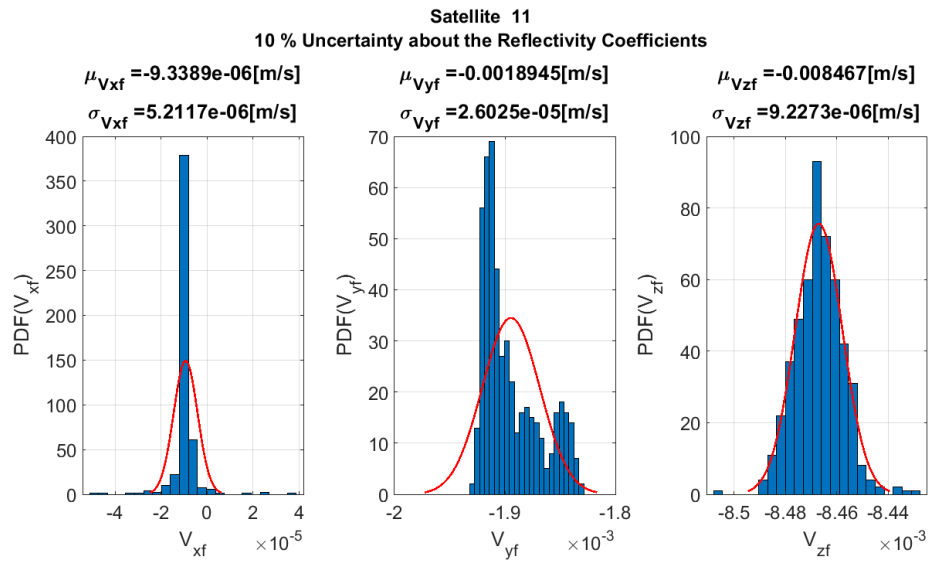


Figure A.36: Velocity distribution for satellite 11 after 10 orbits, uncertainty on reflectivity coefficients

Appendix B

Additional Plots Aerodynamic Stabilization

B.1 Average Altitude 200 km

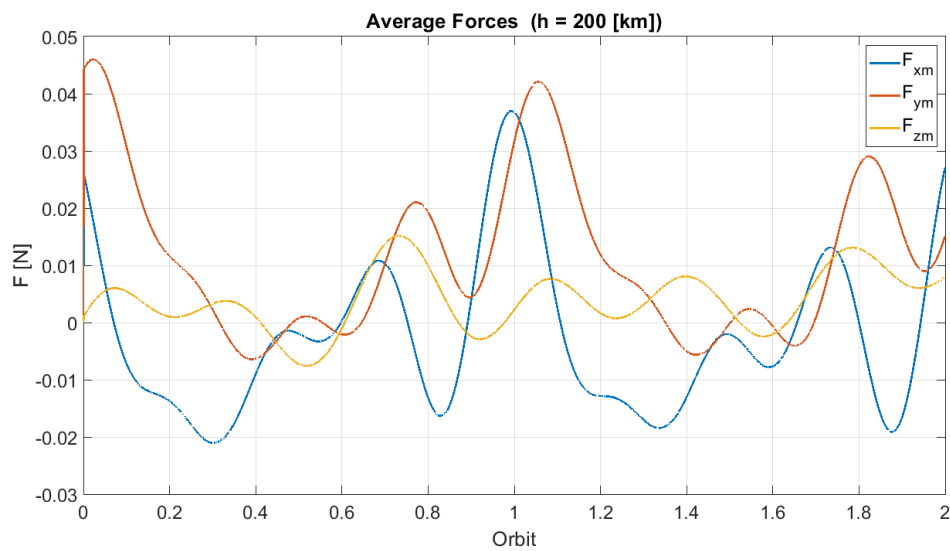


Figure B.1: Average control forces for an orbit with an average altitude orbit of 200 km

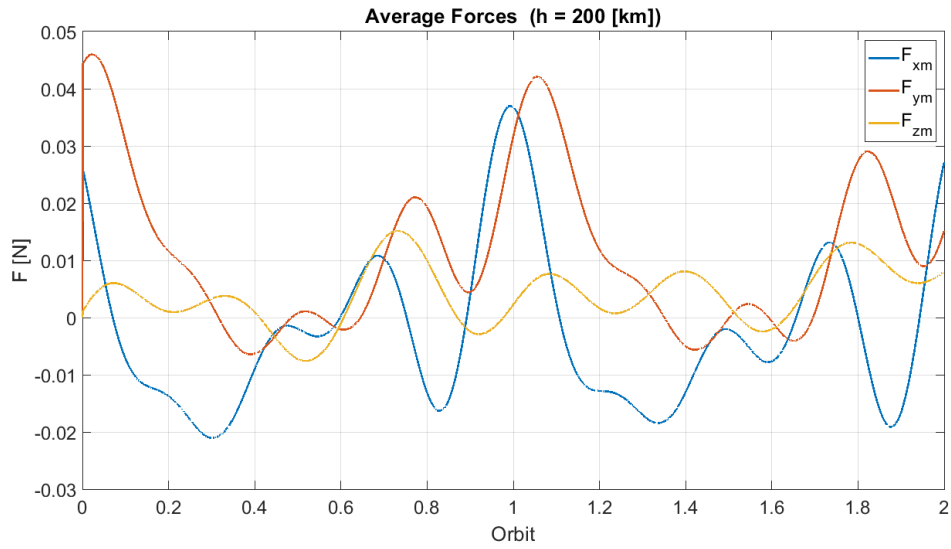


Figure B.2: *Differential control forces for an orbit with an average altitude orbit of 200 km*

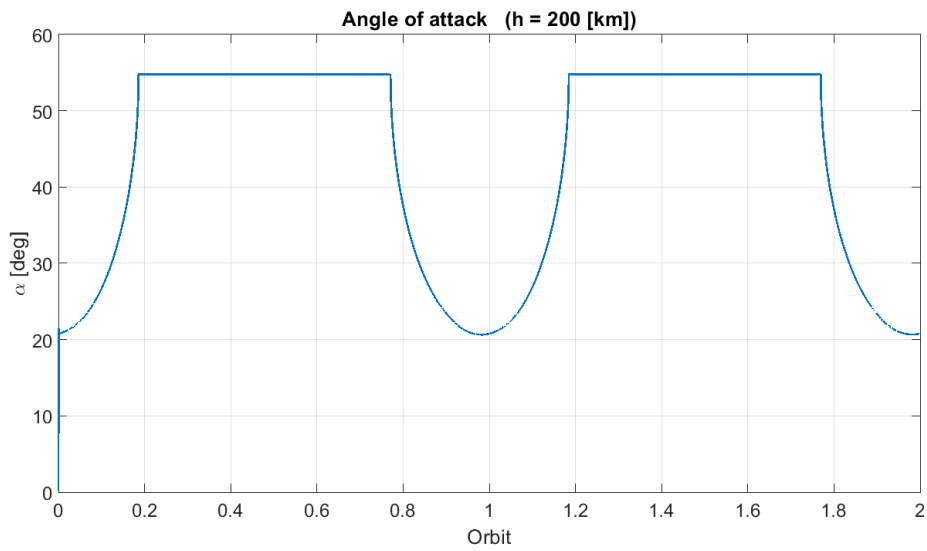


Figure B.3: *Variation of angle of attack for an orbit with an average altitude of 200 km*

B.2 Average Altitude 250 km

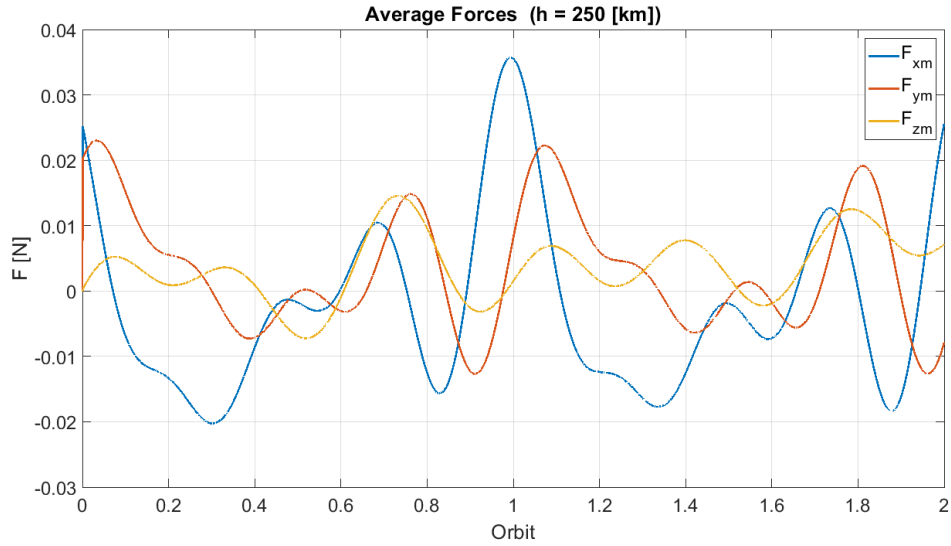


Figure B.4: Average control forces for an orbit with an average altitude orbit of 250 km

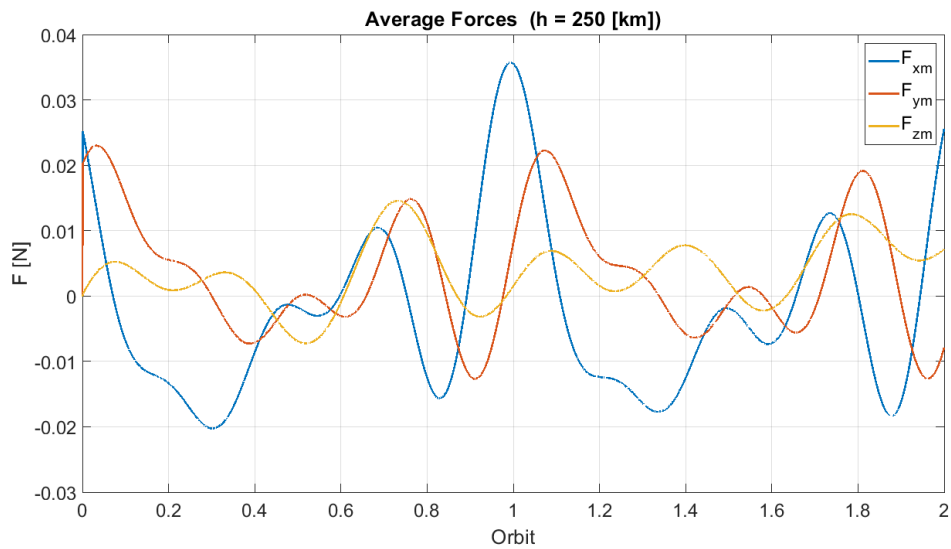


Figure B.5: Differential control forces for an orbit with an average altitude orbit of 250 km

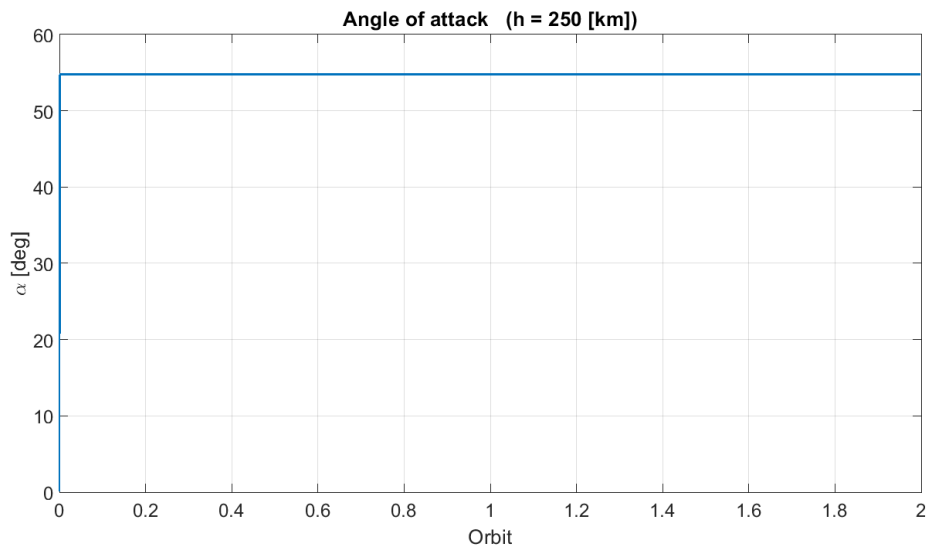


Figure B.6: Variation of angle of attack for an orbit with an average altitude of 250 km

B.3 Average Altitude 300 km

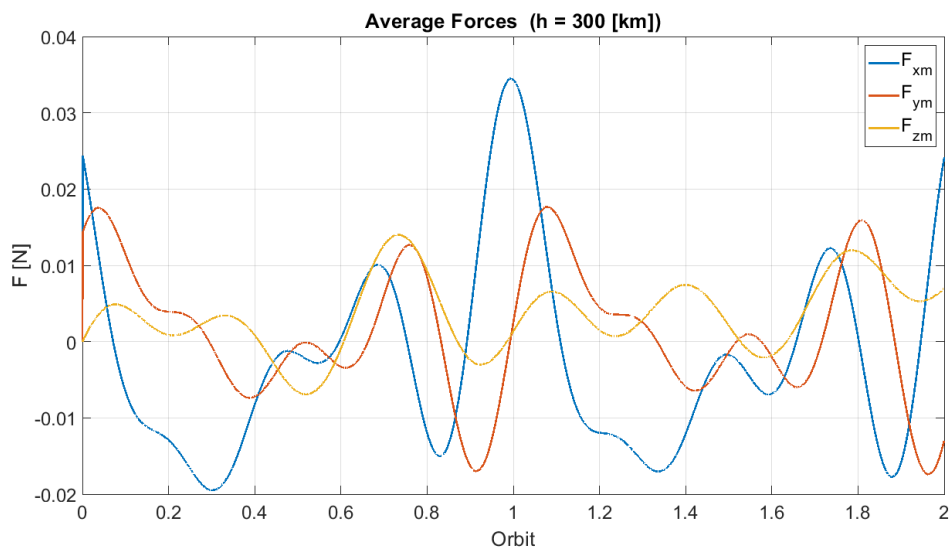


Figure B.7: Average control forces for an orbit with an average altitude orbit of 300 km

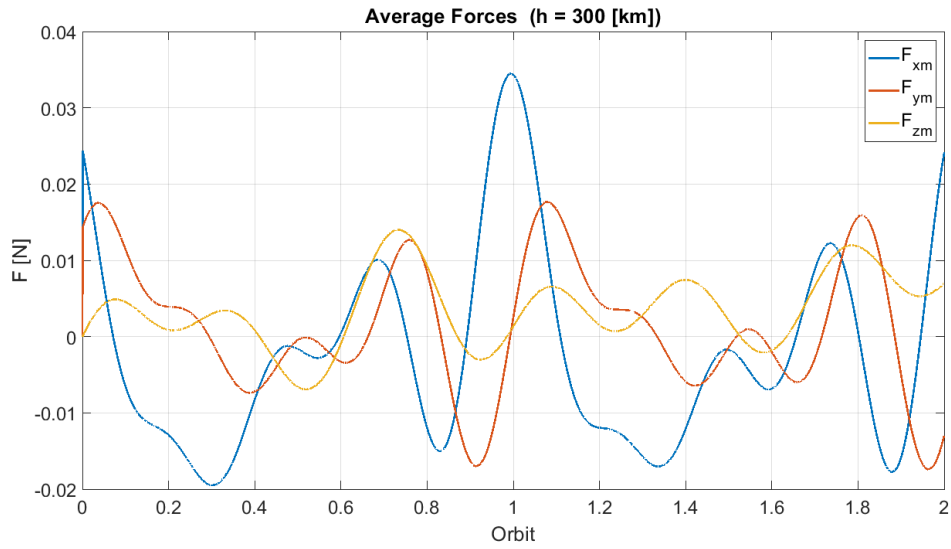


Figure B.8: *Differential control forces for an orbit with an average altitude orbit of 300 km*

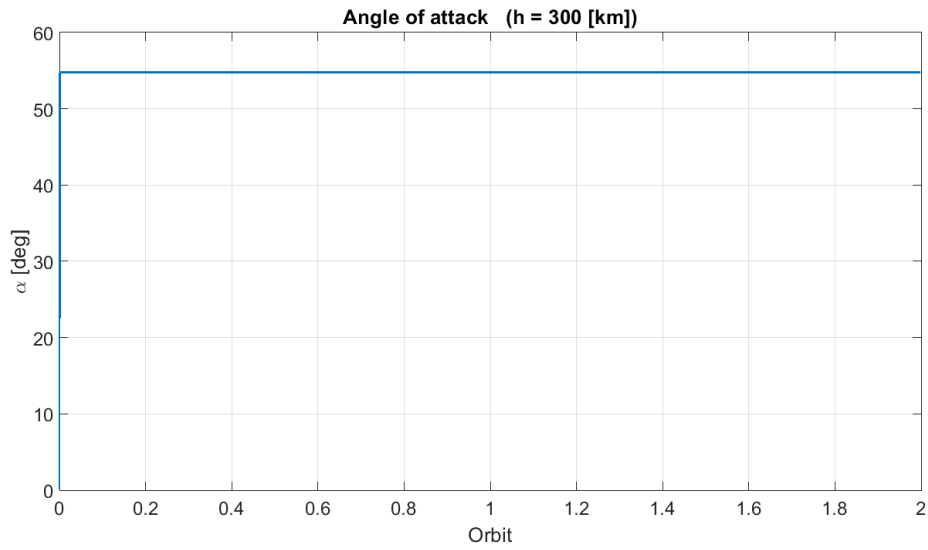


Figure B.9: *Variation of angle of attack for an orbit with an average altitude of 300 km*